

CARRIER-PHASE MULTIPATH MITIGATION IN RTK-BASED GNSS DUAL-ANTENNA SYSTEMS

LUIS SERRANO

October 2013



TECHNICAL REPORT
NO. 287

**CARRIER-PHASE MULTIPATH
MITIGATION IN RTK-BASED GNSS
DUAL-ANTENNA SYSTEMS**

Luis Serrano

Department of Geodesy and Geomatics Engineering
University of New Brunswick
P.O. Box 4400
Fredericton, N.B.
Canada
E3B 5A3

October 2013

© Luis Serrano, 2013

PREFACE

This technical report is a reproduction of a dissertation submitted in partial fulfillment of the requirements for the degree of Doctor of Philosophy in the Department of Geodesy and Geomatics Engineering, October 2013. The research was supervised by Prof. Richard B. Langley and Dr. Don Kim, and funding was provided by Natural Sciences and Engineering Research Council of Canada (NSERC), and the Canadian Space Agency (CSA).

As with any copyrighted material, permission to reprint or quote extensively from this report must be received from the author. The citation to this work should appear as follows:

Serrano, Luis (2013). *Carrier-Phase Multipath Mitigation In RTK-Based GNSS Dual-Antenna Systems*. Ph.D. dissertation, Department of Geodesy and Geomatics Engineering, Technical Report No. 287, University of New Brunswick, Fredericton, New Brunswick, Canada, 227 pp.

ABSTRACT

Carrier-phase multipath mitigation in GPS/GNSS real-time kinematic (RTK) mode has been studied for several years, at least since on-the-fly ambiguity resolution techniques were introduced, and receiver hardware improvements to the point that GNSS RTK-based systems provide position estimates at the mm to cm-level accuracy in real-time.

This level of accuracy has heralded a new era of applications where the use of GNSS RTK-based techniques have become a very practical navigation tool, especially in the fields of machine automation, industrial metrology, control, and robotics.

However, this incredible surge in accuracy tied with real-time capabilities comes with a cost: one must also ensure continuity, and integrity (safety). Typical users of these systems do not expect heavy machinery, guided and/or controlled by GNSS-based systems, to output erroneous solutions even in challenging multipath environments.

In multipath-rich scenarios, phase-multipath reflections can seriously degrade the RTK solutions, and in worst scenarios, integer fixed solutions are no longer available. This dissertation intends to deal with these scenarios, where the rover algorithms should deal with multiple reflections and, in real-time, be able to ameliorate/mitigate their effect.

GNSS-based heading/attitude is usually obtained combining the data from two or more antennas (also known as a moving baseline). Many companies provide commercial systems based on this technique, hence this dissertation finds its main applicability here.

Typical heavy construction machinery includes dozers, motor-graders, excavators, scrappers, etc., which are being equipped more frequently with GNSS dual-antenna systems to provide positioning and orientation information to the operator. We have not used and collected data from one of these machines, although the author has worked extensively with such machinery and their GNSS-based systems. However, the theory developed throughout this dissertation and the proof of concept through controlled tests that mimic the machinery/installed GNSS dual-antenna systems, are the basis of this dissertation.

Moreover the algorithms developed here are meant to be used independently from the receiver hardware, as well as from GNSS signals. Hence GLONASS, and/or Galileo signals can be processed too. This dissertation is based on the fundamental relationship between multiple multipath reflections from close-by strong reflections, and their effect on GNSS RTK-based dual-antenna systems.

Two questions were answered: Firstly, is it possible to retrieve strong multipath reflectors in kinematic applications? Second, once these strong reflectors are correctly identified, how accurate/reliable are the corrections to the raw carrier-phase multipath, knowing that the host platform performs unpredictable manoeuvres?

Based on the results, we can conclude that it is possible to estimate in real-time multipath parameters based on a strong effective reflector. In most of the tests it takes at least 2 minutes to obtain initial values (after *Kalman* filter convergence).

Once they are determined, multipath corrections can be determined straightforwardly for each satellite being tracked, as long as there are no cycle-slips (mostly due to the combination of the machinery high dynamics, especially within the areas where antennas are located, and the machinery itself blocking momentarily satellite signals).

DEDICATION

To Helena, and Margarida (*Guidinha*). You are my life and my inspiration.

ACKNOWLEDGEMENTS

First of all, I am deeply grateful to my advisor, Prof. Richard B. Langley, for giving me the opportunity to work in his group, and for his continuing support during these years. Work with you has been a real pleasure to me, and you have been a steady influence throughout my Ph.D. studies.

Furthermore, I am very grateful to my co-advisor, Dr. Don Kim, for insightful comments both in my work and in this dissertation, for his continuing support, and for many motivating discussions, some of them enjoying a good bottle of wine. I am also grateful to Prof. Marcelo Santos and Prof. Peter Dare for their dissertation review and support.

I would like to thank Prof. Virgilio Mendes, from the University of Lisbon, for introducing me to Satellite Navigation, and for “opening the doors” for my post-graduate studies. Besides being a good friend, I still use his lectures notes on my daily work.

I would like to thank the Canadian research agencies for funding this research, e.g., Natural Sciences and Engineering Research Council (NSERC), and the Canadian Space Agency (CSA).

I would like to thank my family, especially my parents who have always believed that a solid education, cemented with hard working, is the best path to achievement. Last, but not least, I would like to thank all of you my friends who have made my stay in Fredericton so much fun.

TABLE OF CONTENTS

| | |
|---|-----------|
| ABSTRACT..... | ii |
| DEDICATION..... | v |
| ACKNOWLEDGEMENTS..... | vi |
| LIST OF TABLES..... | xi |
| LIST OF FIGURES..... | xii |
| LIST OF SYMBOLS, NOMENCLATURES OR ABBREVIATIONS..... | xviii |
| 1 Introduction..... | 1 |
| 1.1. Limitations of Previous Work | 1 |
| 1.1.1 Multipath Mitigation Developments in Receiver (Time-Domain Processing)..... | 6 |
| 1.1.2 Multipath Mitigation Based on Multi-Sensor Fusion | 11 |
| 1.1.3 Weighting and SNR Models for Multipath Mitigation | 12 |
| 1.1.4 Electromagnetic Propagation Modeling for Multipath Analysis and Ray-Tracing | 14 |
| 1.1.5 Multipath Mitigation Using Spatial Processing Techniques..... | 16 |
| 1.2 Objectives..... | 18 |
| 1.3 Original Contribution | 19 |
| 1.4 Data Analyzed..... | 21 |
| 1.5 Thesis Outline | 23 |
| 2 GNSS Signal Fundamentals..... | 25 |
| 2.1 GNSS Signals | 25 |

| | |
|--|------------|
| 2.1.1 GPS Signal..... | 27 |
| 2.1.2 GLONASS Signal..... | 32 |
| 2.1.3 Galileo Signal..... | 34 |
| 2.2 GNSS Errors..... | 37 |
| 2.2.1 Orbit Errors | 38 |
| 2.2.2 Satellite and Receiver Clock Errors..... | 40 |
| 2.2.3 Ionospheric Error | 41 |
| 2.2.4 Tropospheric Error | 47 |
| 2.2.5 Multipath Error | 50 |
| 2.2.6 Random Errors | 55 |
| 2.3 Extended Kalman Filter | 56 |
| 2.4 Adaptive Estimation..... | 58 |
| 2.5 Whitening Filters | 65 |
| 2.6 RTK-based GNSS Heading/Attitude Systems..... | 67 |
| 3 Introduction to Carrier-Phase Multipath Error | 72 |
| 3.1 Electro-Magnetic Waves (Plane Waves) | 72 |
| 3.2 Polarization..... | 76 |
| 3.3 Multipath Spectra | 77 |
| 3.4 Reflection coefficient | 89 |
| 3.5 Carrier-phase multipath at the receiver carrier-tracking loop | 94 |
| 3.6 Carrier-phase multipath in a GNSS dual-antenna system..... | 109 |
| 4 MIMICS Strategy..... | 122 |
| 4.1 Concept behind the MIMICS algorithm | 122 |

| | |
|---|-----|
| 4.2 MIMICS Algorithm and Specular Carrier-Phase Multipath | 128 |
| 4.3 MIMICS Algorithm Steps | 133 |
| 4.4 - Central Difference Approximations | 140 |
| 4.5 Carrier-Phase Based Kinematic Velocity and Acceleration Estimation..... | 147 |
| 5 Adaptive Estimation Using Auto-Regressive Models | 162 |
| 5.1 Auto-Regressive (AR) Adaptive Estimation | 162 |
| 5.2 Kalman Filter Multipath Parameters Estimation..... | 175 |
| 5.3 Observability | 183 |
| 6 Tests and Results..... | 185 |
| 6.1 GNSS Software Simulation | 186 |
| 6.2 GNSS Hardware Simulation | 190 |
| 6.3 Real-Live Signal Tests | 196 |
| 6.4 Multipath Observables..... | 204 |
| 6.5 Extended Kalman Filter (EKF) Estimation..... | 210 |
| 7 Conclusions and Recommendations | 216 |
| 7.1 Introduction..... | 216 |
| 7.2 Conclusions..... | 218 |
| 7.3 Recommendations | 219 |
| Bibliography | 223 |
| Curriculum Vitae | |

LIST OF TABLES

| | |
|--|-----|
| Table 2.1: Uncertainties of ephemeris..... | 39 |
| Table 2.2: Typical GPS Range noise figures [Hofmann-Wellenhof et al., 2001]..... | 55 |
| Table 3.1: Various types of Costas phase-lock loop discriminators (d)..... | 102 |
| Table 6.1: Real-live signal tests statistics..... | 214 |

LIST OF FIGURES

| | |
|--|----|
| Figure 1.1: Effect of Multipath on C/A-Code cross-correlation function, that is, constructive and in-phase (redrawn from Borre <i>et al.</i> , [1994])..... | 2 |
| Figure 1.2: Effect of Multipath on C/A-Code cross-correlation function, that is, destructive, anti-phase (redrawn from Borre <i>et al.</i> , [1994])..... | 4 |
| Figure 1.3: GNSS Multi-Antenna Array (Navsys high gain portable GPS antenna array – HAGR – taken from Brown and Silva [1994])..... | 10 |
| Figure 1.4: Ray-tracing CAD model of direct and secondary propagation paths of different satellites (www.awecomunications.com)..... | 15 |
| Figure 2.1: Current Radio Navigation satellite system (RNSS) frequency bands..... | 26 |
| Figure 2.2: Generation of GPS signal at satellites (Borre <i>et al.</i> , [1994], page 18)..... | 29 |
| Figure 2.3: GPS L_1 signal structure (not scaled - Borre <i>et al.</i> , [1994], page 20)..... | 32 |
| Figure 2.4: Spreading code, subcarrier, carrier and signal as result of the BOC modulation (Borre <i>et al.</i> , [1994], page 38)..... | 35 |
| Figure 2.5: Ionospheric model broadcast by the WAAS system. It consists of a thin shell at 350 Km altitude which is discretized into a geodetically rectangular grid. A vertical delay estimate and a confidence bound on that estimate are made at each grid vertex..... | 43 |
| Figure 2.6: Ionospheric geometric path delay assuming a single-layer model. IP is the ionosphere point, z_0 and z' are the zenith angles at the ionosphere point and at the observing site, and R_E is the Earth's mean-radius (Hofmann-Wellenhof <i>et al.</i> , [2001])..... | 44 |
| Figure 2.7: Thickness of poly-tropic layers for the troposphere (Hofmann-Wellenhof <i>et al.</i> , [2001])..... | 48 |
| Figure 2.8: Geometry of multiple multipath specular reflections upon a static GNSS receiver..... | 51 |

| | |
|--|----|
| Figure 2.9: Carrier-phase multipath behavior varying the dampening-factor and keeping the phase-delay error at 45 degrees (top), and varying the phase-delay error and keeping the dampening-factor at 0.6..... | 54 |
| Figure 2.10: GNSS dual-antenna system located on a motor-grader’s blade (Trimble GCS900 on a motor-grader with dual GPS – Trimble website)..... | 68 |
| Figure 2.11: GNSS dual-antenna system located on the dozer’s blade blade (Trimble GCS900 on a motor-grader with dual GPS – Trimble website)..... | 69 |
| Figure 2.12: GNSS dual-antenna yaw and roll angles accuracies dependent on the baseline length (plots derived from a Matlab script using multiple antenna spacing between two GNSS-RTK receiver fixed solutions, and Equation 2.49)..... | 70 |
| Figure 3.1: Forward uniform plane-wave..... | 75 |
| Figure 3.2: Left and right circular polarizations..... | 77 |
| Figure 3.3: A typical multipath-rich environment..... | 78 |
| Figure 3.4: Specular reflection (left), and diffuse reflection (right) | 79 |
| Figure 3.5: Fresnel zone (where d is the distance between the transmitter and receiver, b is the radius of the Fresnel zone)..... | 80 |
| Figure 3.6: A 2-D ray-tracing model of forward scatter geometry..... | 81 |
| Figure 3.7 A 2-D ray-tracing model of backscatter geometry (I)..... | 82 |
| Figure 3.8: A 2-D ray-tracing model of backscatter geometry (II)..... | 85 |
| Figure 3.9: A 3-D ray-tracing phase multipath model in a dual-antenna system (master antenna A_0 , and slave antenna A_1)..... | 86 |
| Figure 3.10: Setup scenario for static carrier-phase multipath mitigation tests done by [Ray 2000]..... | 88 |
| Figure 3.11: Example of a GNSS-based heading (and pitch) reference system..... | 89 |
| Figure 3.12: Coupled reflection coefficient values for concrete, using several antenna attenuation values, and a 0 to 90 degrees incidence angle function..... | 93 |
| Figure 3.13: Schematic overview of how a GNSS receiver channel works..... | 95 |
| Figure 3.14: Schematics of a PLL (phase-lock loop) for carrier-tracking..... | 97 |

| | |
|---|-----|
| Figure 3.15: Costas-loop schematic, which is a 180° degrees phase-shift insensitive PLL..... | 99 |
| Figure 3.16: Discriminator input error (degrees)..... | 102 |
| Figure 3.17: Static carrier-phase multipath for GPS L_1 and L_2 (1 meter distance reflector)..... | 107 |
| Figure 3.18: Static carrier-phase multipath for GPS L_1 (5 meter distance reflector)..... | 108 |
| Figure 3.19: Geometric concept of a planar multipath wave incident upon a very short-spaced dual-antenna GNSS system..... | 113 |
| Figure 3.20: Short-spaced dual-antenna system with a strong specular reflector within 1m..... | 114 |
| Figure 3.21: Results from the test setup depicted in previous figure..... | 115 |
| Figure 3.22: Zoom to the first seven minutes of carrier-phase data (no motion)..... | 116 |
| Figure 3.23: Zoom to another segment of carrier-phase data when in static mode (again the x-axis is in minutes)..... | 117 |
| Figure 3.24: GPS L_1 and L_2 static carrier-phase multipath from a specular reflector (antenna separation is 0.5m and the reflector is at 1m distance)..... | 118 |
| Figure 3.25: Same scenario as before (0.5m antenna separation) however the reflector is at a distance of 5m..... | 119 |
| Figure 3.26: Carrier-phase multipath from a dual-antenna system performing a circular motion..... | 120 |
| Figure 3.27: Same as before but showing the satellite elevation angle variation..... | 121 |
| Figure 4.1: Inertial Aided GPS Based Attitude Heading Reference System (AHRS) for General Aviation Aircraft (note the four GPS path antennas on the aircraft body)..... | 122 |
| Figure 4.2: A dual-antenna GNSS-based orientation system used on an excavator..... | 125 |
| Figure 4.3: A dual-antenna GNSS-based orientation system used on maritime applications..... | 126 |

| | |
|--|-----|
| Figure 4.4: Another dual-antenna system used on maritime applications..... | 126 |
| Figure 4.5: UNB motion-table platform for GNSS-based Heading/Attitude system studies..... | 127 |
| Figure 4.6: Geometric view of a uniform plane wave field with two antennas close to each other (r_0 and r_1 are the three-dimensional phase-center coordinates of master and slave antenna, respectively)..... | 131 |
| Figure 4.7: Steps involved in the MIMICS strategy..... | 134 |
| Figure 4.8: Temex LPFRS-01/5M external oscillator used in our studies, connected to an oscilloscope..... | 135 |
| Figure 4.9: Graphic depicting the initial multipath bias to be obtained..... | 139 |
| Figure 4.10: Central difference approximations of different orders..... | 142 |
| Figure 4.11: Frequency response of the filter to the amplitude at a 1 Hz sampling rate. The fourth-order Butterworth filter with cut-off frequencies at 0.125 and 0.375 Hz is also plotted in the figure as an example of the conventional band-pass filters, which have more or less similar frequency responses..... | 150 |
| Figure 4.12: Line-of-sight relative geometry between satellite and user..... | 152 |
| Figure 4.13: Mechanics of satellite acceleration..... | 154 |
| Figure 4.14: Satellite velocity and acceleration accuracy assessment using broadcast ephemeris..... | 158 |
| Figure 5.1: MIMICS algorithm flow-chart (the initial steps of multi-antenna carrier-phase handling, and pre-processing are not depicted)..... | 163 |
| Figure 5.2: White noise model, power-spectral density functional (left), and auto-correlation function (right)..... | 165 |
| Figure 5.3: Flow-chart of a linear prediction function..... | 167 |
| Figure 5.4: The distribution of the AR order models for the estimated multipath observables..... | 172 |
| Figure 5.5: Periodogram of the original time series (used to generate a multipath observable)..... | 173 |

| | |
|--|-----|
| Figure 5.6: Periodogram of the whitened time series (used to generate the original multipath observable)..... | 174 |
| Figure 5.7: Dual-antenna system initial calibration, where the vehicle random vehicle motion causes a continuous variation in the between-antennas angle (θ), and thus leads to a multipath time-decorrelation..... | 175 |
| Figure 5.8: Multipath parameters estimation for each visible satellite (per epoch and simultaneously)..... | 176 |
| Figure 6.1: Illustration of one of the possible scenarios implemented in the simulator.. | 187 |
| Figure 6.2: Multipath parameters estimation using software simulations..... | 189 |
| Figure 6.3: Mechanical setup for dual-antennas random motion, and antenna optimal distance..... | 190 |
| Figure 6.4: Hardware simulator setup with all the required equipment..... | 191 |
| Figure 6.5: Vehicle speed and heading pre-programmed in the simulator scenario set-up..... | 192 |
| Figure 6.6: Top plot is the simulated multipath and in the bottom the estimated..... | 193 |
| Figure 6.7: Autocorrelation values for simulated data (in blue) and estimated data (in red)..... | 195 |
| Figure 6.8: Adaptation of a GNSS dual-antenna system to a typical vehicle..... | 197 |
| Figure 6.9: Site location where the kinematic real-live signal test was performed..... | 198 |
| Figure 6.10: Aerial view of the real-live signal test scenario..... | 199 |
| Figure 6.11: Results from the kinematic test (top plot RTK-based moving baseline estimation, and bottom plot RTK-based baseline distance between rover master antenna and base station)..... | 200 |
| Figure 6.12: Correlation between vehicle dynamics (heading angle) and the multipath spectra..... | 201 |
| Figure 6.13: Results from kinematic tests. Zoom to first 9 minutes..... | 202 |
| Figure 6.14: PRN 5 multipath observables delivered every 0.5 seconds..... | 204 |
| Figure 6.15: PRN 5 multipath observables delivered every second..... | 205 |

| | |
|---|-----|
| Figure 6.16: PRN 13 multipath observables delivered every 0.5 seconds..... | 206 |
| Figure 6.17: PRN 13 multipath observables delivered every second..... | 207 |
| Figure 6.18: Spectra of PRN 5 multipath observables..... | 208 |
| Figure 6.19: Spectra of PRN 13 multipath observables..... | 209 |
| Figure 6.20: Results from the MIMICS algorithm strategy in a real-time, kinematic real-time signal scenario (a zoom-in of the first 9 minutes)..... | 211 |
| Figure 6.21: Same signals as in last figure, however just depicting the two solutions, before (top) and after (bottom) the MIMICS multipath mitigation, for 25 minutes' worth of data (the spikes represent periods when RTK solutions were not available)..... | 212 |
| Figure 6.22: Multipath errors affecting the horizontal versus the vertical solution component..... | 213 |

LIST OF SYMBOLS, NOMENCLATURES OR ABBREVIATIONS

| | | |
|-------------|-----------|---|
| C_k | (various) | Variance-covariance matrix (in the least-squares sense) |
| A_k | (various) | Linearized system design matrix (in the least-squares sense) |
| H_k | (various) | Linearized system design matrix (in the <i>Kalman</i> filter sense) |
| I | (various) | Identity matrix |
| W | (various) | Weight matrix |
| Q_k | (various) | Process noise variance-covariance matrix |
| Φ_k | (various) | <i>Kalman</i> filter transition matrix |
| R | (various) | Measurement noise variance-covariance matrix |
| y_k | (various) | Measurement error vector |
| l | (various) | Measurement vector (observed) |
| V_k | (various) | Residual vector |
| w_k | (various) | Misclosure vector |
| $h_k()$ | (various) | Linearization of the observation equation (Extended <i>Kalman</i> filter) |
| X_k | (various) | State vector |
| λ_L | (various) | L-Band wavelength |
| r_{XX} | (various) | Auto-correlation function |
| Θ | (various) | Auto-regressive coefficient vector |
| τ | (s) | Time offset of GPS/GNSS code delay |
| τ | (s) | <i>Gauss-Markov</i> correlation period |

| | | |
|--------------------|------------|---|
| β | (s) | Inverse of the <i>Gauss-Markov</i> correlation period |
| β | (unitless) | Composite multipath <i>dampening</i> factor |
| α | (unitless) | Reflection Coefficient |
| c | (m/s) | <i>Vacuum</i> speed of light |
| A | (m) | Electromagnetic signal amplitude |
| $\Delta\varphi$ | (rad) | Multipath phase-offset / phase-delay |
| ψ | (rad/deg) | Yaw angle (Euler notation) |
| θ | (rad/deg) | Pitch angle (Euler notation) |
| θ_0 | (rad) | Multipath reflector elevation angle in order to master antenna |
| φ_0 | (rad) | Multipath reflector azimuth angle in order to master antenna |
| $\Delta\gamma_0$ | (rad) | Multipath reflector phase delay in order to master antenna |
| dion | (m) | Ionospheric delay or advance |
| dtrop | (m) | Tropospheric delay |
| dhyd | (m) | Hydrostatic part of the tropospheric delay |
| dwet | (m) | Non-hydrostatic part of the tropospheric delay |
| ε_p | (m) | Code pseudo-range random noise |
| ε_ϕ | (m) | Carrier-phase pseudo-range random noise |
| f | (Hz) | Frequency |
| N | (unitless) | Carrier-phase integer ambiguity |
| M | (m) | Carrier-phase multipath error |
| $M_{0,1}$ | (m) | Single-difference (between receivers) carrier-phase multipath error |

| | | |
|-----|-----------|---|
| P | (m) | Code pseudo-range measurement |
| S | (various) | Driving process noise spectral amplitudes |

| | |
|-------|---|
| AHRS | Attitude Heading Reference System |
| AR | Auto Regressive |
| ARMA | Auto Regressive Moving Average |
| BPS | Bits per Second |
| CAD | Computer-Aided Design |
| CDMA | Code Division Multiple Access |
| CS | Commercial Service |
| DoF | Degrees of Freedom |
| ESOC | European Space Operation Centre |
| EKF | Extended <i>Kalman</i> Filter |
| FIMLA | Fast Iterative Maximum-Likelihood Algorithm |
| FIR | Finite Impulse Response |
| FDMA | Frequency Division Multiple Access |
| FLL | Frequency-Locked Loop |
| GDOP | Geometrical Dilution of Precision |
| GTD | Geometrical Theory of Diffraction |
| GIM | Global Ionospheric Map |
| GNSS | Global Navigation Satellite System |
| GPS | Global Positioning System |

| | |
|---------|--|
| GRAPHIC | Group and Phase Ionosphere Calibration |
| GRL | Geodetic Research Laboratory |
| GLONASS | Global Navigation Satellite System (English Version) |
| ICD | Interface Control Document |
| IEEE | Institute of Electrical and Electronics Engineers |
| IGS | International GNSS Service |
| INS | Inertial Navigation System |
| IMU | Inertial Measurement System |
| ION | Institute of Navigation |
| LOS | Line of Sight |
| MSE | Mean-Squared-Error |
| MIMICS | Multipath Profile From Between Receiver Dynamics |
| NGA | National Geospatial-Intelligence Agency |
| NCO | Numerically Controlled Oscillator |
| NOAA | National Oceanic and Atmospheric Administration |
| OCXO | Oven Controlled Crystal Oscillator |
| PPP | Precise Point Positioning |
| PLANS | Position, Location and Navigation Symposium |
| PLL | Phase-Locked Loop |
| PRN | Pseudo Random Number |
| PRS | Public Regulated Service |
| RINEX | Receiver Independent Exchange Format |
| RTK | Real-Time Kinematic |

| | |
|------|---|
| RMS | Root-Mean Square |
| SAR | Search and Rescue |
| SBAS | Satellite-Based Augmentation system |
| SoL | Safety-of-Life |
| TCXO | Temperature Controlled Crystal Oscillator |
| TEC | Total Electron Content |
| UKF | Unscented Kalman Filter |
| UNB | University of New Brunswick |
| UTD | Uniform Theory of Diffraction |
| WAAS | Wide-Area Augmentation System |

1 Introduction

This dissertation presents a novel approach to deal with carrier-phase multipath reflections in kinematic applications, particularly in GNSS RTK-based dual-antenna systems. These systems are typically employed in scenarios where strong multipath and blockages, and high platform dynamics (or variable dynamics) are very common.

This first chapter outlines research performed within the scientific and industrial community to ameliorate the effect of phase multipath (C/A-code multipath is acknowledged as well due to its obvious intrinsic relationship with phase multipath).

Even though this dissertation is based on specific dual-antenna phase multipath mitigation for kinematic scenarios, a thorough description of different methods covering a broad spectrum of applications will be made, and their limitations will be identified. Based on that, the original contribution of this dissertation will be explained with support coming out from the several simulated and real-live signal data sets used throughout these studies. Finally, the dissertation overview is given.

1.1. Limitations of Previous Work

Multipath propagation of the GPS signal is a dominant source of error in differential positioning. Objects in the vicinity of a receiver antenna (notably the ground) can easily

reflect GPS signals, resulting in one or more secondary propagation paths. These secondary-path signals, which are superimposed on the desired direct-path signal, always have a longer propagation time and can significantly distort the amplitude and phase of the direct-path signal. A simple graphical explanation on how multipath contaminates the original signal, just thinking of the C/A-code, is given in the next 2 figures.

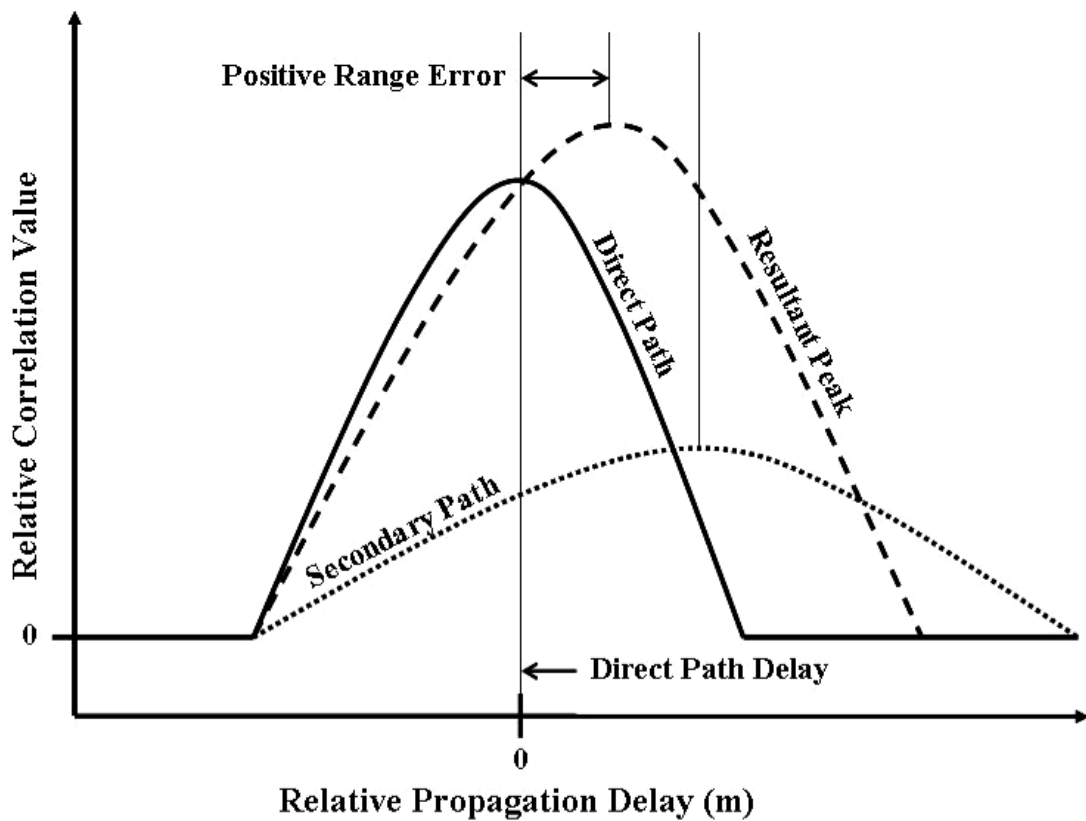


Figure 1.1: Effect of Multipath on C/A-Code cross-correlation function, that is, constructive and in-phase (redrawn from Borre *et al.* [1994])

In an idealistically multipath-free environment, there would be no secondary paths, only direct paths, thus the multipath range error would be zero based on the correct and undistorted cross-correlation peak (ideally without thermal noise as well).

In real-life scenarios, however, with multiple reflections from near and far away reflectors, the resulting cross-correlation peak will now have, at best, two superimposed components, one from the direct path and one from the secondary path.

The resultant peak is a function with a distortion depending on the relative amplitude, delay, and phase of the secondary path. There are two possibilities:

- For a constructive secondary path we end up with a positive range error depicted in Figure 1.1
- For a destructive secondary path, Figure 1.2, we end up with a negative range error.

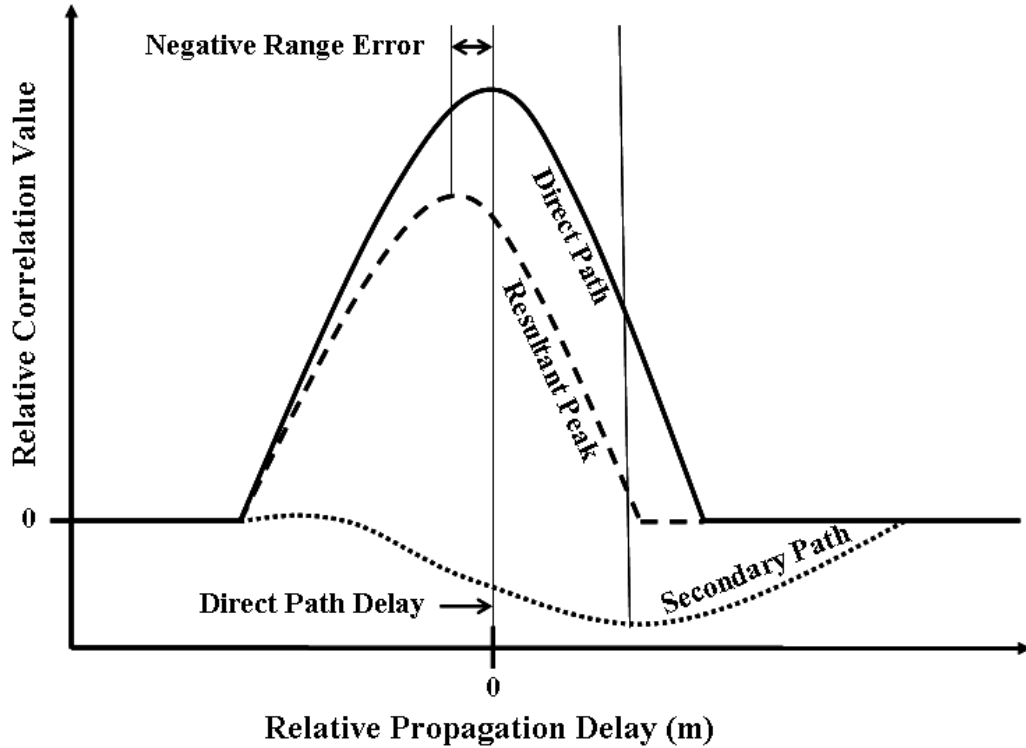


Figure 1.2: Effect of Multipath on C/A-Code cross-correlation function, that is, destructive and anti-phase (redrawn from Borre *et al.* [1994])

More important for precise differential positioning, phase-multipath remains the single-most important source of error in short baseline kinematic GNSS and in most network real-time kinematic applications. Driving down multipath errors is probably the most important objective of current research into the use of GNSS for machine automation/construction and engineering applications, as it is for heading/attitude determination from GNSS.

Most of the original research done in this area, especially during the beginning of true GPS real-time kinematic techniques throughout the 1990s, did not really differentiate between static and kinematic multipath mitigation techniques.

In fact, much of the research done in these days using the GNSS phase observable still does not reflect that fact even though it would be logical to do so due to a better understanding of phase-multipath dynamic behavior. Nevertheless, and from a practical point of view, the majority of phase-multipath mitigation techniques within receivers, in theory, should be the same regardless of the user platform dynamics (here one does not include dedicated geodetic-quality receivers used for permanent reference stations).

With some adaptations, the receiver firmware should be flexible enough so that the multipath mitigation algorithms automatically detect a variation in the receiver dynamics and the consequential phase-multipath change. Hence, this reflects much of the research done nowadays, in particular in adaptive stochastic modeling theory, and in general dynamic filtering fine-tuning. Moreover, MEMS IMU sensors could also be used to detect dynamics variation, for short periods, due to their high sensing-rate and short latency [Geng *et al.*, 2007].

Therefore, I will provide a historical list of major mitigation techniques that conceptually reflect all the “stakeholders” involved in any phase-multipath signal processing/mitigation technique, and their intrinsic limitations. They include receiver and antenna hardware, software (algorithms), techniques for specific application (including

GNSS multi-antenna systems, attitude, multi-sensor fusion, etc.), and multipath propagation modeling. All these techniques can be ordered in the following way:

1.1.1 Multipath Mitigation Developments in Receiver (Time-Domain Processing)

Receiver manufacturers have developed most of the practical approaches. However they are often reluctant, for commercial, competitive, and intellectual property reasons, to explicitly reveal their methods. Despite that, many of the historical receiver multipath mitigation techniques were published in some seminal articles described below.

Narrow-Correlator Technology

The first significant means to reduce GPS multipath effects by receiver processing made its debut in the early 1990s. Until that time, most receivers had been designed to use 1.0 chip early-late correlator spacing in the implementation of delay-lock loops (DLLs).

The paper by Van Dierendonck *et al.* [1994] demonstrates that noise reduction is achieved with narrower correlator spacing (thus the widely used term narrow-correlator technique) because the noise components of the early and late signals are correlated and tend to cancel, provided that early and late processing is simultaneous (not dithered). Also included in the narrow correlator concept is the fact that a receiver higher front-end

bandwidth is employed so that there can be higher sampling which enables the narrow spacing.

Multipath effects are reduced because the DLL discriminator is less distorted by the delayed multipath signal (as depicted in Figures 1.1 and 1.2).

Correlation Function Shape-Based Methods

Still in the 1990s, and after the successful implementation of the narrow-correlator technique, researchers continued working on ways of understanding and reducing distorted-shape correlation functions due to secondary path signals. A study, and subsequent article [Townsend *et al.*, 1995], revealed a new technique to determine the parameters of the multipath model from the shape of the correlation function. This technique, the multipath estimating delay lock loop or MEDDL, estimates both line-of-sight and multipath signal parameters, thereby reducing the influence of the multipath signals on the code and carrier estimates of the direct-path signal.

The limitation in this technique arises from the practical difficulty in attempting to map each measured shape into a corresponding direct-path delay estimate. Even in simple cases (just two signals, direct and one secondary path signal), a large number of correlation function shapes must be handled. Nevertheless, this article is quite important in the sense that it specifically addresses carrier-phase multipath mitigation.

Maximum-Likelihood Multipath Estimation

One of the most notorious approaches to time-domain multipath mitigation within receiver technology is called multipath mitigation technology (MMT), and is incorporated in a number of GPS receivers manufactured by the Canadian company NovAtel with the name Vision Correlator [Fenton and Jones, 2005].

The MMT algorithm was actually developed by Larry Weill and Ben Fisher [Weill and Fisher, 1996], and is an optimized maximal likelihood process that attempts to estimate the “best fit” of the vision correlator vector (an array containing pulse-shape information given by $[\tau, A, \theta]$, where τ represents time offset of code delay, A represents the amplitude, and θ represents the carrier-phase angle) with multiple versions of the reference function, i.e., the vision correlator vector representing the line-of-sight signal.

The limitation in the MMT technique, as in many original receiver-dedicated multipath techniques, is that it reaches the theoretical performance limits, albeit being able to improve short-delay carrier-phase multipath. Still, in articles depicting this technique, it is acknowledged that MMT cannot deal with multipath delays of up to one meter so common in GNSS-positioned machines with multiple parts.

Maximal likelihood theory is relatively straightforward, however its implementation at (GNSS) receiver level is quite cumbersome and it derives considerable receiver memory and power, although with today’s GNSS receiver hardware, these are not major limiting

factors (at least for high-end receivers). However, Sahmoudi and Landry [2008] have derived a new approach dubbed fast iterative maximum-likelihood algorithm (FIMLA) that optimizes the maximum likelihood receiver implementation using the GNSS signal model structure and the spreading code periodicity.

So far (as of 2013) this is the ongoing trend in time-domain multipath mitigation techniques, that is, many receiver implementation developments using all the power brought by cheaper and better software, and hardware receivers.

Multi-Antenna Arrays

As explained above, GNSS commercial companies make heavy investments in novel digital signal processing (DSP) techniques and hardware to improve their receiver-immunity to multipath signals, thus unsurprisingly they do not reveal or publish anything about the algorithms, at least in the early stages of commercialization. Therefore, academic research tended to develop smart and flexible solutions not dependent on the chosen hardware.

Use of multiple GNSS antennas is quite common in several dynamic applications where GNSS-based attitude systems are one example (civil applications), and GNSS phased-array antennas for anti-jamming mostly used in electronic warfare.

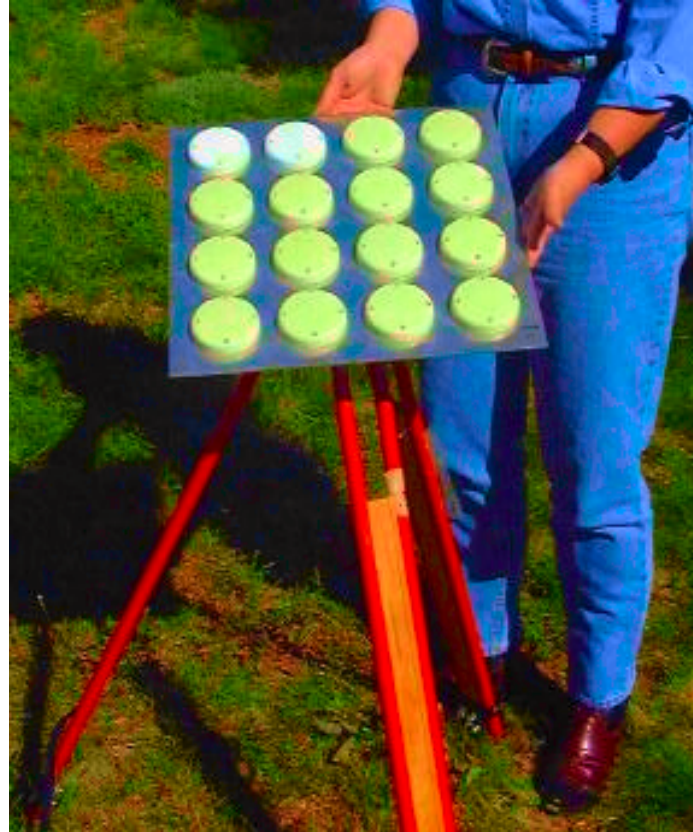


Figure 1.3: GPS Multi-Antenna Array (Navsys high gain portable GPS antenna array – HAGR – taken from Brown and Silva [1994])

Using an array of very closely-spaced antennas (Figure 1.3) and assuming that multipath signals are heavily correlated among the different antennas is also used as a means to mitigate phase-multipath. An original work has been developed around this idea [Ray *et al.*, 1998], where the correlated nature of multipath, along with the known geometry among the antennas, are used with the relative carrier phase differences to aid in the extraction of the direct carrier phase from the multipath-corrupted carrier-phase measurement.

One of the limitations in this approach is that it is only intended for static carrier-phase multipath mitigation. Moreover, and in order to guarantee observability in the estimation of the multipath parameters, it is necessary to have an array of at least five “patch” antennas placed very close to each other. This can be quite impractical in some applications and platforms, not to mention an increase in hardware cost and complexity.

Probably the biggest limitation in this approach might be the fact that phase multipath is highly dependent on the antenna site position, thus even if the antennas are rather closely spaced together, one should still expect some multipath decorrelation in between the array of antennas. However, this original work, despite its inherent limitation in being employed in dynamic applications, provided to a great extent some of the background of this dissertation as it will be seen later on.

1.1.2 Multipath Mitigation Based on Multi-Sensor Fusion

The rationale behind the integration of measurements from different sensors and GPS is that some sensors, like inertial ones, are immune to external signal corruption sources. This is very important, especially in GPS-based navigation techniques in critical applications, where signals are potentially corrupted by intentional/unintentional jamming, multipath and attenuation, and loss-of-lock due to high dynamic maneuvers. Inertial sensor measurements are virtually immune to these perturbations.

However, there are some strong limitations in this approach. Firstly, most of the research carried out in this area deals with systems using C/A-code observables, mostly for urban/indoor navigation where meter-level accuracy is sufficient. Hence, it is unknown to a large extent the real benefits in using GPS and inertial navigation system (INS) integration for phase-multipath mitigation. Moreover, despite inertial measurements having larger bandwidths and resolution when compared to GPS signals, they are not accurate and stable enough (at least for affordable inertial sensors) to be able to detect and extract GPS phase-multipath signals.

1.1.3 Weighting and SNR Models for Multipath Mitigation

Other software-based carrier-phase multipath mitigation techniques rely on the signal-to-noise ratio (SNR) observable. Usually this observable is mostly used to weight code pseudoranges, however due to the dependability of the SNR observable on the quality of the receiver-generated measurements it is quite reasonable to use it as a means to ameliorate noise and phase-multipath adaptively.

This can be accomplished by using straight-forward SNR measurements to develop covariance matrices weighting models. The article by Comp and Axelrad [1996] explains how this observable is used to adaptively estimate the spectral parameters (frequency, amplitude, phase offset) of multipath in the associated SNR, and then in constructing a profile of the multipath error in the carrier-phase. The foundation of this technique centers on the following equation (Equation 1.1), where $\Delta\varphi$ is the phase-delay caused by

multipath, $\alpha_i A_0$ is the multipath amplitude fluctuation, and ψ_i is the multipath phase-offset due to the i th of n reflections.

$$\Delta\varphi \approx \frac{\sum_i^n \alpha_i A_0 \sin(\psi_i)}{A_0 A_a + \sum_i^n \alpha_i A_0 \cos(\psi_i)} \quad (1.1)$$

This equation, as will become clear in further chapters, is fundamental throughout this dissertation as it provides part of the theoretical background for the dual-antenna system phase-multipath observable developed. Here, it relates with the SNR observable in the form of the following equation, as the phase-multipath fluctuations in the SNR are modeled as sinusoids:

$$SNR_{mp} = \sum_i^n \alpha_i(t) A_0 \cos(\psi_i(t)) + v \quad (1.2)$$

where v represents the remaining un-modeled errors not related to multipath. The limitation in this approach is also, in a way, one of its biggest advantages; i.e., the SNR observable is less sensitive to platform motion than the differential phase measurements, making it suitable for high-dynamic vehicles. However, being less sensitive to signal-embedded dynamics makes SNR also less sensitive to sudden changes in the multipath signal dynamics, thus making this approach impractical in many GPS-based machine automation scenarios.

Another limitation is a fact well depicted in a private memo by Collins *et al.* [1999]. In this memo, we can see that the receiver-generated SNR values may have different formulations to provide meaningful output quantities, depending on the receiver manufacturer.

1.1.4 Electromagnetic Propagation Modeling for Multipath Analysis and Ray-Tracing

The computational electromagnetic modeling technique is a powerful tool to solve electromagnetic problems as they estimate the solution to a problem based on a full-wave analysis. Modeling can be used to study the propagation of GNSS signals as well, as seen in Figure 1.4, where computer-aided design (CAD) tools are used to propagate the electromagnetic systems based on the relationship between the electromagnetic signals orientation, and the modeled buildings, blockages, and reflectors geometry.

The geometrical theory of diffraction (GTD)/uniform theory of diffraction (UTD) are one of the electro-magnetic (EM) modeling techniques. The GTD technique provides a high frequency approximation solution of Maxwell's equations to the electromagnetic fields including direct, reflected and diffracted signals [McNamara *et al.*, 1990].

This method is suitable for the case when the dimensions of objects being analyzed are large relative to the wavelength of the field. Detailed geometry information is required before giving out the solution. The difference between (GTD) and (UTD) is that the later

method implements the improvements to the diffraction coefficients of the former method.

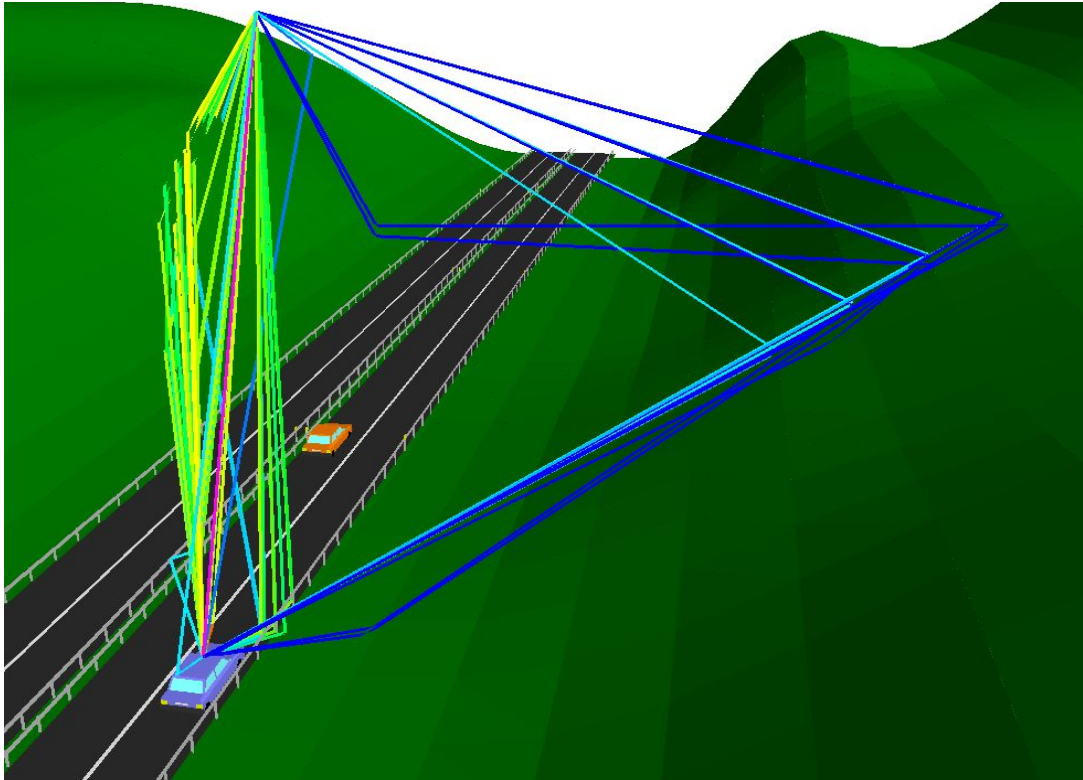


Figure 1.4: Ray-tracing CAD model of direct and secondary propagation paths of different satellites (www.awe-communications.com)

Because of the size of buildings and other man-made structures compared to the corresponding wavelength of wireless frequencies, direct numerical solvers of Maxwell's equations, such as the finite element and finite difference methods, involve too many unknowns to feasibly estimate in real time.

Dealing with multiple reflectors, using the technique of ray-tracing, is in principle simply a matter of modeling the received waveform as the sum of the responses from the different paths rather than just two paths. However, finding the magnitude and phase of these responses is no simple task, thus this technique to develop multipath maps based on EM propagation and ray-tracing techniques is quite useful in research and planning of wireless systems, but impractical for real-time precise GNSS applications.

1.1.5 Multipath Mitigation Using Spatial Processing Techniques

This introductory chapter, albeit describing hardware and software-based multipath mitigation techniques using DSP techniques and algorithms, would not be complete without mentioning simple spatial techniques. Therefore, for the sake of completeness, a brief overview of these techniques will be given.

Antenna Location Strategy

This is perhaps the simplest form of spatial processing to position the antenna where it is less susceptible to receiving multipath reflections. However, this is a technique with a very limited applicability in dynamic applications due to the constant change in environment.

Ground-plane and Choke-Ring Antennas

The most common form of spatial processing is an antenna designed to attenuate signals reflected from the ground or arriving at low elevation angles, like most commercial GPS antennas do nowadays. Nevertheless, this simple antenna design cannot prevent that wave fronts arrive at the ground plane disk edge from below inducing surface waves on the top of the disk that then travel to the antenna element and inflict serious multipath contamination.

The most well-known way of eliminating this effect is using the so-called choke-ring antennas. However, their size, weight and cost makes it rather prohibitive to be used in virtually all dynamic applications, especially in machine automation where hardware is subject to very harsh conditions.

NovAtel once again innovated in this area by developing (and patenting) an antenna with a multipath mitigation performance similar to one achieved with a choke-ring antenna, however with much reduced size and weight, dubbed pinwheel antenna [Kunysz, 2000].

Directive Arrays

Antenna arrays form a highly directive spatial response pattern with an obvious high gain in the direction of the direct path signal and attenuation in the other remaining directions from which secondary-path signals may arrive. Directive arrays are not affordable and are often impractical because it is almost impossible to detect all the possible scenarios of

gain and attenuation for all different satellite signals especially when the host platform is moving.

1.2 Objectives

The overall goal of my research was to develop a complete and novel phase-multipath mitigation technique, which can be used efficiently in real-time kinematic applications, independent of the manufacturer hardware (although as mentioned before, based on common dual-antenna systems).

The rationale behind this work is that the technique should be simple and flexible enough to be used in any automation and guidance application regardless of the platform. And at the same time, it should provide realistic phase-multipath corrections to the raw observations without losing throughput capabilities.

This means that the multipath mitigation algorithms should be able to provide accurate corrections with reasonable short-time latency. In order to achieve these objectives, this research was phased in the following steps:

1. The development and assessment of observables that physically represent or mimic the behavior of signal multipath in real-live scenarios such as GPS-based machine guidance in urban or construction environments;

2. The correlation of those observables with the vehicle dynamics, and the identification of the source and kind of reflectors originating the signal phase-multipath error characteristics;

3. Develop a strategy, in this case the so-called MIMICS (**M**ultipath Profile from **B**etween Receiver **D**ynamics) technique, using the information gathered in the two previous steps to process the signals in real time (or in near real time), in order to improve the positioning navigations results;

4. Create validation methods to clearly assess if this strategy is as successful as planned. As with any other science field, a lot of resources should be allocated to this part in order to improve the strategy or correct misconceptions. This included analysis of data from different broad scenarios, both simulated and real-live signals, and obviously the use of comparison methods with ground truth references.

1.3 Original Contribution

This dissertation clearly innovates in a quite recent field of GNSS-based applications, where due to its real-time nature a high-level of accuracy and reliability is necessary. This may include dual-antenna machine guidance systems found in the construction and mining industries for the guidance of dozers, motor graders, excavators, scrapers as well

as in agricultural applications for the guidance of tractors and harvesters. A shipyard crane-guidance system is another field of application.

A few phase-multipath mitigation techniques, from which this dissertation evolves, were previously described. Such techniques include the mitigation of static carrier-phase multipath using an array of closely spaced antennas [Ray *et al.*, 1998], and the use of adaptive SNR-based carrier-phase multipath mitigation techniques [Comp and Axelrad, 1996].

The major contribution of this dissertation is that it takes the inputs of these two techniques and merges them in a synergistic way and overcomes their individual limitations. This means that in this novel technique, which to the best of my knowledge is thus far unique, phase-multipath mitigation can be carried out in real-time applications, independently of the platform, the hardware, and platform dynamics, and using only two GPS antennas.

Moreover, the background algorithm to mitigate static/kinematic phase multipath does not rely on derived observables that may mask true phase-multipath signals, but rather it relies only on the raw multipath-contaminated carrier-phase observable. To the best of my knowledge, including techniques from industrial and academic institutions, this is the only technique performing this kind phase-multipath processing.

Secondly, and during the development of this novel technique, the author realized that most of the understanding (and thus the processing) of phase-multipath signals in multiple dynamic scenarios relies on a rather original stochastic concept developed by Kim and Langley [2002] called quasi-random errors:

“[T]hey have temporal and spatial characteristics which are more or less quasi-random. To detect and remove quasi-random errors, they must be handled using a rigorous mathematical approach to isolate their effects from parameter estimates.”

In this dissertation, original adaptive stochastic software algorithms were developed for real-time purposes, which reflect and can typically handle the phase-multipath “quasi-random” behavior due to multiple reflections and random platform dynamics.

1.4 Data Analyzed

Knowing that the description of the spectrum of GNSS multipath in phased-array antennas and the inherent modeling is quite a hefty task (although very important to many applications benefiting from the attempt to remove/ameliorate multipath errors, as well as other research areas such as anti-jamming and interference detection systems), we developed several techniques, methodologies, and dedicated hardware components to simulate, collect, and analyze the required data that can be useful in all these research areas.

These techniques and methodologies originated the following software, hardware, methodologies, and results:

1. Phased-array antenna multipath simulation (where, in this study, only two antennas are used and in same plane, but that can be changed according to the simulation scenario), which includes choice of antenna random motion and relative geometry, plus the distance, elevation angle and azimuth for up to 4 major multipath (specular) reflectors.
2. Development of a 3-axial, six degrees of freedom, motion table to collect multipath data in a GNSS-based attitude system (using 4 antennas). Although this table, quite complex and powerful, was developed in the scope of a different project, it had an immense impact on the understanding of how such systems behave in the presence of strong multipath reflectors.
3. Adaptation of the motion table to a simple dual-antenna motion table system where it is possible to simulate multiple random motions between only two closely-space antennas. Moreover this platform was integrated (with variable distance length) with a large specular “thin-foiled” reflector allowing the study of specular reflectors in the vicinity of the GNSS antennas.
4. Development of simulation methodologies, mostly related to multiple platform realistic dynamics simulation in face of severe multipath reflections, such as

experienced by vehicles in urban canyons, to be used with a GNSS hardware simulator.

5. Use of all the information gathered throughout software/hardware simulations, and real-live signal data with meaconing (forced multipath reflector). Therefore, based on the previous developments mimic those scenarios collecting data on a vehicle with a GNSS-based dual-antenna system navigating close to effective strong reflectors.

1.5 Thesis Outline

Chapter 2 discusses the fundamentals of global navigation satellite systems (GNSS) where an introduction to some concepts related to Galileo signal structure and services is made due to its already and foreseen availability. This is rather important because, as explained before, this dissertation relies on a technique that should be independent from the hardware in use and, in theory, from the carrier-phase signals employed.

Albeit developed for GPS signals, there is nothing that hinders the extension and use of this dissertation work for Galileo carrier-phase signals (or GLONASS or some other GNSS for that matter). An overview of optimal estimation methods and filtering techniques will be covered as well as an introduction to some of the algorithms developed throughout this dissertation.

Chapter 3 covers in more detail the description of multipath signals and spectra, and the physical relationship of carrier-phase multipath in multiple GPS antennas. And finally an introduction is made to between-antennas multipath observables derivation.

Chapter 4 describes the MIMICS technique as a basis of this dissertation. A detailed description of its mathematical formulation and derivation is provided. The use of carrier-phase higher-order range dynamics will be overviewed from the dynamic application point-of-view.

Chapter 5 covers in detail the mathematics behind phase-multipath adaptive estimation, adaptive stochastic modeling and its implementation on real-time software algorithms. The intrinsic relationship between multipath mitigation calculations and its latency will be analyzed.

Chapter 6 describes, by order, all the tests performed throughout this work, from software simulations to hardware simulations, to real-live signal tests. The application of the MIMICS algorithms to mitigate multipath signals with a series of real-live signal scenarios and results are then presented and discussed.

Chapter 7 draws conclusions from this work, and presents recommendations for future work.

2 GNSS Signal Fundamentals

2.1 GNSS Signals

The GNSS satellites continuously transmit navigation signals in two or more frequencies in L band. These signals contain ranging codes and navigation data to allow the users to compute the travelling time from satellite to receiver, and the satellite coordinates at any epoch. The main signal components are described as follows:

1. **Carrier:** Radio frequency sinusoidal signal at a given frequency;
2. **Ranging code:** Sequences of 0s and 1s (zeroes and ones), which allow the receiver to determine the travel time of radio signal from satellite to receiver. They are called Pseudo-Random Noise (PRN) sequences or PRN codes;
3. **Navigation data:** A binary-coded message providing information on the satellite ephemeris (Keplerian elements for GPS, or satellite position and velocity for GLONASS), clock bias parameters, almanac (with a reduced accuracy ephemeris data set), satellite health status, and other complementary information.

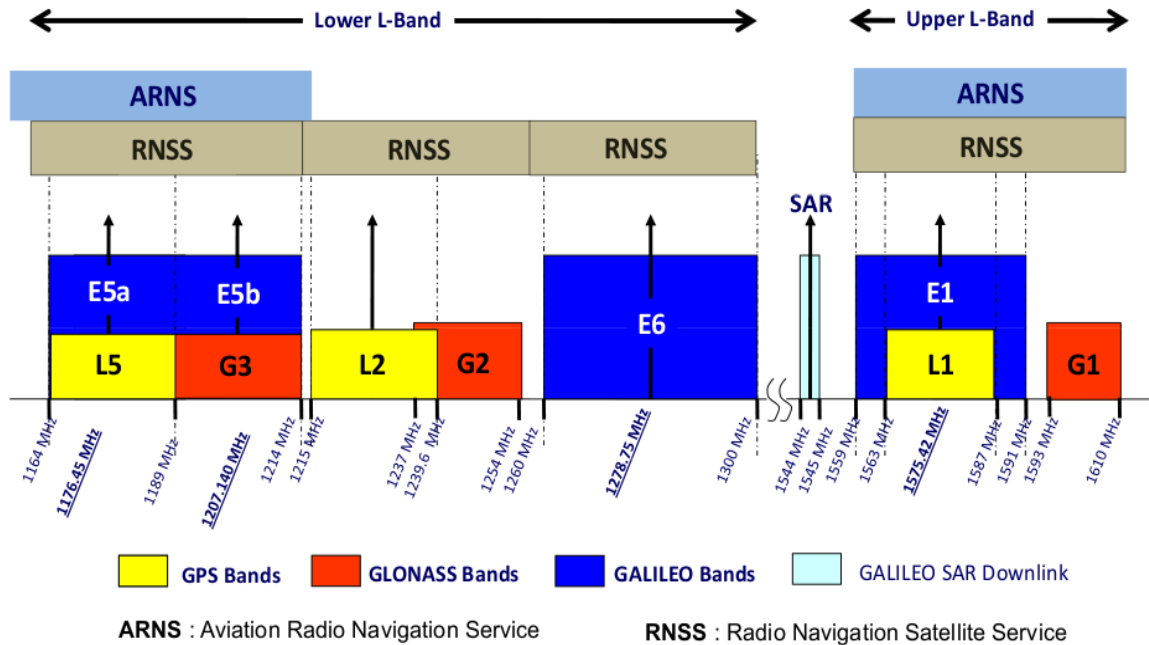


Figure 2.1: Current Radio Navigation Satellite System (RNSS) frequency bands (figure taken from ESA Navipedia website, [Subirana *et al.*, [2011]])

We can see depicted in Figure 2.1 the frequency bands currently used by RNSS. There are two bands in the region allocated to the Aeronautical Radio Navigation Service (ARNS) on a primary basis worldwide. These bands are especially suitable for Safety-of-Life (SoL) applications because no other users are allowed to interfere with their signals.

They correspond to the upper L band (1590.0 to 1610.0 MHz), having the GPS L_1 , Galileo E_1 and GLONASS G_1 , and to the bottom of the Lower Band-L (1151.0 to 1214.0 MHz), where GPS L_5 and Galileo E_5 are located, with E_{5a} and L_5 coexisting in the same frequencies. The remaining GPS L_2 , GLONASS G_2 and Galileo E_6 signals are

in the bands 1215.6 to 1350.0 MHz. These bands were allocated to Radio-location Services (ground radars) and RNSS on a primary basis. Thence the signals in these bands are more vulnerable to interference than the previous ones. The different GNSS signal structure and definition will be approached in next items, with an obvious emphasis on the GPS signal.

2.1.1 GPS Signal

The Navstar Global Positioning System (GPS) was conceived as an all-weather space-born ranging system, to satisfy the requirements of accurate determination of position, velocity, and time in a global reference system, anywhere, and on a continuous basis.

Despite being created for, and maintained by, military forces (the United States Department of Defense - DoD), nowadays its use is so widespread in a multitude of civilian and military applications that it would be almost impossible to think of doing some tasks without having GPS. In fact, it would be difficult to believe that a system that started to be complex and mainly developed (and used) by specialists from the military and geodesy fields, evolved in just over two decades to be acquired cheaply and manipulated easily by anyone, and anywhere.

The legacy GPS signals are transmitted on two radio frequencies in the ultrahigh frequency (UHF) band. The UHF band covers the frequencies from 300 MHz to 3 GHz.

These frequencies are referred to as L_1 and L_2 (for Link 1 and Link 2) and are derived from a common frequency, $f_0 = 10.23$ MHz:

$$f_{L1} = 154 \cdot f_0 = 1575.42 \text{ MHz} \quad (2.1)$$

$$f_{L2} = 120 \cdot f_0 = 1227.60 \text{ MHz} \quad (2.2)$$

More specifically, these signals are in the L band, which stretches from 1 to 2 GHz. The signals are composed of the following three parts:

1. *Carrier*: The carrier wave with frequencies f_{L1} or f_{L2} .
2. *Navigation data*: The navigation data contain information regarding satellite orbits, clocks, almanac, health, and other parameters. This information is uploaded to all satellites from the ground stations in the GPS Control Segment (CS). The navigation data have a bit rate of 50 bits per second (bps).
3. *Spreading sequence*: Each satellite has two unique spreading sequences or codes. The first one is the coarse acquisition code (C/A), and the other one is the encrypted precision code (P(Y)). The C/A code is a sequence of 1023 chips (a chip corresponds to a bit, and it is simply called a chip because it does not hold any information.) The code is repeated each *ms* giving a chipping rate of 1.023 MHz.

The P code is a longer code ($2.35469592765000 \times 10^{14}$ or $\approx 2.35 \times 10^{14}$ chips) with a chipping rate of 10.23 megachips per second. Each GPS is assigned a one-week segment of the P code which repeats itself each week, starting at the beginning of the GPS week, that is, at Saturday/Sunday midnight. The C/A code is only modulated onto the L_1 carrier while the P(Y) code is modulated onto both the L_1 and the L_2 carrier.

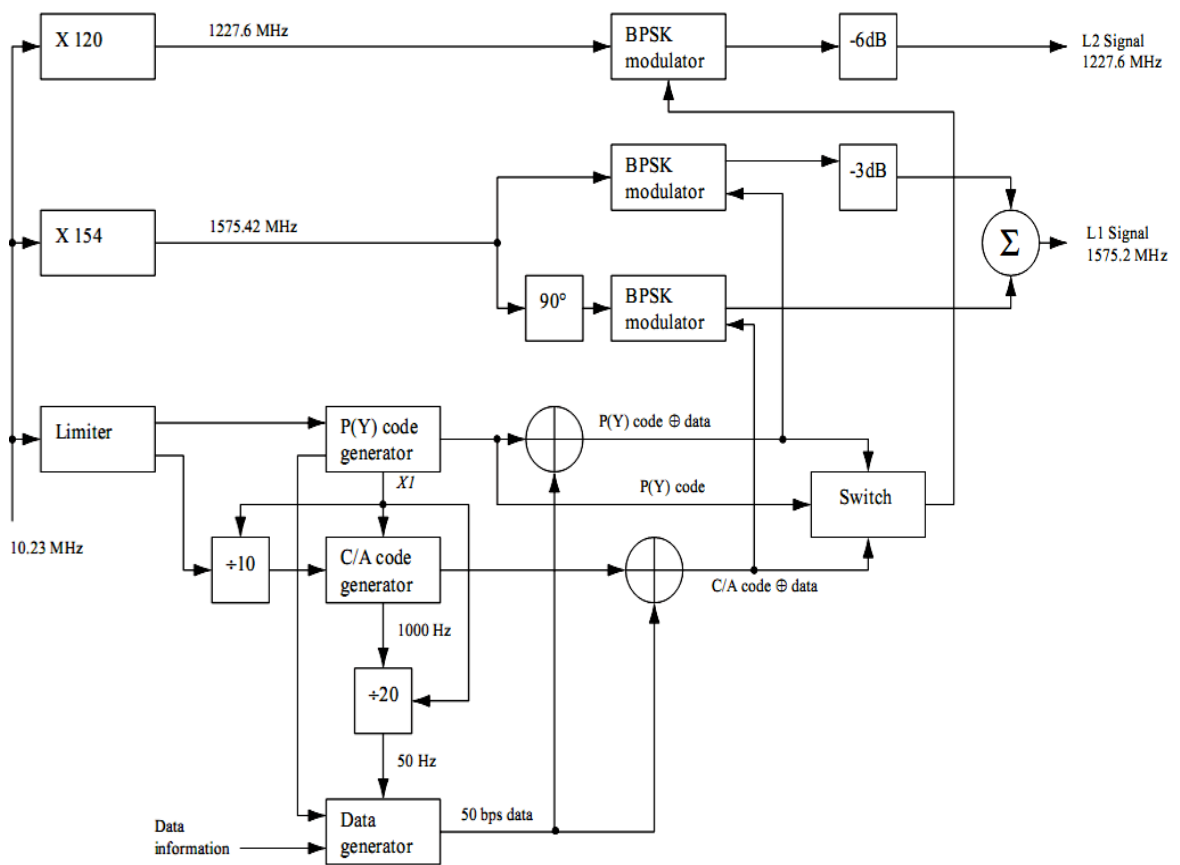


Figure 2.2: Generation of GPS signal at the satellite (Borre et al. [2007], page 18)

In the following a detailed description of the signal generation is given. Figure 2.2 is a block diagram describing the signal generation. The block diagram should be read from left to right. At the far left, the main clock signal is supplied to the remaining blocks. The clock signal has a frequency of 10.23 MHz.

Actually, the exact frequency is 10.22999999543 MHz to adjust for relativistic effects giving a frequency of 10.23 MHz seen from the user on Earth. When multiplied by 154 and 120, it generates the L_1 and L_2 carrier signals, respectively. At the bottom left corner a limiter is used to stabilize the clock signal before supplying it to the P(Y) and C/A code generators. At the very bottom the data generator generates the navigation data. The code generators and the data generator are synchronized through the $X1$ signal supplied by the P(Y) code generator.

The C/A code \oplus data and the P(Y) code \oplus data signals are supplied to the two modulators for the L_1 frequency. Here the signals are modulated onto the carrier signal using the binary phase-shift keying (BPSK) method. Note that the two codes are modulated in quadrature with each other on L_1 . That is, there is a 90° carrier-phase shift between the two signal components.

After the P(Y) part is attenuated 3 dB (analogously, the L_2 signal is attenuated by 6 dB), these two L_1 signals are added to form the resulting L_1 signal. The so-called Standard Positioning Service (SPS) is based on C/A code signals alone. It follows that the signal transmitted from satellite k can be described as:

$$\begin{aligned}
s^k(t) = & \sqrt{2P_C} [C^k(t) \oplus D^k(t)] \cos(2\pi f_{L_1} t) + \\
& \sqrt{2P_{P_{L_1}}} [P^k(t) \oplus D^k(t)] \sin(2\pi f_{L_1} t) + \\
& \sqrt{2P_{P_{L_2}}} [P^k(t) \oplus D^k(t)] \sin(2\pi f_{L_2} t)
\end{aligned} \tag{2.3}$$

where P_C , $P_{P_{L_1}}$, and $P_{P_{L_2}}$ are the powers of signals with C/A or P code, C^k is the C/A code sequence assigned to satellite number k , P^k is the P(Y) code sequence assigned to satellite number k , D^k is the navigation data sequence, and f_{L_1} and f_{L_2} are the carrier frequencies of L_1 and L_2 , respectively.

Figure 2.3 shows the three parts forming the signal on the L_1 frequency. The C/A code repeats itself every ms , and one navigation bit lasts $20ms$. Hence for each navigation bit, the signal contains 20 complete C/A sequences. The final signal is created by binary phase-shift keying (BPSK), where the carrier is instantaneously phase shifted by 180° at the time of a chip level change.

When a navigation data bit transition occurs (about one third from the right edge, as depicted in Figure 2.3), the phase of the resulting signal is also phase shifted 180° .

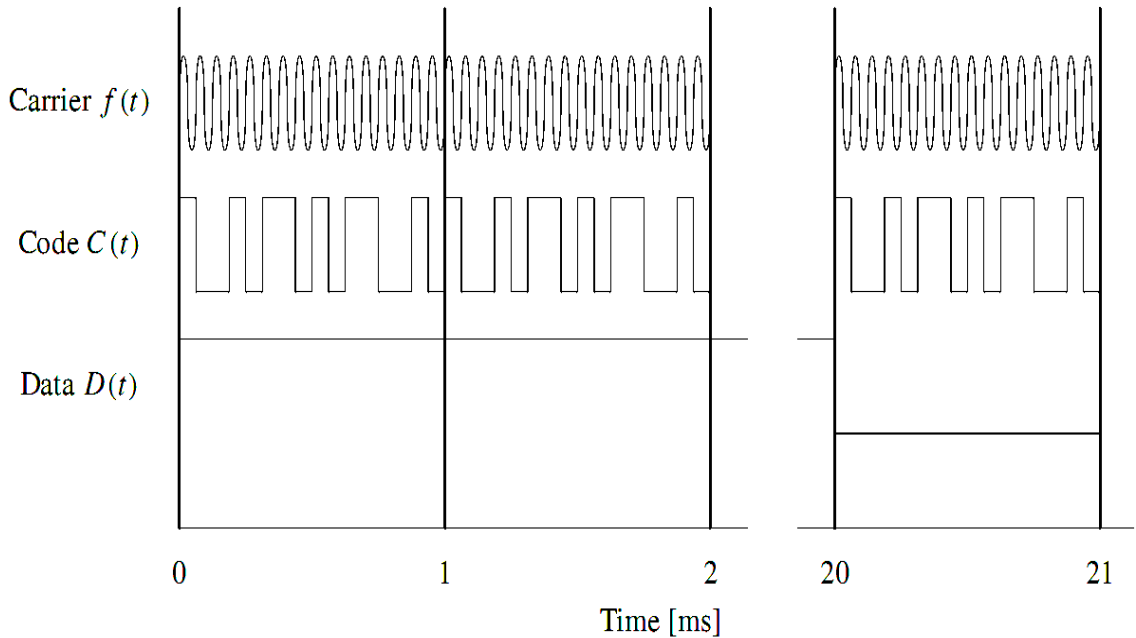


Figure 2.3: GPS L_1 signal structure (not scaled - Borre *et al.* [2007], page 20).

2.1.2 GLONASS Signal

A second configuration for global positioning is the Global Navigation Satellite System (GLONASS), placed in orbit by the former Soviet Union, and now maintained by the Russian Federation [Grewal *et al.*, 2007]. GLONASS also uses 24 satellites when in FOC (Full Operation Capability), but these are distributed approximately uniformly in three orbital planes (as opposed to six orbital planes for GPS).

But there is no doubt that what really differentiates the two systems is definitely its signal structure. The GLONASS system uses frequency-division multiple access (FDMA) of

independent satellite signals, as opposed to GPS, which uses code-division multiple access or CDMA. Its two carrier signals corresponding to L_1 and L_2 have frequencies:

$$f_1 = (1602.0 + k \times 0.5625) \text{ MHz, and } f_2 = (1246.0 + k \times 0.4375) \text{ MHz} \quad (2.4)$$

where $-7 \leq k \leq 6$ (previously $k = 0, 1, 2, \dots, 13$) is the satellite number. These frequencies lie in two bands at $L_1 = 1598.0625 - 1605.375$ MHz, and $L_2 = 1242.9375 - 1248.625$ MHz. The methods for receiving and analyzing GLONASS signals are similar to the methods used for GPS signals [Grewal *et al.*, 2007].

In fact, many commercial brands offering hybrid receivers tracking GPS/GLONASS signals are nowadays able to provide increased precision solutions using both signals within the same positioning *kernel* (providing that both signals are aligned in the same time and geodetic reference frames, making both systems increasingly interoperable).

Nevertheless, and as of September 2007, some sites revealed that a major change was in the air for GLONASS signal structure. Basically they cited that due to interoperability issues with GPS and the future European GNSS system (Galileo), GLONASS would eventually change from an FDMA to a CDMA system [GPS World, 2007].

According to preliminary statements from GLONASS developers, there will be three open and two restricted CDMA signals. The open signal L3OC is centered at 1202.25 MHz and it was introduced by GLONASS-K1 test satellite, launched in 2011. The final

GLONASS-M satellites, planned to be launched from 2014 to 2017, will also include the L3OC signal [Revnivkh, 2012].

2.1.3 Galileo Signal

The Galileo system will offer several services, a few of which are free of charge and the rest are commercial. These include the Open Service (OS), Safety of Life Service (SoL), Commercial Service (CS), Public Regulated Service (PRS), and Search and Rescue (SAR). These services span three frequency bands [Grewal *et al.*, 2007]:

$E_{5a} - E_{5b}$ Band: This band, which covers the frequency range from 1164 to 1214 MHz, contains two signals, denoted E_{5a} and E_{5b} , which are respectively centered at 1176.5 and 1207.140 MHz. E_{5a} and E_{5b} will be also be available in a combined, high performance, AltBOC signal.

E_6 Band: This band spans the frequency range from 1260 to 1300 MHz and contains a C/Nav signal (to be used by commercial services), and a G/Nav signal (used by the public regulated services), each centered at 1278.75 MHz.

$E_2 - L_1 - E_1$ Band: This band, sometimes denoted just as L_1 or E_1 for convenience, spans the frequency range from 1559 to 1591 MHz.

I will only overview the L_1 OS signal (OS for open service), because it is the correspondent to the GPS L_1 signal. The L_1 OS signal alone is expected to guarantee a horizontal accuracy, that is, 2D Root-Mean Square (RMS) better than 15m, a vertical accuracy (3D RMS) better than 35m, velocity accuracy better than 50 cm/s, and a timing accuracy better than 100 ns [Borre *et al.*, 2007].

All Galileo satellites use the same frequency bands and make use of the CDMA technique as mentioned before for GPS. Spread spectrum signals will be transmitted including different ranging codes per signal, per frequency, and per satellite. All signals are transmitted with a right-hand circular polarization, as are those for GPS and GLONASS.

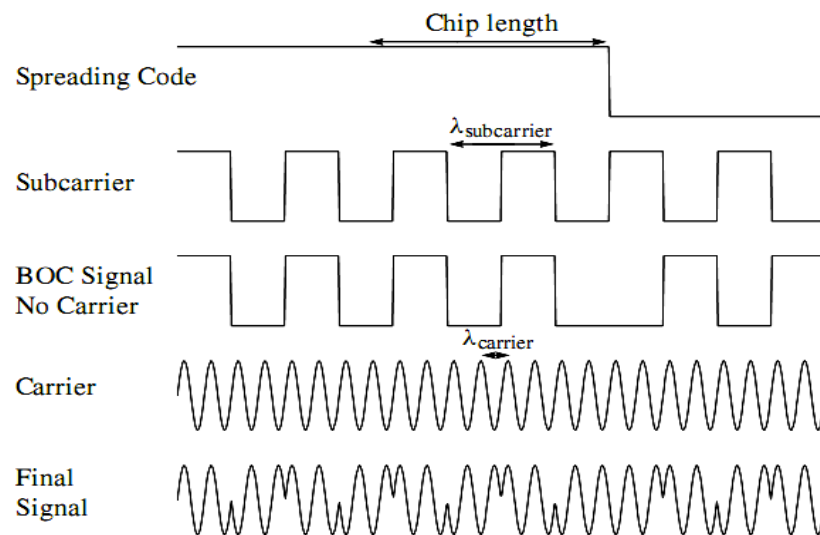


Figure 2.4: Spreading code, subcarrier, carrier and signal as result of the BOC modulation

(Borre *et al.* [2007], page 38).

The Galileo signals and the planned modernized GPS signals exhibit improved performance compared to the existing GPS signals. One of the improvements is the introduction of the binary offset carrier (BOC) modulation (Figure 2.4). BOC modulations offer two independent design parameters:

- Sub-carrier frequency f_S in MHz, and
- Spreading code rate f_C in Mchip/s.

These two parameters provide freedom to concentrate signal power within specific parts of the allocated band to reduce interference with the reception of other signals.

Furthermore, the redundancy in the upper and lower sidebands of BOC modulations offers practical advantages in receiver processing for signal acquisition, code tracking, carrier tracking, and data demodulation [Borre *et al.*, 2007].

Based on several independent research studies [Hein *et al.*, 2004] conducted mainly by European institutions, it was shown that BOC signals have a superior performance when dealing with both code pseudo-range and carrier-phase thermal noise, as well as with multipath performance. The application of the MIMICS technique with Galileo BOC signals represents a very interesting alternative to GPS or GLONASS signals. This stems mostly from two reasons:

The MIMICS algorithm is used to separate carrier-phase multipath from GPS L_1 signals, requiring at a first stage to low-pass filter the data (the same can be said about GLONASS signals). This filtering may, inadvertently, remove some multipath high frequencies that can cause the resultant MIMICS multipath correction to bias the corrected results. For BOC signals, this stage may be skipped so that the data band-pass filtering can be properly carried out focusing only on specific multipath frequencies.

The use of BOC signals will represent a major breakthrough in code multipath research. However, not much is being discussed about the multipath performance of BOC carrier-phase signals when comparing with GPS signals. This may be explained from the fact that carrier phase tracking of BOC signals is similar to carrier phase tracking of GPS BPSK signals [Pany *et al.*, 2002].

Therefore, a BOC signal is expected to have a comparable carrier phase multipath error envelope to that of a GPS carrier-phase signal, hence making the use of MIMICS with Galileo BOC signals a very interesting option.

2.2 GNSS Errors

To conclude, one should provide the GNSS pseudo-range equation relating the just mentioned signal structure and its inherent error-contaminated geometric range between the satellite and the user receiver, that is:

$$\begin{aligned}
P &= \rho + d\rho + \Delta t + T + I_{f_L} + \varepsilon_{P_{mp}} + \varepsilon_{P_{noise}} \\
\Phi &= \rho + d\rho + \Delta t + T - I_{f_L} + \varepsilon_{\Phi_{mp}} + \varepsilon_{\Phi_{noise}} + \lambda N
\end{aligned}
\tag{2.5}$$

where:

| | |
|---|---|
| P | is a pseudo-range code measurement in metres |
| Φ | is a carrier-phase measurement in metres |
| ρ | is the assumed geometric-range between the receiver and satellite |
| | in metres |
| $d\rho$ | is the satellite orbit range error in metres |
| $\Delta t = (t_R - t^S)$ | is the difference between the receiver and satellite clock biases |
| | (metres) |
| T | is the tropospheric range error in metres |
| I_{f_L} | is the ionospheric range error at the frequency f_L in metres |
| $\varepsilon_{P_{mp}}, \varepsilon_{\Phi_{mp}}$ | are the code and carrier phase multipath error in metres |
| $\varepsilon_{P_{noise}}, \varepsilon_{\Phi_{noise}}$ | are the code and carrier-phase noise error in metres |
| λN | is the carrier-phase ambiguity in metres |

2.2.1 Orbit Errors

The application of GNSS-based positioning and navigation depends substantially on how accurately the respective GNSS satellite orbit is known. For single-receiver or single

point-positioning, an orbital error is highly correlated with the positional error [Hofmann-Wellenhof *et al.*, 2001]. For the case of differential positioning, relative orbital errors are considered to be approximately equal to relative baseline errors.

Analogously, for determining precise GNSS-based velocities and accelerations it is necessary to determine precise satellite orbital velocities and accelerations (see Serrano *et al.* [2004] for details). The orbital information is either transmitted by the satellite as part of the broadcast message (i.e., the navigation message), or can be obtained in the form of precise ephemeris from several sources (being used mainly for post-processed GNSS applications, and dubbed precise ephemeris SP3 files).

The official orbit determination for GPS satellites is based on observations at the five monitor stations of the control segment (plus the more recent stations maintained by the U.S. Air Force, and the National Geospatial-Intelligence Agency – NGA). These computed orbital data can be disseminated worldwide to users as three different types of information, i.e., almanac data, broadcast ephemerides, and precise ephemerides (as a by product and usually with some latency depending on the provided product accuracy).

Their uncertainties are listed in the following table:

| Orbit Product | Uncertainty (3D RMS) | Remark |
|----------------------|-----------------------------|------------------------------|
| Almanac | Some kilometres | Depending on the age of data |
| Broadcast | 1-2m | Or even better |
| Precise | Few centimetres to 0.20m | Depending on the delay |

Table 2.1: Uncertainties of ephemeris

2.2.2 Satellite and Receiver Clock Errors

The traveling time between satellite S and receiver R is denoted τ_R^S , taking on values of approximately 70 ms. Let c denote the velocity of light in vacuum, and the pseudo-range P_R^S is defined as:

$$t_R - t_S = \tau_R^S = \frac{P_R^S}{c} \quad (2.6)$$

Let any epoch in GPS time (GPST) be called t^{GPS} . The clock at satellite S and the clock at receiver R do not run perfectly aligned with GPST. Thus, we introduce the receiver clock offset dt_R defined as:

$$t_R = t^{GPS} + dt_R \quad (2.7)$$

and the satellite clock offset dt^S as:

$$t^S = (t_R - \tau_R^S)^{GPS} + dt^S \quad (2.8)$$

Any GNSS satellite always contain atomic clocks (in fact that is one of the premises of a global satellite navigation system), thus the clock behavior can be accurately modeled using a second-order polynomial function. The polynomial coefficients (a_0 , a_1 , and a_2 although it is often zero) and are provided within the navigation message to model the satellite clock such as:

$$dt^S = a_0 + a_1(t^S - t_{oe}) + \dots \quad (2.9)$$

Receiver clocks dt_R , on the other hand, are low quality for commercial and practical reasons, therefore the receiver clock bias is estimated as a nuisance parameter (of no interest to us), along the other unknown parameters such as receiver coordinates, usually on an epoch-by-epoch basis.

2.2.3 Ionospheric Error

The ionosphere can be considered as the part of the Earth's atmospheric region that has enough ionized molecules and free electrons to significantly affect radio wave propagation. The main physical quantity adopted to characterize the ionosphere is the spatial and temporal distribution of the number of free electrons per volume unit. Consider a single electromagnetic wave propagating in space with wavelength λ and frequency f . The velocity of its phase:

$$v_{phase} = \lambda \cdot f \quad (2.10)$$

and is denoted phase velocity. For a group of waves with slightly different frequencies, the propagation of the resultant energy is defined by the group velocity [Hofmann-Wellenhof *et al.*, 2001]:

$$v_{group} = -\frac{df}{d\lambda} \lambda^2 \quad (2.11)$$

This velocity has to be considered for GNSS code measurements. A relation between phase and group velocity may be obtained using the Rayleigh equation:

$$v_{group} = v_{phase} - \lambda \frac{dv_{phase}}{d\lambda} \quad (2.12)$$

Phase and group velocity are equal in non-dispersive media as is the speed of light in *vacuum*. The wave propagation in a medium depends on the refractive index n . Generally the propagation velocity for the corresponding refractive indices n_{phase} and n_{group} is obtained from:

$$\begin{aligned} v_{phase} &= \frac{c}{n_{phase}} \\ v_{group} &= \frac{c}{n_{group}} \end{aligned} \quad (2.13)$$

These two equations have a very important physical connotation within atmospheric propagation, i.e., the larger the refractive index the smaller the velocity, therefore resulting in proportional signal-path magnitude changes (with longer lengths for the group and smaller for the phase signal-path).

Numerous ionospheric models have been proposed and implemented by not only the GPS/GNSS community, but also the atmospheric research community in general. The basic model of the ionosphere that the Wide-Area Augmentation System (WAAS) has implemented is a thin-shell approximation depicted in Figure 2.5 [Hansen, 2000]:

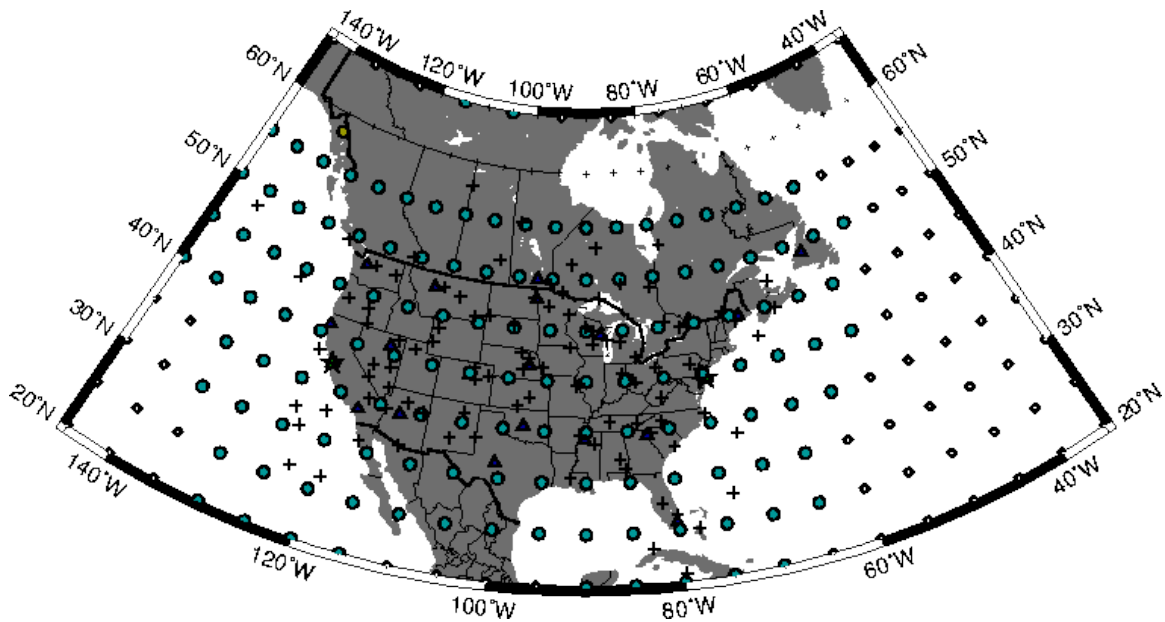


Figure 2.5: Ionospheric model broadcast by the WAAS system. It consists of a thin shell at 350 Km altitude which is discretized into a geodetically rectangular grid. A vertical delay estimate and a confidence bound on that estimate are made at each grid vertex.

This collapses the variation of the ionosphere's electron density distribution into an impulse function in the radial direction. The thin-shell approximation creates a vertically equivalent ionosphere that varies only with latitude, longitude, and time. The transformation is carried out by a non-linear mapping called the obliquity factor [Hansen, 2000].

The more generic physical explanation of the ionosphere and its inherent properties is given in next figure:

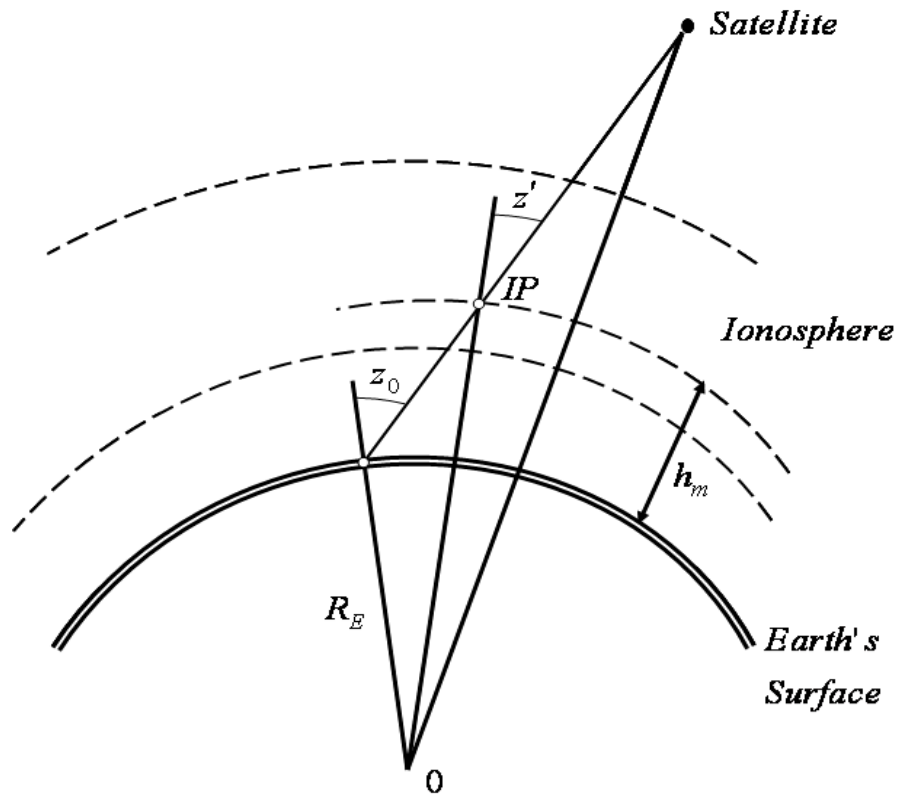


Figure 2.6: Ionospheric geometric path delay assuming a single-layer model. IP is the ionospheric Pierce point, z_0 and z' are the zenith angles at the ionosphere point and at the observing site, and R_E is the Earth's mean-radius [Hofmann-Wellenhof *et al.*, 2001].

As depicted in Figure 2.6, the ionosphere, extending in various layers from a minimum height (h_m) of about 50km, to 1000km (represented by the outer layer in the Figure) above the Earth, is a dispersive medium with respect to GNSS signals. The phase refractive index, n_{phase} , can be approximated by the series:

$$n_{phase} = 1 + \frac{\alpha_2}{f^2} + \frac{\alpha_3}{f^3} + \frac{\alpha_4}{f^4} + \dots \quad (2.14)$$

The coefficients α_2 , α_3 , and α_4 do not depend on frequency but on the quantity N_e denoting the number of electrons *per* cubic meter (i.e., the electron density) along the propagation path [Hofmann-Wellenhof *et al.*, 2001]. The coefficient α_2 can be approximated with a value of:

$$\alpha_2 = -40.3 \cdot N_e \text{ [Hz}^2\text{]} \quad (2.15)$$

Now, and just looking at Equation 2.10, we can see that $n_{group} > n_{phase}$, thus, $v_{group} < v_{phase}$ therefore, and as a consequence of the different velocities, signal measurements are delayed when represented by code pseudo-range observables, and are advanced when represented by carrier-phases. The magnitude of these signal-path changes can be quantitatively obtained by using just up to the second-order term of (Equation 2.14), and by using the α_2 value, i.e.:

$$n_{phase} = 1 - \frac{40.3N_e}{f^2} \quad (2.16)$$

When talking about this effect along the propagation signal path (column of number of electrons *per* cubic meter), then we have to integrate along the path from the satellite to the receiver. This is done through an integral (Fermat's principle), and with some mathematical manipulation one obtains [Hofmann-Wellenhof *et al.*, 2001]:

$$\Delta Iono_{phase} = -\frac{40.3}{f^2} \int N_e ds, \text{ and } \Delta Iono_{group} = \frac{40.3}{f^2} \int N_e ds \quad (2.17)$$

where ds means measured from the satellite to the user receiver. Now, defining TEC (Total Electron Content) as:

$$TEC = \int N_e ds \quad (2.18)$$

and substituting into Equation 2.17, we obtain:

$$\Delta Iono_{phase} = -\frac{40.3}{f^2} TEC, \text{ and } \Delta Iono_{group} = \frac{40.3}{f^2} TEC \quad (2.19)$$

TEC is given in TEC units (TECU), where 1 TECU = 10^{16} electrons *per* m^2 . Fortunately, and due to the dispersive nature of the ionosphere, GNSS users with dual-frequency

receivers can correct for the ionospheric range error (at least first-order errors) through an appropriate combination of measurements observed on L_1 and L_2 .

In the near future, more GNSS signals with multiple frequencies will be available on both GPS and Galileo, thus we should expect an improvement in ionospheric modeling error and mitigation.

2.2.4 Tropospheric Error

A radio signal travelling through the neutral atmosphere (i.e., and contrarily to the ionosphere, the un-ionized part) suffers a delay mostly due to the lowest-most region of the atmosphere, the troposphere, which can be defined at the zenith (zenith tropospheric delay) as:

$$d_{trop}^z = \int_{R_S}^{R_A} [n(r) - 1] dr = 10^{-6} \int_{R_S}^{R_A} N dr \quad (2.20)$$

where n is the refractive index, N is the refractivity (as seen before), R_S is the station geocentric radius and R_A the radius of the top of the neutral atmosphere [Mendes *et al.*, 1995]. The zenith tropospheric delay is usually divided into two components, designated as hydrostatic (or dry) and wet (see Figure 2.7):

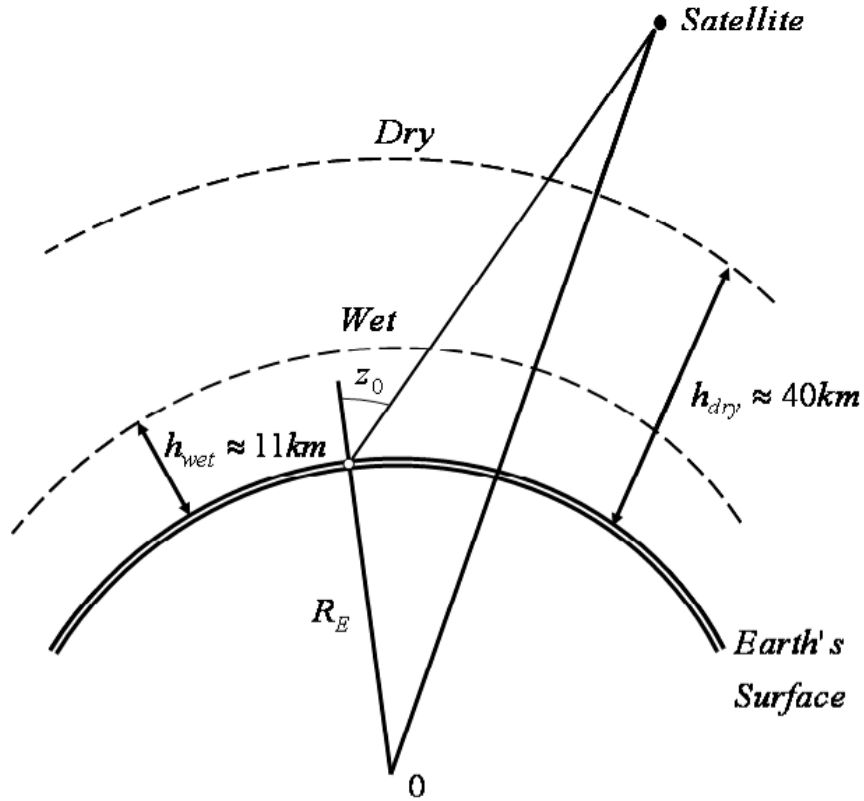


Figure 2.7: Thickness of poly-tropic layers for the troposphere [Hofmann-Wellenhof *et al.*, 2001].

The hydrostatic component of the zenith delay can be modeled very accurately provided good station pressure measurements are available. At low-elevation angles, partial derivatives of the hydrostatic and wet delays are sufficiently different as to cause errors in the estimates of station heights and zenith total delays, unless accurate surface pressure values are used to model the hydrostatic delay [Tregoning and Herring, 2006].

The wet component (included in the layer from the Earth's surface up to 11km where all the meteorological conditions are formed) is spatially and temporally highly variable and poorly predicted by models.

About 90% of the tropospheric refraction arises from the dry component, and the remaining 10% from the wet component. Therefore, even though the wet component represents the smallest part of the troposphere it is, however, responsible for most of the tropospheric refraction.

The zenith delay can be related to the delay that the signal would experience at other elevation angles through the use of mapping functions. If the mapping functions are determined separately for the hydrostatic and the wet component, the tropospheric delay can be expressed as:

$$d_{trop} = d_{hydrostatic}^z \cdot m_{hydrostatic}(\epsilon) + d_{wet}^z \cdot m_{wet}(\epsilon) \quad (2.21)$$

where $d_{hydrostatic}^z$ is the zenith delay due to mostly dry gases, d_{wet}^z is the zenith delay due to water-vapor, m_h is the hydrostatic component mapping function, m_w is the wet component mapping function, and ϵ is the non-refracted elevation angle at the ground station. Many tropospheric models have been developed throughout the years for precise navigation.

However, throughout this dissertation we use the Geodetic Research Laboratory (University of New Brunswick, Canada) developed UNB3 troposphere prediction model [Collins and Langley, 1997], which is based on the zenith delay algorithms of Saastamoinen [1973], the mapping functions of Niell [1996], and a table of sea-level atmospheric values derived from the U.S. 1966 Standard Atmosphere Supplements, and lapse rates to scale the sea-level values to the receiver height.

2.2.5 Multipath Error

GNSS multipath, as the name perfectly describes it, is the effect when a GNSS satellite-emitted signal arrives at the user receiver via more than one path. Multipath is mostly caused by high-reflecting surfaces near the receiver (see next figure for such an example). Secondary effects include reflections at the satellite (mainly at the satellite's solar panels) during signal transmission, but usually they are considered to have a residual effect; therefore it has not been given too much attention.

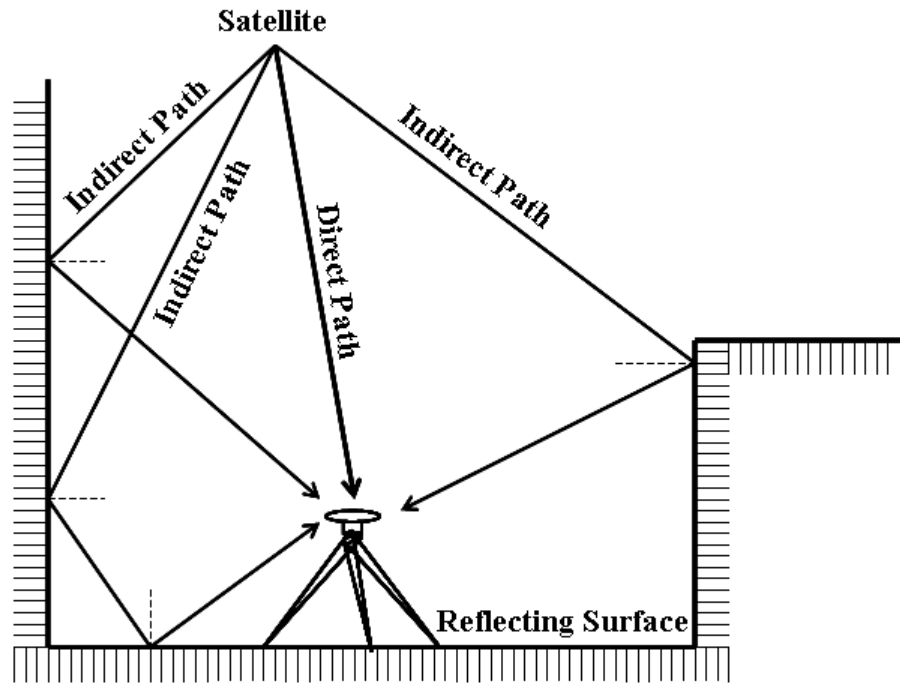


Figure 2.8: Geometry of multiple multipath specular reflections upon a static GNSS receiver

The multipath error is scaled according to the wavelength, and with today's current narrow-correlator-spacing technology receivers it is known that it can have magnitudes of a few metres, and a few centimetres for code pseudo-range observations, and carrier-phase observations, respectively. In severe cases, loss-of-lock may even occur.

In Figure 2.8, only specular reflections are depicted. However, multipath effects on GNSS signals are not limited to smooth reflections arising from so-called specular reflectors, but also arise from irregular surfaces, vegetation and foliage. In these cases, multipath signal reflections tend to have a more quasi-random signature thus depicting

the reflection-surface irregularity (i.e. with higher-frequency components within the signal *spectrum*) such as in multipath diffraction, and scattering.

Moreover, and as mentioned in the introductory chapter, GNSS signal multipath is not limited to static receiver scenarios, but rather to many kinematic platforms as well. This plurality of multipath reflection characteristics under different platform dynamics and reflection conditions will receive more attention in the following chapter. For the time being, a simple geometric approach to describe typical carrier-phase multipath modeling will be derived.

The effect of multipath on carrier phases has been thoroughly studied, at least since the end of the 1980s and beginning of the 1990s. A seminal work on a geometric carrier-phase multipath equation was developed during that time by Georgiadou and Kleusberg [1988], and later studied and applied to permanent reference stations by Elósegui *et al.* [1995].

Because of its continued importance to current carrier-phase multipath mitigation techniques the derivation of this equation will be overviewed following Hofmann-Wellenhof *et al.* [2001] (although as it will be seen in the next chapter, this equation relies on a rather simplistic approach that the reflection arises from a strong flat reflector). The direct and indirect signals interfere at the antenna center and may be represented by:

$$\begin{aligned}
a \cos \varphi &= \text{direct signal} \\
\beta a \cos(\varphi + \Delta\varphi) &= \text{indirect signal}
\end{aligned} \tag{2.22}$$

where a and φ denote the amplitude and phase of the direct signal. The amplitude of the indirect signal is reduced by the damping factor β because of the reflection at the surface (material-dependent reflection / refraction characteristics). The phase of the indirect signal is delayed by the phase shift $\Delta\varphi$, which is a function of the geometric configuration (relative position between GNSS receiver, reflector, and satellite geometry). Now, adding algebraically the two sinusoidal terms we obtain:

$$a \cos \varphi + \beta a \cos(\varphi + \Delta\varphi) \tag{2.23}$$

Using some trigonometric manipulations on Equation 2.23 one can easily obtain (for more details please see Georgiadou and Kleusberg [1988]):

$$\tan(\Delta\varphi_M) = \frac{\beta \sin(\Delta\varphi)}{1 + \beta \cos(\Delta\varphi)} \Leftrightarrow \Delta\varphi_M = \tan^{-1} \left[\frac{\beta \sin(\Delta\varphi)}{1 + \beta \cos(\Delta\varphi)} \right] \tag{2.24}$$

where $\Delta\varphi_M$ is the angular phase-multipath error. This equation, though rather simplistic, is of extreme importance throughout this dissertation (albeit having different representations), and can provide an idea of carrier-phase multipath behavior just based on the variation of the damping factor (top plot), and phase-delay error (bottom plot) in Figure 2.9:

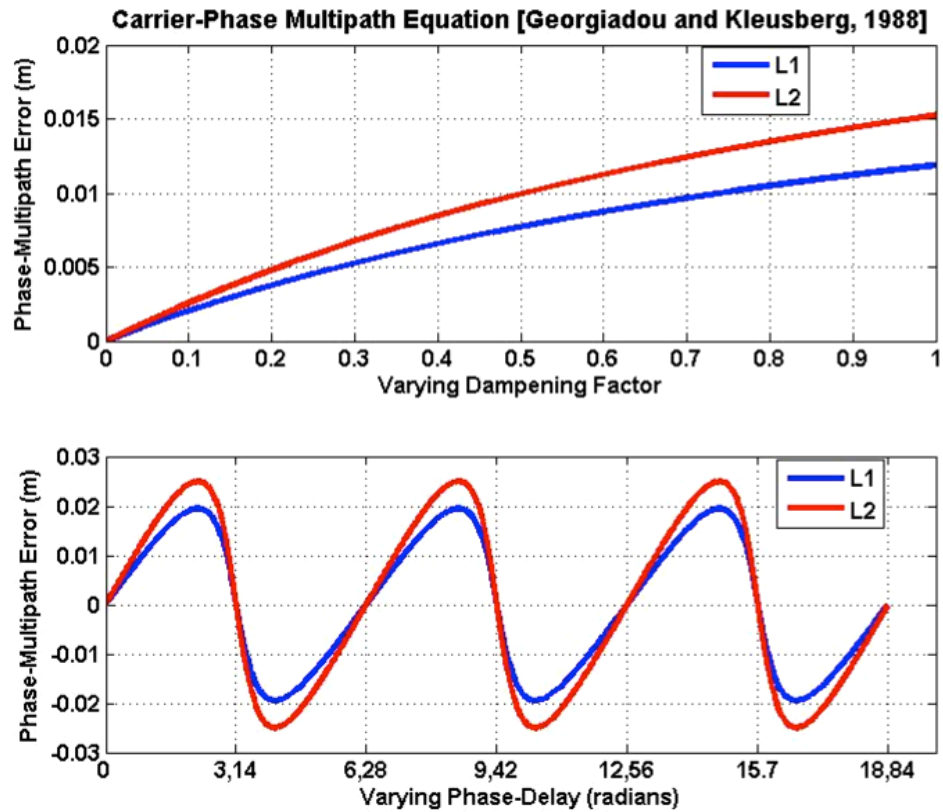


Figure 2.9: Carrier-phase multipath behavior varying the damping-factor and keeping the phase-delay error at 45 degrees (top), and varying the phase-delay error and keeping the damping-factor at 0.6

The theoretical maximum effect of multipath on carrier-phase measurements occurs for $\Delta\varphi_M = 90^\circ = 1/4$ cycle. Converting this phase error to range, and scaling to L_1 for instance, we obtain a maximum error of approximately 5cm (although is rarely seen).

2.2.6 Random Errors

The noise term consists of receiver measurement noise and the sum of all other unmodeled and second-order effects (for instance, second-order ionospheric and tropospheric refraction).

It is also a function of the GNSS-receiver technology used (receiver and antenna hardware), where geodetic-quality receivers will have much better noise envelopes than, say, hand-held receivers. This is obviously reflected in their respective prices.

Overall, the random noise mainly contains the actual observation noise plus random constituents of multipath, especially within kinematic applications (i.e., high-frequency uncorrelated multipath components). The two observables (code and phase) pseudo-range noise is summarized in next table:

| Range | Noise |
|------------------------------|---------------|
| Code range (C/A-code) | 10 – 300 cm |
| Code range (P-code) | 10 – 30 cm |
| Phase range | 0.2 – 5 mm |

Table 2.2: Typical GPS range noise figures [Hofmann-Wellenhof *et al.*, 2001]

2.3 Extended Kalman Filter

The Kalman filter is an extremely effective and versatile procedure for combining noisy sensor outputs to estimate the *state* (vector of unknown parameters) of a system with uncertain dynamics [Grewal *et al.*, 2007]. The noisy sensors could be just GNSS receivers (it seems as though the Kalman filter was tailored to fit navigation sensors), speed sensors, inertial sensors, altimeters, water-speed sensors, etc.

The system state in question includes position, velocity, acceleration, but may also include nuisance parameters such as clock bias, or time-correlated noise sources. Uncertain dynamics include unpredictable disturbances of the host dynamic platform, caused either by a human operator or by the environment (wind, terrain topography, blockages, etc.).

Although developed for linear systems, its main use has been in dealing with non-linear systems and sensors, in which case one has to use the approach due to Stanley F. Schmidt [Novoselov *et al.*, 2005], the extended Kalman filter (throughout this dissertation, just EKF). In this sense non-linear sensors can be represented in the form:

$$z_k = h_k(x_k) + v_k \quad (2.25)$$

Where z_k is the sensor-measurement vector, x_k is the state-vector, $h_k(x_k)$ is a smoothly differentiable function of x_k , and v_k is the vector of residuals. The essential EKF equations are summarized in two blocks. The first is the predictor (time updates):

$$\text{Predicted state vector:} \quad \hat{x}_k^- = \hat{x}_{k-1}^+ + \int_{t_{k-1}}^t f(\hat{x}, t) dt \quad (2.26)$$

$$\text{Predicted covariance matrix:} \quad P_k^- = \Phi_k \cdot P_{k-1}^+ \cdot \Phi_k^T + Q_{k-1} \quad (2.27)$$

and the second is the corrector (measurement updates):

$$\text{Kalman gain:} \quad K_k = P_k^- \cdot H_k^T [H_k \cdot P_k^- \cdot H_k^T + R_k]^{-1} \quad (2.28)$$

$$\text{Corrected state estimate:} \quad \hat{x}_k^+ = \hat{x}_k^- + K_k \cdot [z_k - h_k(\hat{x}_k^-)] \quad (2.29)$$

$$\text{Corrected covariance matrix:} \quad P_k^+ = P_k^- - K_k \cdot H_k \cdot P_k^- \quad (2.30)$$

where f is the function driving the system dynamics, Φ_k is the transition matrix, Q_k is the process-noise matrix, and K_k is the Kalman gain. H_k is the *Jacobian* matrix, that is, a matrix consisting of the partial derivatives of the measurements in order to the unknown parameters. Therefore, it is also known as a sensitivity matrix, as it “maps” the influence of the measurements in order to the parameters (or vice-versa)

2.4 Adaptive Estimation

Temporal models are used to relate one epoch's state to the next. This is accomplished using an assumption about the stochastic behavior of the estimated parameter over time. If a parameter is static and constant over time then one epoch will directly relate to the next. Consequently, the one epoch's estimated parameters and estimated variance-covariance can be used as a-priori information for the following epoch.

The reverse case (infinite white noise) is also trivial. If the parameters from one epoch have no relationship with the next epoch's parameters then no information from one epoch can be passed to the next. In this case the state vector from the one epoch can be used as a point of expansion for the next epoch with an infinite variance (i.e., no information).

All the cases in between can be described by a system of differential equations that relate one epoch to the next. This system of differential equations defines the transition from one epoch to the next and, to some extent, the change in variance-covariance from one epoch to the next. Two common, time-varying systems are a random-walk process and a first order *Gauss-Markov* process. These processes are described in Gelb [1974].

A random walk process is best described by a roaming value that changes by a discrete step randomly increasing or decreasing from the previous value. All the future values are tied to the current value; however, the likelihood that the future value and the current

value are the same decreases over time. In terms of temporal modeling, the current value of the parameter is used as the a-priori estimate for the next epoch but due to the decreased likelihood that the value is the same, the estimated variance of the parameter is increased from one epoch to the next. The update equations from one epoch to the next for a random-walk process are:

$$\begin{cases} x_{k+1} = x_k \\ \sigma_{x_{k+1}}^2 = \sigma_{x_k}^2 + q\Delta t \end{cases} \quad (2.31)$$

where x is the value of the random-walk parameter, σ^2 is the estimated variance of the parameter, q is the spectral density (which describes the variability of the parameter over time), and Δt is the difference in time between the last update and the next. A Gauss-Markov process is described by the differential equation [Gelb, 1974]:

$$\dot{x} = -\beta x + w \quad (2.32)$$

It produces a characteristic decreasing autocorrelation function. It is commonly used in prediction because of the behavior of the estimate over time. Initially, the predicted update is the same as the latest estimate and over time the estimate converges to zero. For this reason, it is a conservative estimation choice for many estimated parameters. The update equations for a first order Gauss-Markov process are:

$$\begin{cases} x_{k+1} = e^{-\beta\Delta t} x_k \\ \sigma_{x_{k+1}}^2 = \sigma_{x_k}^2 + \frac{q}{2\beta} (1 - e^{-2\beta\Delta t}) \end{cases} \quad (2.33)$$

In the precise carrier phase positioning filters usually there are four types of states: ambiguities, slant ionosphere error, position, and velocity. Within this dissertation, carrier-phase multipath is another state. Ambiguities and static positions are usually modeled as random constants (static states), whereby one epoch's parameter estimate is used as a-priori information for the next epoch. Slant ionosphere error and velocity are time-varying states, which change somewhat from epoch to epoch. The system dynamics model for the position and velocity states, when the velocity is estimated as a first order Gauss-Markov process, is:

$$\begin{cases} \dot{x} = \dot{x} \\ \ddot{x} = -\beta\dot{x} + w \end{cases} \quad (2.34)$$

where x is the position state, \dot{x} is the velocity state, \ddot{x} is the acceleration, β is the rate of decline of the velocity over time and w is the white noise error associate with the propagation error. In matrix form the system model is given by:

$$\begin{bmatrix} \dot{x} \\ \ddot{x} \end{bmatrix} = \begin{bmatrix} 0 & 1 \\ 0 & -\beta \end{bmatrix} \begin{bmatrix} x \\ \dot{x} \end{bmatrix} + \begin{bmatrix} 0 \\ w \end{bmatrix} \quad (2.35)$$

This system of equations can be solved using a Taylor series expansion [Gelb, 1974]. The expansion about t_0 is:

$$x(t) = x(t_0) + \dot{x}(t_0)(t - t_0) + \ddot{x}(t_0) \frac{(t - t_0)^2}{2!} + \ddot{\ddot{x}}(t_0) \frac{(t - t_0)^3}{3!} + \dots \quad (2.36)$$

The expansion can be related to the system model by:

$$x(t) = x(t_0) + F \cdot \Delta t \cdot x(t_0) + \frac{F^2 \cdot \Delta t^2}{2!} x(t_0) + \frac{F^3 \cdot \Delta t^3}{3!} x(t_0) + \dots \quad (2.37)$$

where

$$F = \begin{bmatrix} 0 & 1 \\ 0 & -\beta \end{bmatrix} \quad (2.38)$$

This expansion in terms of the matrix F is:

$$\begin{bmatrix} x \\ \dot{x} \end{bmatrix} = \left(I + \sum_{i=1}^{\infty} \begin{bmatrix} 0 & -\beta^{i-1} \\ 0 & -\beta^i \end{bmatrix} \frac{\Delta t^i}{i!} \right) \begin{bmatrix} x(t_0) \\ \dot{x}(t_0) \end{bmatrix} = \begin{bmatrix} 1 & a \\ 0 & b \end{bmatrix} \begin{bmatrix} x(t_0) \\ \dot{x}(t_0) \end{bmatrix} \quad (2.39)$$

where a and b are the elements of the matrix to be simplified in the following derivation:

$$a = \Delta t - \beta \frac{\Delta t^2}{2!} + \beta^2 \frac{\Delta t^3}{3!} + \dots \quad (2.40)$$

$$1 - \beta a = 1 - \beta \Delta t + \beta^2 \frac{\Delta t^2}{2!} - \beta^3 \frac{\Delta t^3}{3!} + \dots \quad (2.41)$$

which can be replaced using the definition of the Taylor series expansion of an exponential decay function in the following form:

$$e^\alpha = 1 + \alpha + \frac{\alpha^2}{2!} + \frac{\alpha^3}{3!} + \dots \quad (2.42)$$

resulting in:

$$a = \frac{1 - e^{-\beta \Delta t}}{\beta} \quad (2.43)$$

A similar derivation can be made for the solution of b :

$$b = 1 - \beta \Delta t + \frac{\beta^2 \Delta t^2}{2!} - \frac{\beta^3 \Delta t^3}{3!} + \dots = e^{-\beta \Delta t} \quad (2.44)$$

The transition matrix, which relates one epoch to the next, is then:

$$\Phi = \begin{bmatrix} 1 & \frac{1 - e^{-\beta \Delta t}}{\beta} \\ 0 & e^{-\beta \Delta t} \end{bmatrix} \quad (2.45)$$

The propagation's effect on the covariance matrix is based on the noise term (w). If:

$$G = \begin{bmatrix} 0 & 0 \\ 0 & 1 \end{bmatrix} \quad (2.46)$$

then the propagation's effect on the variance-covariance matrix is defined by the following (hereafter the temporal propagation is assumed to be from t_0 to t):

$$\begin{aligned} Q_{ww} &= \int_0^t \Phi G Q G^T \Phi^T dt = \int_0^t \begin{bmatrix} 1 & \frac{1-e^{-\beta t}}{\beta} \\ 0 & e^{-\beta t} \end{bmatrix} \begin{bmatrix} 0 & 0 \\ 0 & 1 \end{bmatrix} \begin{bmatrix} 1 & 0 \\ \frac{1-e^{-\beta t}}{\beta} & e^{-\beta t} \end{bmatrix} (q) dt \\ &= \int_0^t (q) \begin{bmatrix} \left(\frac{1-e^{-\beta t}}{\beta} \right)^2 & \frac{1-e^{-\beta t}}{\beta} e^{-\beta t} \\ \frac{1-e^{-\beta t}}{\beta} e^{-\beta t} & e^{-\beta t} \end{bmatrix} dt \end{aligned} \quad (2.47)$$

where q is the estimated parameter spectral amplitude. The integrals of each of the elements of this matrix can be calculated independently and will not be demonstrated here. The update (using the transition matrix) of the state parameters is given by:

$$\begin{cases} x_{k+1} = \Phi x_k \\ P_{x_{k+1}|x_{k+1}} = \Phi P_{x_k|x_k} \Phi^T + Q_{ww} \end{cases} \quad (2.48)$$

Finally, and in terms of a position and velocity (PV) system, where the velocity is modeled as a first order Gauss-Markov process, the state update-equation is:

$$\begin{bmatrix} x \\ \dot{x} \end{bmatrix}_{k+1} = \begin{bmatrix} 1 & \frac{1-e^{-\beta\Delta t}}{\beta} \\ 0 & e^{-\beta\Delta t} \end{bmatrix} \begin{bmatrix} x \\ \dot{x} \end{bmatrix}_k \quad (2.49)$$

and the covariance matrix update equation is:

$$P_{x_{k+1}|x_{k+1}} = \begin{bmatrix} 1 & \frac{1-e^{-\beta\Delta t}}{\beta} \\ 0 & e^{-\beta\Delta t} \end{bmatrix} P_{x_k|x_k} \begin{bmatrix} 1 & 0 \\ \frac{1-e^{-\beta\Delta t}}{\beta} & e^{-\beta\Delta t} \end{bmatrix} + \begin{bmatrix} a_{11} & a_{12} \\ a_{21} & a_{22} \end{bmatrix} \quad (2.50)$$

where:

$$a_{11} = \frac{q}{\beta^3} \left(-\frac{3}{2} + \beta t + 2e^{-\beta t} - \frac{1}{2}e^{-2\beta t} \right),$$

$$a_{12} = a_{21} = \frac{q}{\beta^2} \left(\frac{1}{2} - e^{-\beta t} + \frac{1}{2}e^{-2\beta t} \right),$$

and

$$a_{22} = \frac{q}{2\beta} (1 - e^{-2\beta t})$$

Similar equations can be easily derived for the Gauss-Markov 1st-order position-velocity-acceleration model (PVA). In this dissertation, and as it will be seen later, a PVA model

is more suitable to carrier-phase multipath modeling due to the high-frequency nature of multipath environments in kinematic/urban scenarios. In this case the transition matrix would be given by:

$$\begin{bmatrix} x \\ \dot{x} \\ \ddot{x} \end{bmatrix}_{k+1} = \begin{bmatrix} 1 & \Delta t & \frac{\beta\Delta t + e^{-\beta\Delta t} - 1}{\beta^2} \\ 0 & 1 & \frac{1 - e^{-\beta\Delta t}}{\beta^2} \\ 0 & 0 & e^{-\beta\Delta t} \end{bmatrix} \begin{bmatrix} x \\ \dot{x} \\ \ddot{x} \end{bmatrix}_k \quad (2.51)$$

2.5 Whitening Filters

Data whitening arises in a variety of contexts in which it is useful to decorrelate a data sequence either prior to subsequent processing, or to control the spectral shape after processing [Eldar and Oppenheim, 2002]. One example in which data whitening has been used to advantage includes improving the correct detection of underlying signals of interest within multi-signature systems.

This is typical in GNSS signal phase-multipath detection in kinematic scenarios, where adding to the original multipath reflections there are other error sources, including biases which can be properly modeled but their higher-order effects still remain, plus the usual receiver noise.

The technique developed in this dissertation to detect and mitigate carrier-phase multipath signals in dynamic scenarios, dubbed MIMICS (**M**ultipath Profile from **B**etween **R**eceIver **D**yna**M**ICS), resorts to pre-whitening of carrier-phase differenced data to obtain between-receiver multipath observables [Serrano *et al.*, 2006]. Although an initial decorrelation of multipath data can be performed through mechanical randomization, a dedicated whitening algorithm is implemented in order to guarantee consistency and thoroughness.

Let $\mathbf{a} \in \mathfrak{R}^m$ denote a random vector of carrier-phase multipath-contaminated data (therefore with time-correlation) with positive-definite covariance matrix \mathbf{C}_a . We wish to “whiten” the vector \mathbf{a} using a whitening transformation \mathbf{W} to obtain the random vector $\mathbf{b} = \mathbf{W} \cdot \mathbf{a}$, where the covariance matrix of \mathbf{b} is given by $\mathbf{C}_b = c^2 \cdot \mathbf{I}_m$ for some $c > 0$. Thus we seek a transformation \mathbf{W} such that:

$$\mathbf{C}_b = \mathbf{W} \cdot \mathbf{C}_a \cdot \mathbf{W}^T = c^2 \cdot \mathbf{I}_m \quad (2.52)$$

for some constant $c > 0$, and \mathbf{I}_m is the identity matrix with dimension $m \times m$. We refer to any \mathbf{W} satisfying Equation 2.48 as a whitening transformation. However, there are an unlimited number of ways of choosing \mathbf{W} but only when the “whiten” vector $\mathbf{b} = \mathbf{W} \cdot \mathbf{a}$ is as close as possible to the original vector \mathbf{a} , then we say that \mathbf{W} is an optimal whitening transformation [Eldar and Oppenheim, 2002].

Paralleling the concept of least-squares *orthogonalization* used, for instance, in the LAMBDA method for decorrelation of float ambiguities in GPS-RTK [Teunissen, 1996], in the MIMICS technique we develop an optimal linear whitening transformation for obtaining multipath observables.

The optimality arises from choosing a whitening transformation that does not introduce any distortion in data, and minimizes the mean-squared-error (MSE) between the original and whitened data; i.e., that result in a white output that is as close as possible to the input, in an MSE sense. This algorithm will be described in chapter five, where it will be depicted that the optimal whitening transformation is obtained through the Yule-Walker method for AR (auto-regressive) model parameter estimation.

2.6 RTK-based GNSS Heading/Attitude Systems

The theory of attitude determination using multiple GNSS antennas is well documented in the literature. If the relative position of two antennas can be determined with a sub-centimeter accuracy using carrier-phase observables, two of the three attitude parameters, usually heading (yaw - ψ) and pitch (θ), or heading and cross-slope (roll - γ), can be estimated [Keong and Lachapelle, 2000].

Heading is the rotation angle about the z -axis (up), positive clockwise, and pitch is the rotation angle about the rotated x -axis (east), positive upward:

$$\psi = \arctan \frac{\Delta E}{\Delta N} \qquad \theta = \arctan \left(\frac{\Delta Up}{\sqrt{\Delta E^2 + \Delta N^2}} \right) \qquad (2.53)$$

We can see some examples of RTK-based GNSS dual-antenna systems:



Figure 2.10: GNSS dual-antenna system located on a motor-grader's blade (Trimble GCS900 on a motor-grader with dual GPS – Trimble website).

In Figure 2.10 we can see a motor-grader with the two masts connected to the blade, having in both sides GNSS receivers serving as a positioning and orientation device. Likewise, in Figure 2.11, the dozer blade has both masts equipped as well with GNSS receivers.

As we can see, most of the time only two attitude angles are necessary and sufficient, and they can be easily derived once the baseline connecting the two antennas is fixed using normal RTK on-the-fly (OTF) techniques.

Despite these systems being subject to very harsh conditions (see next figure) such as vibration, shock, and even to corrosive materials, they are, however, expected to deliver the usual centimeter-level RTK accuracy, plus degree-level (or even sub-degree) accuracy for the heading/roll or heading/pitch estimated angles.



Figure 2.11: GNSS dual-antenna system located on the dozer's blade (Trimble GCS900 on a dozer with dual GPS – Trimble website).

As seen in the two previous figures, in these scenarios most of the multipath is originated from the platform itself. Typical metallic and flat smooth surfaces are seen all over these construction machines. Therefore it is quite reasonable to expect that the major source of carrier-phase error arise from multipath reflections.

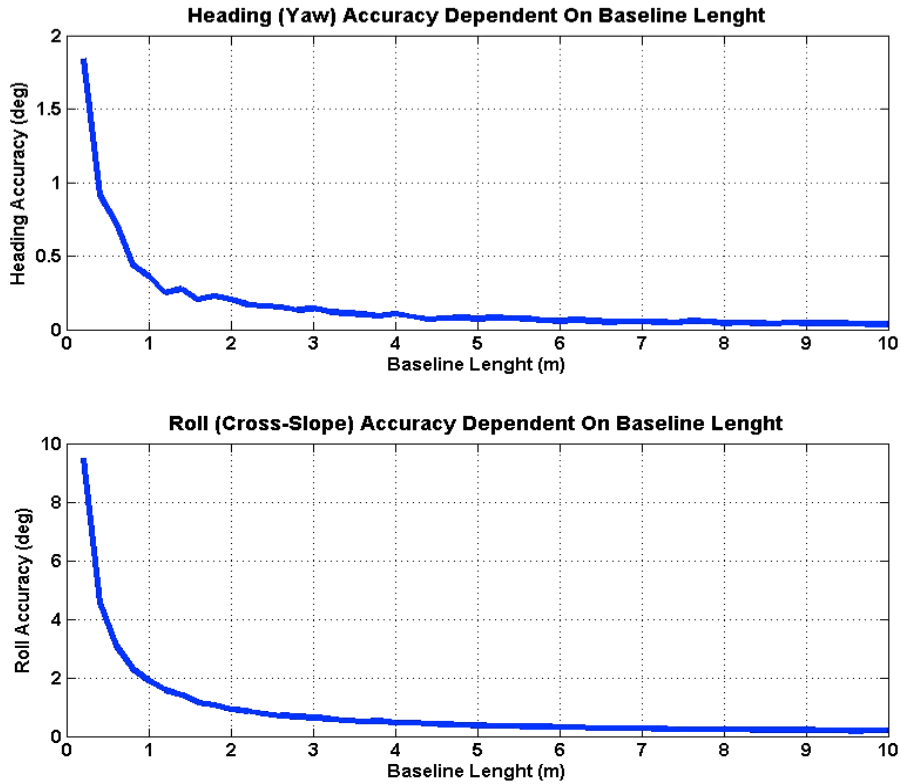


Figure 2.12: GNSS dual-antenna yaw and roll angles accuracies dependent on the baseline length (plots derived from a Matlab script using multiple antenna spacing between two GNSS-RTK receiver fixed solutions, and Equation 2.49)

Adding strong multipath signals to the high forces and pressure on the antennas, one can expect that not only the location and height (with pole masts) of the antennas should be

carefully chosen, but as well their distance (see Figure 2.12). In this dissertation, the algorithms developed within MIMICS technique, are supposed to deal with these kinds of scenarios.

3 Introduction to Carrier-Phase Multipath Error

3.1 Electro-Magnetic Waves (Plane Waves)

The theory behind GPS/GNSS multipath signals needs conceptual support as well as a sound geometric characterization. This is rather important as, though multipath represents the composition of multiple complex signals, still the best multipath mitigation techniques and algorithms assume certain geometric conditions and constraints along the signal propagation. That is certainly the case herein where the multipath models/observables to be derived depend upon electromagnetic plane-wave theory and propagation models (be it the direct incident path, or the multipath signals).

The wave equation is a second-order partial differential equation that is satisfied by all electromagnetic fields in homogeneous linear media [Popović and Popović, 2000]. Assume that an electromagnetic field exists in a homogeneous linear medium with parameters ϵ (complex dielectric constant), μ_0 (*vacuum* permeability), and σ (dielectric conductivity). Suppose that there are neither free charges nor field sources (impressed electric fields) in the medium considered then Maxwell's equations have the following form:

$$\nabla \times \mathbf{E} = -\mu_0 \frac{\partial \mathbf{H}}{\partial t}, \quad \nabla \cdot \mathbf{E} = 0 \quad (3.1)$$

$$\nabla \times \mathbf{H} = \sigma \mathbf{E} + \frac{\partial \mathbf{E}}{\partial t}, \quad \nabla \cdot \mathbf{H} = 0 \quad (3.2)$$

where \mathbf{E} and \mathbf{H} are, respectively, the electric and magnetic fields, and ∇ is the curl operator. What these equations say is that within electromagnetic plane waves (or any electromagnetic wave for that matter) is that their electric and magnetic field vectors are normal to each other, and to the direction of propagation, and constant in planes normal to that direction. If one rearranges these electromagnetic plane-wave equations assuming a harmonic time-dependence, then we obtain (where x, y, z are the plane propagation Cartesian coordinates):

$$\mathbf{E}(x, y, z, t) = \mathbf{E}(z)e^{j\omega t} \quad (3.3)$$

$$\mathbf{H}(x, y, z, t) = \mathbf{H}(z)e^{j\omega t} \quad (3.4)$$

Where $\mathbf{E}(z)$ and $\mathbf{H}(z)$ again represent the electric and magnetic fields, and are transverse with respect to the z -direction (i.e., the propagation direction of the wave) and ω is the angular-frequency of the wave. Although they represent the simplest electromagnetic waves, uniform plane waves are of extreme practical importance: actual waves radiating from sources are spherical, but at large distances from sources they become practically plane waves (as with the signal between GNSS satellites and user receivers). Wave fronts

are defined, in general, to be surfaces of constant phase. A forward moving wave like the following:

$$E(z) = e^{j\omega t} = E_0 e^{-jkz} \quad (3.5)$$

corresponds to the time-varying field:

$$E(z, t) = E_0 e^{j\omega t - jkz} = E_0 e^{j\varphi(z, t)} \quad (3.6)$$

where $\varphi(z, t) = kz - \omega t$, the wave number $k = 2\pi / \lambda$, and λ is the wavelength of the wave vector. A surface of constant phase (e.g., a plane wave) is obtained by setting $\varphi(z, t) = \text{const}$. Denoting this constant by $\varphi_0 = kz_0$ and using the property $\omega = kv$, we obtain the condition:

$$\varphi(z, t) = \varphi_0 \Rightarrow kz - \omega t = kz_0 \Rightarrow z = vt + z_0 \quad (3.7)$$

Thus the wave-front is the xy -plane intersecting the z -axis at the point $z = vt + z_0$, and moving forward with velocity v (conventionally c represents the speed of light - an electromagnetic wave - in a *vacuum*]. This justifies the so-called term “plane-wave”.

Analogously, a backward-moving wave will have planar wave-fronts parameterized by $z = -vt + z_0$, that is, moving backwards. A wave that is a linear combination of forward

and backward components may be thought of as having two planar wave-fronts, one moving forward, and the other backward.

The vectors $\{\mathbf{E}_{0+}, \mathbf{H}_{0+}, \hat{\mathbf{z}}\}$ and $\{\mathbf{E}_{0-}, \mathbf{H}_{0-}, -\hat{\mathbf{z}}\}$ form right-handed orthogonal systems and as such the magnetic field $\mathbf{H}_{0\pm}$ is perpendicular to the electric field $\mathbf{E}_{0\pm}$ (as depicted in Figure 3.1) and their cross-product, i.e. $\mathbf{E}_{0\pm} \times \mathbf{H}_{0\pm}$, points towards the direction of propagation, that is, $\pm \hat{\mathbf{z}}$. The next figure depicts the case of a forward propagating plane-wave:

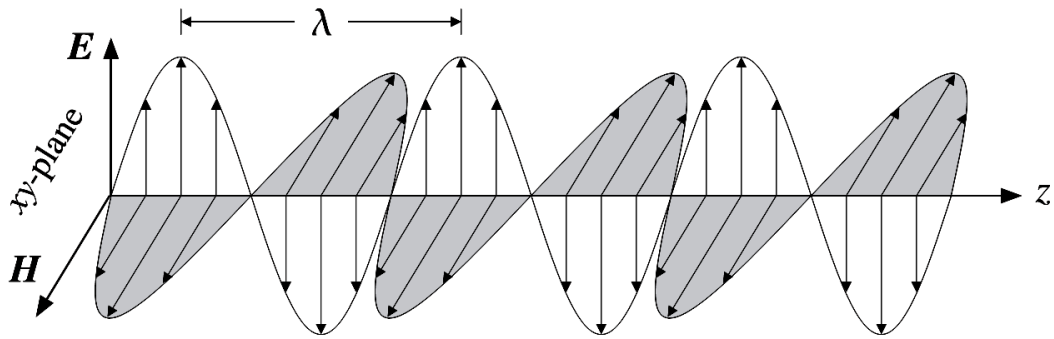


Figure 3.1: Forward uniform plane-wave (figure taken from [Popović and Popović, 2000])

The wavelength λ is the distance by which the phase of the sinusoidal wave changes by 2π radians. Since the propagation factor e^{-jkz} accumulates a phase of k radians per meter, we have by definition that $k\lambda = 2\pi$. The wave-length λ can be expressed via the frequency of the wave in Hertz, $f = \omega/2\pi$, as follows:

$$\lambda = \frac{2\pi}{k} = \frac{2\pi c}{\omega} = \frac{v}{f} \quad (3.8)$$

3.2 Polarization

The polarization of a plane-wave is defined to be the direction of the electric field. More precisely, polarization is the direction of the time-varying real-valued field, that is:

$$\mathbf{E}(z,t) = \text{Re}[\mathbf{E}(z,t)] \quad (3.9)$$

At any fixed point Z the vector $\mathbf{E}(z,t)$ may run along a fixed linear direction or it may be rotating as a function of t , tracing a circle or an ellipse. Let's imagine that one curls his fingers of his left and right hands into a fist and point both thumbs towards the direction of propagation. If the fingers of his right hand are curling in the direction of rotation of the electric field, then the polarization is right polarized.

Thus in this example because we have a forward-moving field and the field is turning counter-clockwise, the polarization will be right-circular just like with GPS, GLONASS and Galileo signals. In fact, all GNSS signals are circular polarized and for consistency they follow a right-hand circular polarization (RHCP) scheme. If the field were moving backwards, then it would be left-circular. We can see in next figure (Figure 3.2) the four cases of left/right polarization with forward/backward plane-waves:

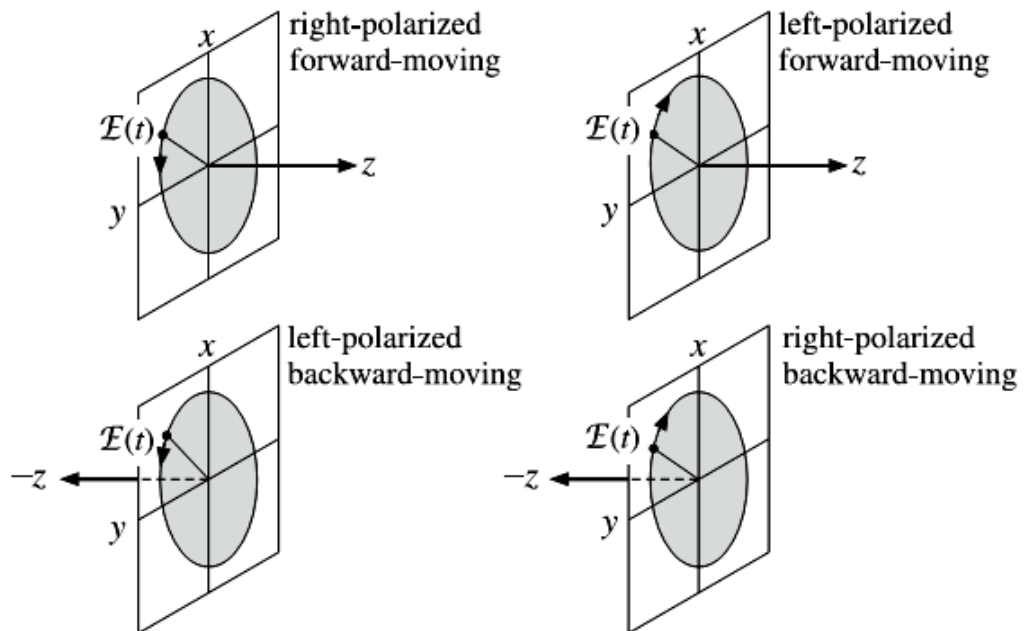


Figure 3.2: Left, right circular polarizations (figure taken from [Popović and Popović, 2000])

3.3 Multipath Spectra

Multipath is the unwanted distortion of the direct Line-Of-Sight (LOS) satellite signal by localized reflected and/or diffracted signals, thus distortions caused by indirect secondary satellite signals arriving at the receiver. The extent and severity of multipath experienced by a GNSS receiver, at the antenna and RF front-end, depends mainly on the type of environment where it is located (comparing for instances an urban-canyon with an open space scenario), the number and type reflector material, the relative height and distance

between the receiver antenna(s) and the reflector(s), the receiver dynamics and the satellite position during its orbit.

An example providing the different faces of multipath reflections and thus providing a feeling of the multipath spectra is given next figure (Figure 3.3):

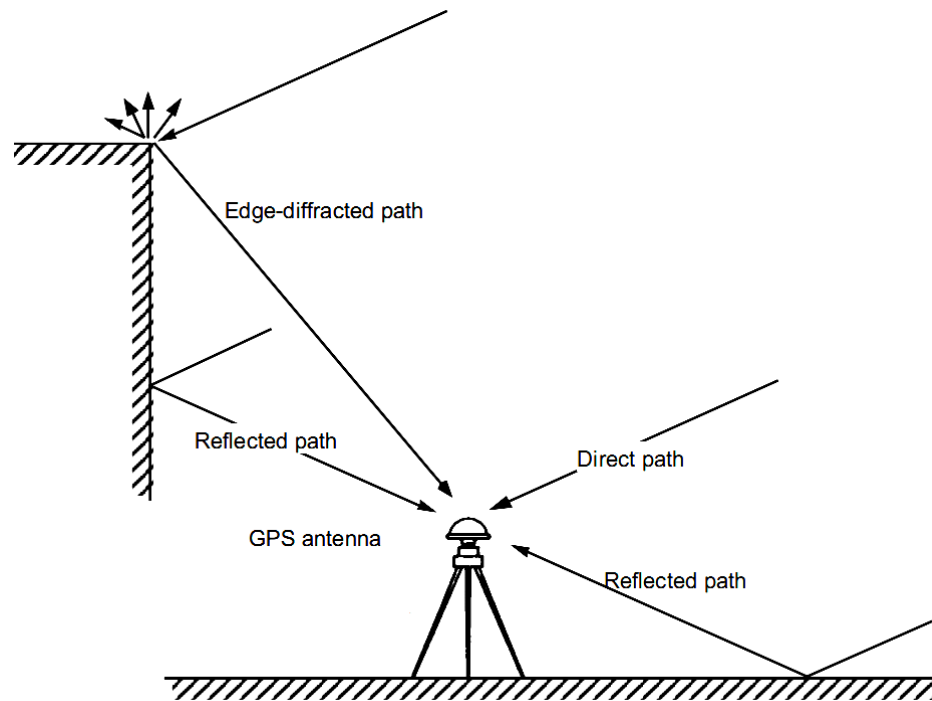


Figure 3.3: A typical multipath-rich environment

The reflection and scattering of the signal from a surface has two components: the specular and the diffuse components [Ray, 2000]. Reflection off of smooth surfaces such as mirrors, concrete walls or a calm body of water leads to a type of reflection known as

specular reflection. Reflection off of rough surfaces such as clothing, paper, and the asphalt roadway leads to a type of reflection known as diffuse reflection.

Whether the surface is microscopically rough or smooth has a tremendous impact upon the subsequent reflection of a beam of light. The diagram below depicts two beams of light incident upon a rough and a smooth surface.

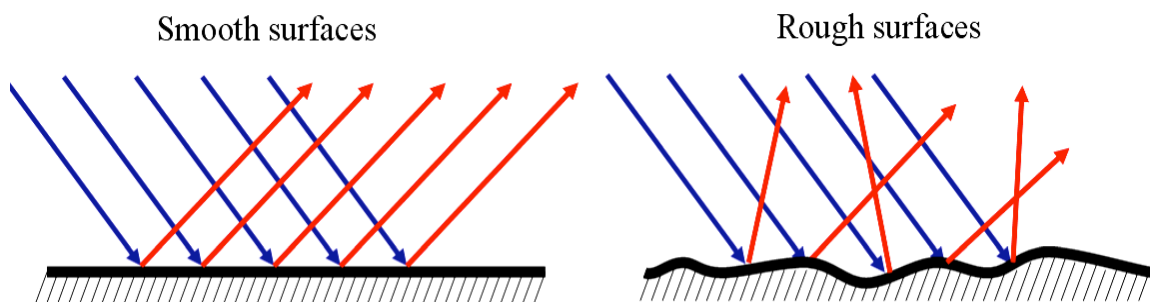


Figure 3.4: Specular reflection (left), and diffuse reflection (right)

Specular reflections are deterministic in nature and originate from smooth surfaces (Figure 3.4 - left), as opposed to diffuse scattering which tends to be random and therefore can be included in the stochastic modeling (noise) of any electromagnetic-ranging system (Figure 3.4 - right).

Thus, specular reflections, due to their biasness, require more complex modeling and will then be given special attention in the following ray-tracing models, and throughout this dissertation.

When a reflected electromagnetic wave from a specular reflector occurs then it is the result of the radiation of the points on the *Fresnel* ellipse (Figure 3.5). The resultant wave has very little fluctuation of phase and amplitude and therefore is very deterministic as mentioned before.

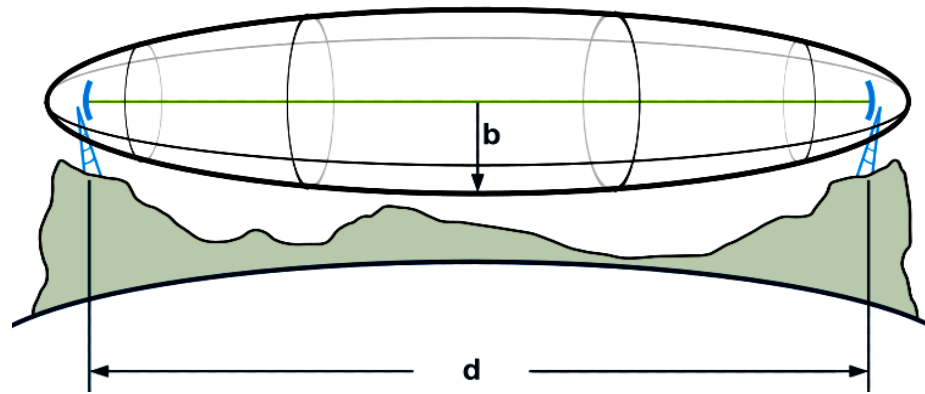


Figure 3.5: Fresnel zone (where d is the distance between the transmitter and receiver, b is the radius of the Fresnel zone)

A Fresnel zone is one of a (theoretically infinite) number of concentric ellipsoids which define volumes in the radiation pattern of a (usually) circular aperture. Fresnel zones result from diffraction by the circular aperture and basically provide a very powerful tool to acknowledge, dependent on which zone (thus the aperture radius), by how much the signal phase changes due to the obstructions/reflections.

Before considering reflection coefficients for specific GNSS multipath propagation cases we first need to develop an understanding of propagation situations that describe the

majority of GNSS multipath propagation scenarios. These are, for the time-being, very simplistic 2-D ray-tracing multipath scenarios and just for one receiver antenna being affected by a deterministic multipath bias, therefore a specular reflector.

Consider the forward-scatter problem with a flat specular reflecting lower boundary in Figure 3.6 where the GNSS antenna is located at point P , at a distance d from the left-hand boundary, height h above the reflecting surface, and with a LOS signal propagating into the domain at angle θ .

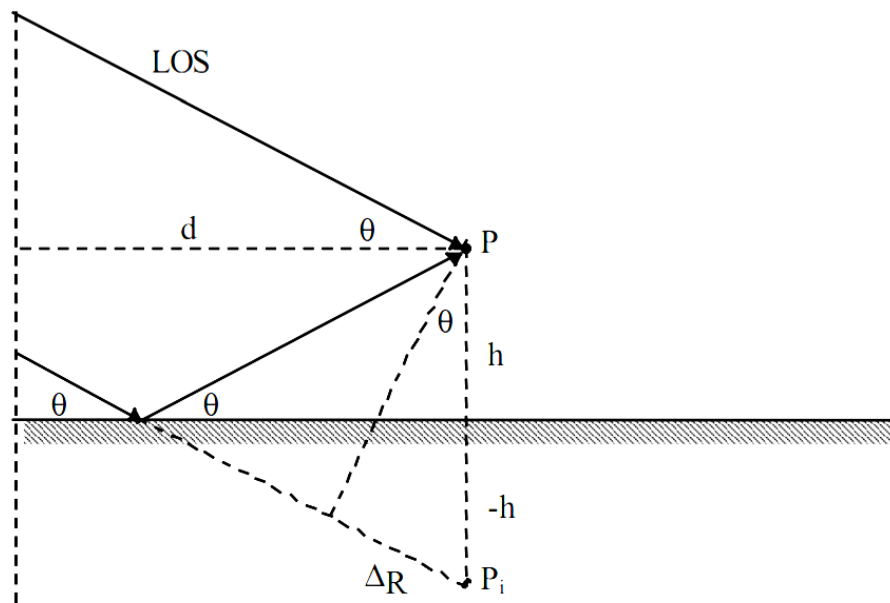


Figure 3.6: A 2-D ray-tracing model of forward scatter geometry

In terms of receiver-tracking the main problem is that any additional secondary path will have a time-delay making the reflected signal travel an additional distance ΔR to the

image point P_i (always in relation to the LOS point P). This additional path-length using basic trigonometric manipulation is given by:

$$\Delta R = 2h \sin \theta \quad (3.9)$$

Now let's consider the backscatter problem with the addition of a vertical reflecting surface forming the right-side boundary (Figure 3.7):

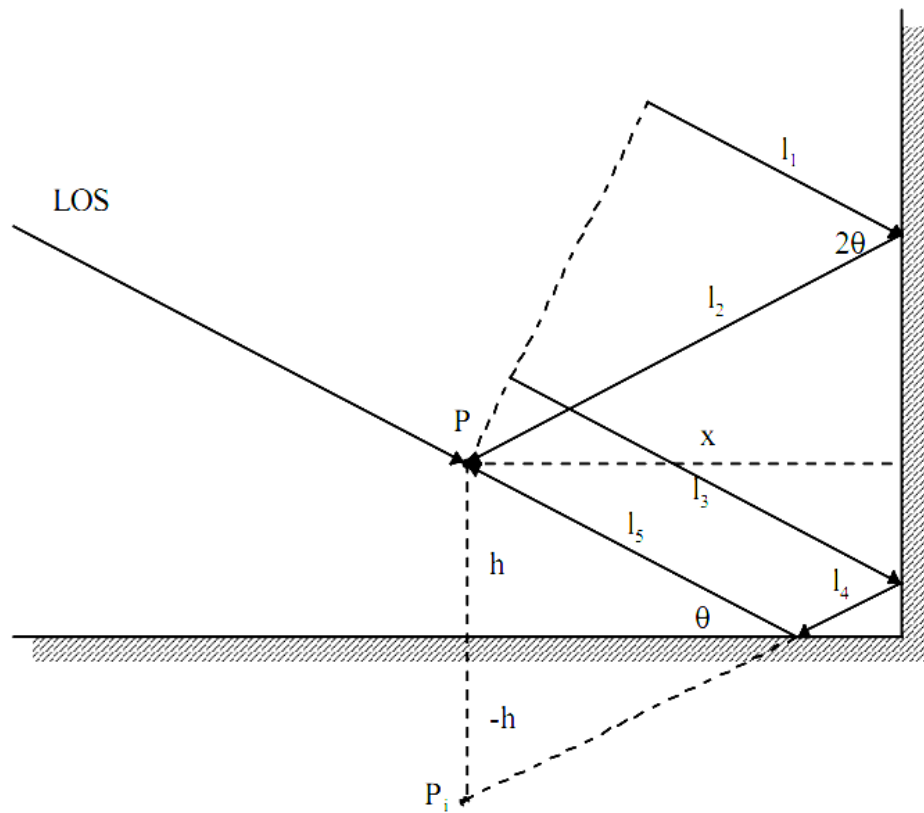


Figure 3.7 A 2-D ray-tracing model of backscatter geometry (I)

In this scenario one has to distinguish all the possible additional path lengths, represented by l_i with $i=1...5$. Nevertheless and for this particular geometry x , representing the distance from the centre LOS point P to the right hand-side boundary, respects the following inequality (basically it says that both second and third signals arrive above the LOS signal):

$$x > \frac{h}{\tan \theta} \quad (3.10)$$

The region in which this occurs will be known as zone l_i . The individual path lengths are then given by the following five equations (Equation 3.11):

$$\begin{aligned} l_1 &= \frac{x \cos 2\theta}{\cos \theta} \\ l_2 &= \frac{x}{\cos \theta} \\ l_3 &= 2h \sin \theta + \frac{x \cos 2\theta}{\cos \theta} \\ l_4 &= \frac{x}{\cos \theta} - \frac{h}{\sin \theta} \\ l_5 &= \frac{h}{\sin \theta} \end{aligned} \quad (3.11)$$

And the total path-length difference, relative to the LOS, is given by the two combinations:

$$\Delta R_A = l_1 + l_2 = 2x \cos \theta \quad (3.12)$$

and

$$\Delta R_B = l_3 + l_4 + l_5 = 2h \sin \theta + 2x \cos \theta \quad (3.13)$$

which adding algebraically gives the following result (total path difference):

$$\Delta R_A + \Delta R_B = \frac{2x}{\cos \theta} = \frac{2h}{\sin \theta} \quad (3.14)$$

For the sake of completeness, one should include the case, and using the previous scenario depicted in Figure 3.5, when the reflected signal arriving from below the horizontal produces a different geometric arrangement depicted in next figure (Figure 3.8):

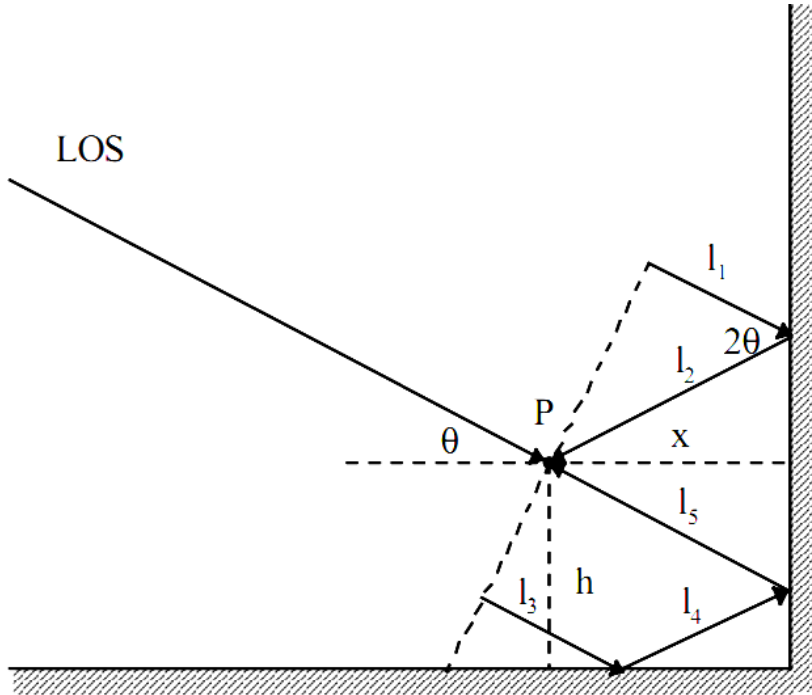


Figure 3.8: A 2-D ray-tracing model of backscatter geometry (II)

As before the relevant paths are given by:

$$\begin{aligned}
 l_1 &= \frac{x \cos 2\theta}{\cos \theta} \\
 l_2 = l_5 &= \frac{x}{\cos \theta} \\
 l_3 &= 2x \cos \theta - \frac{h \cos 2\theta}{\sin \theta} \\
 l_4 &= \frac{h}{\sin \theta} - \frac{x}{\cos \theta}
 \end{aligned}
 \tag{3.15}$$

However, the total path differences are the same as those given by Equation 3.7 [Hannah, 2001]. Unfortunately, these ray-tracing geometric models only hold for optimal situations

where the satellite during its visible orbit is perfectly aligned with the reflector and thus the LOS satellite signal plus all the secondary (multipath) signals are all contained in a plane perpendicular to the specular reflector surface (see Figures 3.6, 3.7, and 3.8).

Nevertheless in our studies we are mostly concerned with the accurate understanding and development of specular multipath ray-tracing models that should fit all satellite orbit scenarios and specifically for close-by dual-antenna systems (which can have different heights between them further complicating the ray-tracing modeling). Such a scenario can be seen in Figure 3.9:

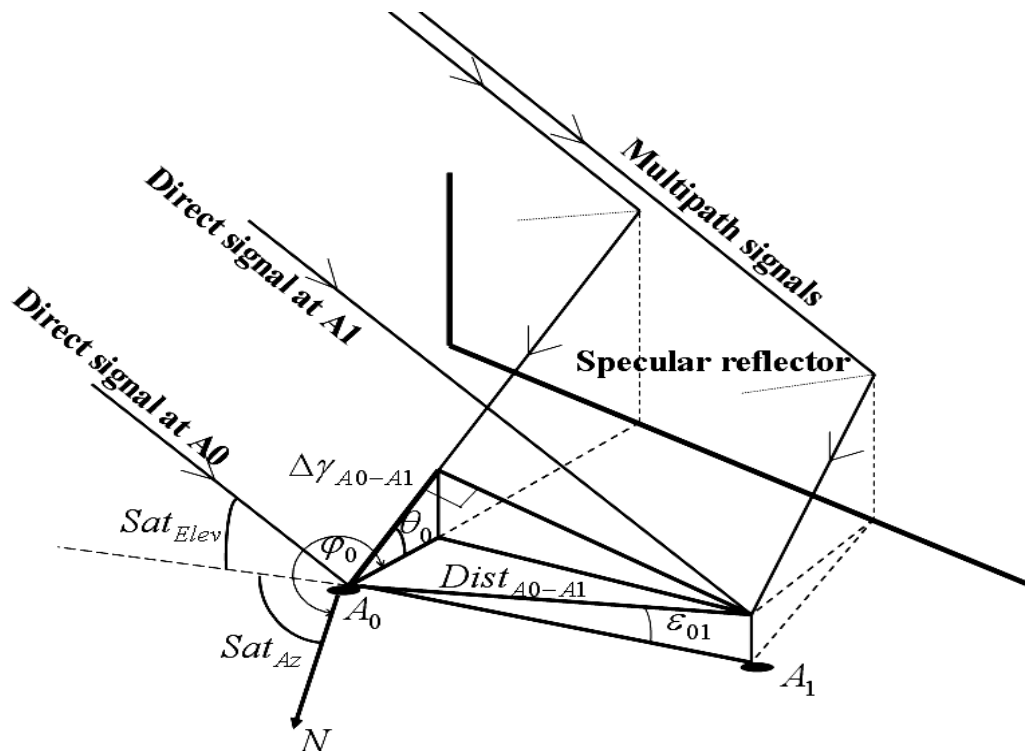


Figure 3.9: A 3-D ray-tracing phase multipath model in a dual-antenna system (master antenna A_0 , and slave antenna A_1)

Where $\Delta\gamma_{A_0-A_1} = \Delta\gamma_{A_0} - \Delta\gamma_{A_1} = \Delta\gamma_{01}$ is the difference between the multipath phase-delay at antenna 0 and antenna 1, φ_0 and θ_0 are the azimuth and elevation-angle between the master antenna A_0 and the specular reflector respectively, and ε_{01} is the differential height between the two antennas (in radians).

Missing in the figure is the angle ϕ_{01} representing the differential azimuth between the two antennas. In fact, these parameters $(\Delta\gamma_0, \varphi_0, \theta_0)$ represent the bulk of the spectral single-difference (between-antennas) multipath geometric parameterization (missing is a dampening factor that will be overviewed later).

Because the goal is to parameterize a dual-antenna multipath observable we ought to relate the multipath phase-delay parameter from one antenna to the other (mathematically speaking it is also advisable to reduce the state vector unknown number). Ray [2000] has shown that the following equation relates the multipath phase delay at two close-by antennas, for a static scenario (please see this dissertation for further explanation on how to obtain the equation):

$$\Delta\gamma_1 = \Delta\gamma_0 - \frac{2\pi}{\lambda_{L_i}} dist_{01} \cos(\varphi_0 - \phi_{01}) \cos(\theta_0) \quad (3.16)$$

However this model assumes that contiguous antennas are positioned on the same fixed plane, thus with the same orthometric height, which is exactly the proposed method for

static carrier-phase multipath mitigation (see Figure 3.10, and note in particular the plate with 6 patch antennas).

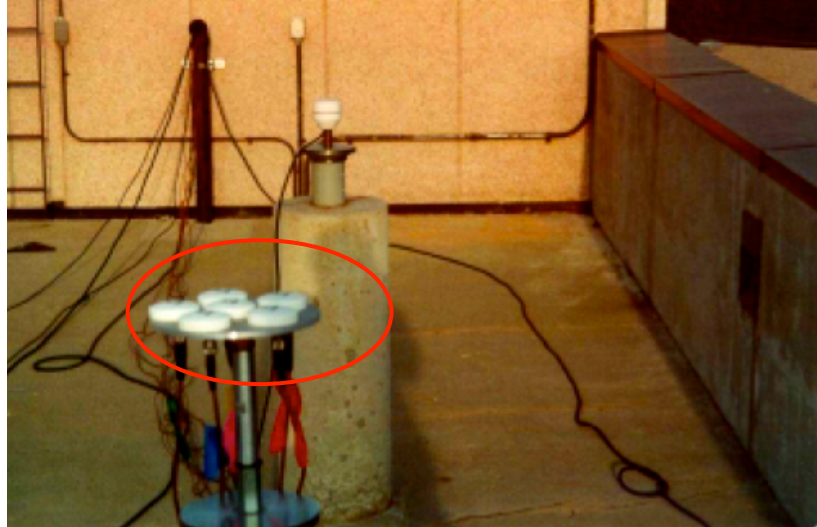


Figure 3.10: Setup scenario for static carrier-phase multipath mitigation tests done by Ray [2000]

However, realistically speaking in any GNSS RTK-based heading or attitude system employing multi-antenna systems the dynamic platform is prone to experience several differential angular motions between the antennas. These motions, depending on the alignment of the antennas on the platform, are the platform attitude angles which can vary considerably, even for a short time span, as it is typical in an airplane GNSS-based heading system (Figure 3.11):

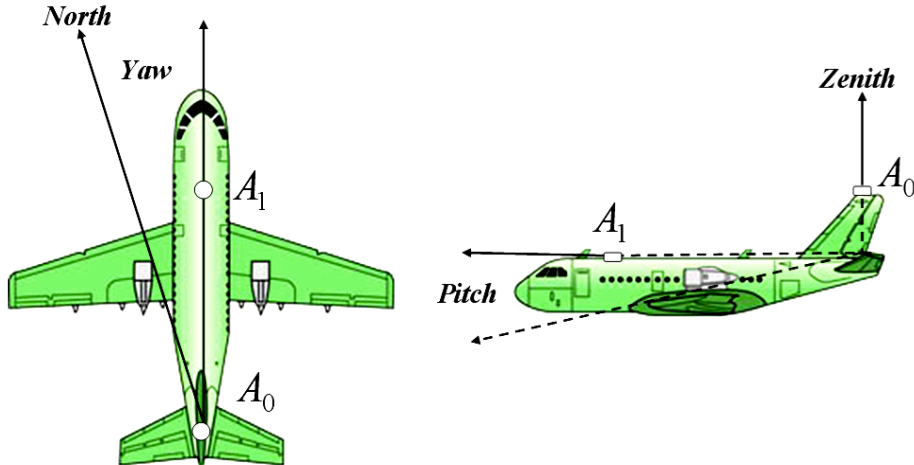


Figure 3.11: Example of a GNSS-based heading (and pitch) reference system

Therefore Equation 14 has to be slightly adapted to those situations where there is constantly changing the differential elevation angle, $\varepsilon_{01} = \varepsilon_0 - \varepsilon_1$, between contiguous antennas:

$$\Delta\gamma_1 = \Delta\gamma_0 - \left[\frac{2\pi}{\lambda_{L_i}} dist_{01} \cos(\phi_0 - \phi_{01}) \cos(\theta_0) \cos(\varepsilon_{01}) \right] \quad (3.17)$$

Note that when that angle ε_{01} is zero, thus the antennas are on the same horizontal plane, the two previous equations do provide the same result.

3.4 Reflection coefficient

Plane electromagnetic waves frequently encounter obstacles along their propagation paths. In such cases, the wave induces induction currents in the object (if the object is metallic), or polarization currents (if the object is made of an insulator). This induced current is the origin of the scattered field, and is in the root of the electromagnetic multipath signals. The reflectors are called *scatterers* or multipath reflectors.

When a plane electromagnetic wave is incident on a planar boundary between two homogeneous media, the scattered waves are also plane waves [Popović and Popović, 2000]. One of these waves is radiated back into the space of the incident wave, hence it is known as the reflected wave.

The behavior of multipath is determined by the geometry (as depicted in the previous specular-reflector-based ray-tracing models), and electrical properties of the propagation environment. Signals reflected from a sufficiently smooth surface are called *specularly* reflected signals. They are directional, phase coherent and contributed by the central Fresnel zones (Figure 3.5) on the surface near the receiver. The total field received by the antenna is the sum of direct signal and *specularly* reflected signal.

The reflection coefficients, derived from the Fresnel equations (Equations 3.18, and 3.19) for a smooth flat surface, provide information on the nature of the reflected signals [Hannah, 2000]. GNSS signals are RHCP, and since circular polarization is the vector sum of the horizontal and vertical polarized waves then one can derive the reflection coefficients for the horizontal and vertical components, respectively:

$$\Gamma_H = \frac{\sin \theta - \sqrt{\varepsilon - \cos^2 \theta}}{\sin \theta + \sqrt{\varepsilon - \cos^2 \theta}} \quad (3.18)$$

$$\Gamma_V = \frac{\varepsilon \sin \theta - \sqrt{\varepsilon - \cos^2 \theta}}{\varepsilon \sin \theta + \sqrt{\varepsilon - \cos^2 \theta}} \quad (3.19)$$

where

$$\varepsilon = \varepsilon_r - j \frac{\sigma}{\omega \varepsilon_0} \quad (3.20)$$

is the complex absolute permittivity (frequency-dependent). Substituting for ω and ε_0 in Equation 3.20 gives:

$$\varepsilon = \varepsilon_r - j60\lambda\sigma \quad (3.21)$$

where ε_0 is the *vacuum* permittivity (also called permittivity of free space or the electric constant), and represents the ratio of the magnetic, and electric field in free-space. Its value, by definition, is given by:

$$\varepsilon_0 = \frac{1}{c^2 \mu_0} \approx 8.8541878176... \times 10^{-12} \frac{F}{m} \text{ (Farads per meter),}$$

and μ_0 is the *vacuum* permeability with a value of $4\pi \times 10^{-7} V \cdot s / A \cdot m$ (the S.I. units represent Volts times seconds divided by Amperes time metres). ϵ_r is the relative permittivity (or dielectric constant) of the reflecting surface material (unit-less), and σ represents the dielectric conductivity (with units S/m, that is, Siemens per meter). The relationship between the different permittivity quantities is given by:

$$\epsilon_r(\omega) = \frac{\epsilon(\omega)}{\epsilon_0} \quad (3.22)$$

The dielectric constant ϵ_r and conductivity σ depend not only on the frequency of the electromagnetic wave but also on the nature of the surface, the temperature, and the moisture content (i.e., when reflected from the soil surface).

The calculation of each linear reflection coefficient is now straightforward, for a given frequency, grazing angle (θ -the angle between the electromagnetic beam and the surface, rather than that between the beam and the surface normal, in other words 90° minus the angle of incidence), dielectric constant and conduction value for the reflecting surface medium [Hannah, 2001].

A plot depicting several reflection coefficient values, for a concrete-made specular reflector is given in Figure 3.12 (other materials could be chosen, but concrete is chosen for the sake of consistency with the real-live signal tests made where the main blockage/reflector was made of this material). The plot represents an effective coupled (

Γ_H and Γ_V) reflection coefficient magnitude for an incident L_1 GPS RHCP signal, and for typical antenna attenuation ratios (to reduce receiver sensitivity to unwanted multipath signals) ranging from 0 dB to 30 dB.

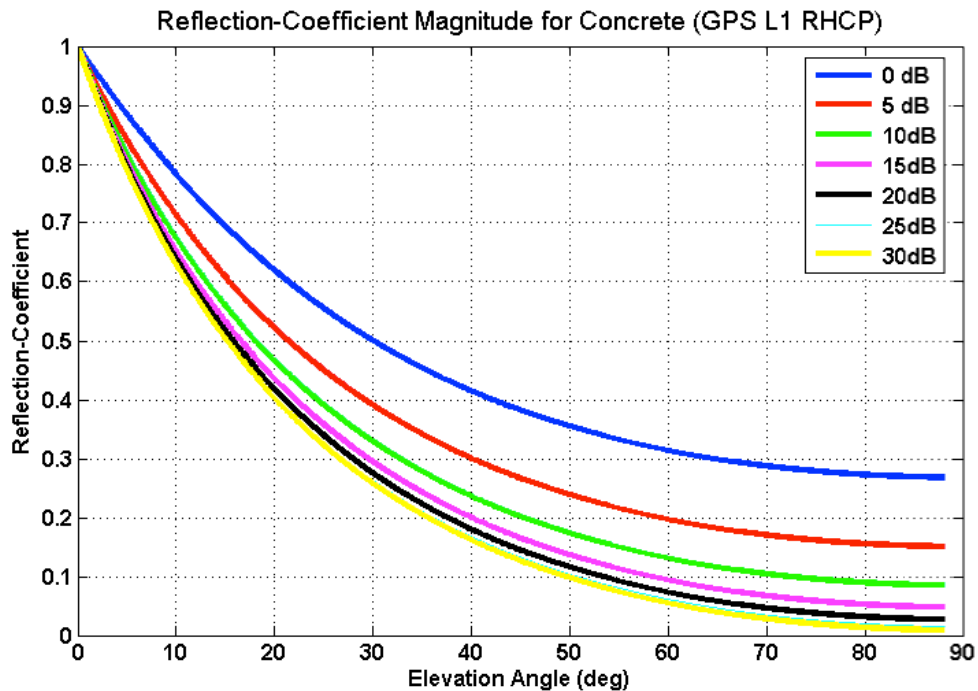


Figure 3.12: Coupled reflection coefficient values for concrete, using several antenna attenuation values, and a 0 to 90 degrees incidence angle function [Hannah, 2001].

Therefore, the reflection coefficient for a smooth surface is a function of the relative dielectric constant, the conductivity, the elevation angle, and the electromagnetic wave frequency. The reflection coefficient of the reflecting surface also depends on the polarization of the incident field. If the electric field intensity vector is in the plane of incidence, the polarization is vertical and the reflection coefficient Γ_V , applies, while Γ_H

applies when the wave is polarized perpendicular to the plane of incidence. The Brewster angle θ_B is the angle at which Γ_V goes to zero:

$$\theta_B = a \tan\left(\sqrt{\varepsilon_1/\varepsilon_2}\right) \quad (3.23)$$

Where the indexes 1, and 2 represent the medium of the incoming signal, and of the absorbed or scattered medium, respectively. If medium 1 is air then:

$$\varepsilon_1 = 1 \Rightarrow \theta_B = a \tan\left(\sqrt{1/\varepsilon_2}\right) \quad (3.24)$$

As mentioned before GNSS signals are circularly polarized, where the most basic motivation is that circular polarizations are more tolerant of physical orientation mismatches, that is, between the GNSS satellite emitter (which may spin), and the receiver antenna.

.Reflection coefficients for circularly polarized waves can be derived from those for horizontal and vertical polarization..If the elevation angle is less than the Brewster angle, the circular polarization component predominates, whereas if the angle is greater than the Brewster angle then the orthogonal polarization component predominates.

3.5 Carrier-phase multipath at the receiver carrier-tracking loop

After developing a specular multipath ray-tracing model for a dual-antenna system optimized for kinematic scenarios, and a simple concrete-made reflection coefficient (thus all the state-vector parameters to be included in a multipath observable) one should relate them, and provide a canonical meaning, with the way how they are sensed from the receiver point-of-view, that is, how carrier-phase multipath is formed at the carrier tracking-loop.

The GNSS signal processing takes place in different channels. Every satellite visible to the antenna is allocated to its own channel, limited by a maximum number of channels in the receiver. Figure 3.13 is an overview of a channel:

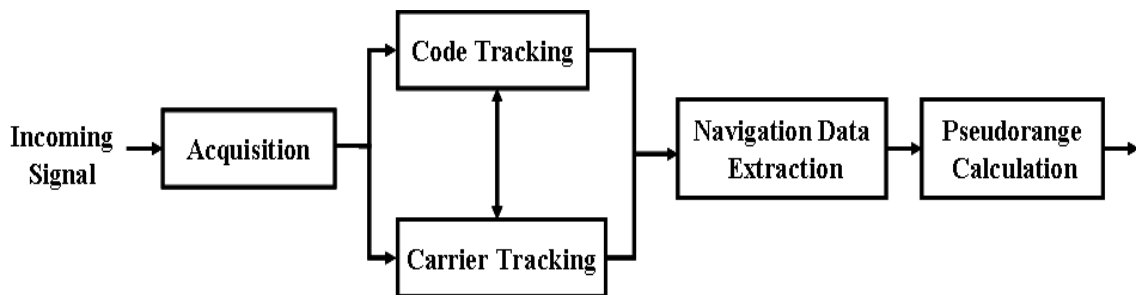


Figure 3.13: Schematic overview of how a GNSS receiver channel works

The *acquisition stage* depicted in Figure 3.13 has a purpose of identifying if a certain satellite is visible to the user or not. If the satellite is visible, the acquisition must determine the signal frequency (which is different from its nominal frequency, due to the satellite relative motion causing a Doppler effect - thus a frequency shift), and the signal

code-phase (the point in the current incoming signal data-block where the C/A code begins).

When acquiring a satellite k , the incoming signal s is multiplied with the locally generated C/A code corresponding to the satellite k (being GNSS one-way ranging systems, this is the only way that a receiver can identify correctly a satellite k). The C/A code is a 1,023 bit long pseudorandom number (PRN) which, when transmitted at 1.023 megabits per second (Mbit/s), repeats every millisecond. Pseudorandom numbers only match up, or strongly correlate, when they are exactly aligned.

Each satellite transmits a unique PRN code, which does not correlate well with any other satellite's PRN code. In other words, the PRN codes are highly orthogonal to one another (at this 2nd stage, the codes are clearly distinguishable from each other). This is a form of code division multiple access (CDMA), which allows the receiver to recognize multiple satellites on the same frequency. The cross-correlation done within the receiver between C/A codes for different satellites can only be done successfully if the locally generated C/A code (replica) is properly aligned in time, i.e., with the correct code-phase.

Similarly, to remove the carrier-wave from the signal, the frequency of the locally generated signal must be close to the incoming signal-frequency. For static platforms/receivers this is a rather simple task. However, when the host platform experiences high-dynamics resulting in faster and bigger Doppler changes (e.g., in planes

and rockets), the receiver local frequency replica might have a problem coping with the incoming signal frequency.

The *tracking stage* is a process that improves the coarse values of code-phase and frequency, and keeps track of these as the signal properties change over time. The accuracy of the final value of the code-phase is connected to the accuracy of the pseudo-range calculated later on. The tracking contains two parts, code-tracking and carrier-frequency/phase tracking.

Because this dissertation deals mainly with carrier-phase multipath, only the carrier-wave tracking is overviewed. This tracking is done in two ways, either by tracking the phase of the signal or by tracking the frequency. The tracking is running continuously to follow the changes in frequency as a function of time (Doppler shift due to relative satellite-receiver motion). To track a carrier wave signal phase-lock loops (PLL), or frequency-lock loops (FLL) are often used:

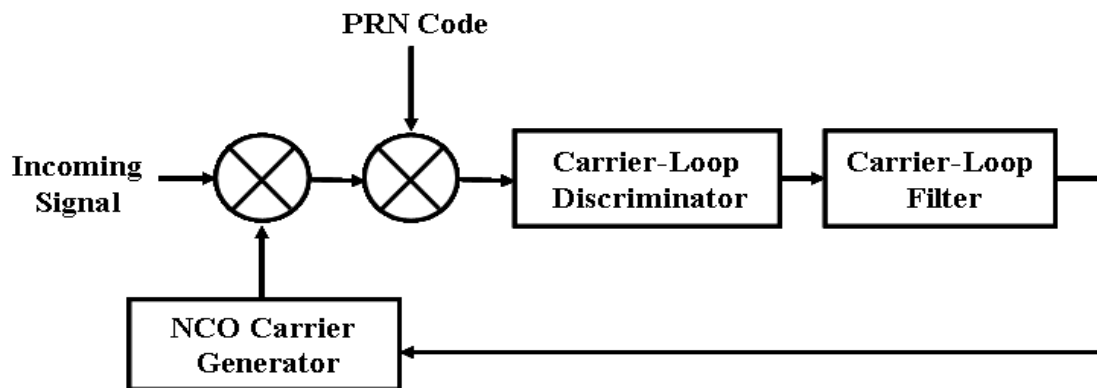


Figure 3.14: Schematics of a PLL (phase-lock loop) for carrier-tracking

Figure 3.14 shows a basic block diagram for a phase-lock loop. The first two multiplications remove the carrier, and the PRN code of the input signal through signal-mixing (thus the \otimes operator), and by doing it the signal is moved from a center-frequency (RF) to an intermediate-frequency (IF).

The loop discriminator block is used to find the phase-error on the local (receiver-generated) carrier wave replica. The output of the discriminator, d , which is the phase-error (or a function of the phase-error), is then filtered and used as a feedback to the numerically controlled oscillator (NCO) which adjusts the frequency of the local carrier-wave. In this way the local carrier-wave could be an “almost” precise replica of the input signal carrier-wave.

The problem with using an ordinary PLL is that it is sensitive to 180° degrees phase-shifts. Due to navigation bit transitions, a PLL used in a GPS receiver has to be insensitive to 180° degrees phase-shifts.

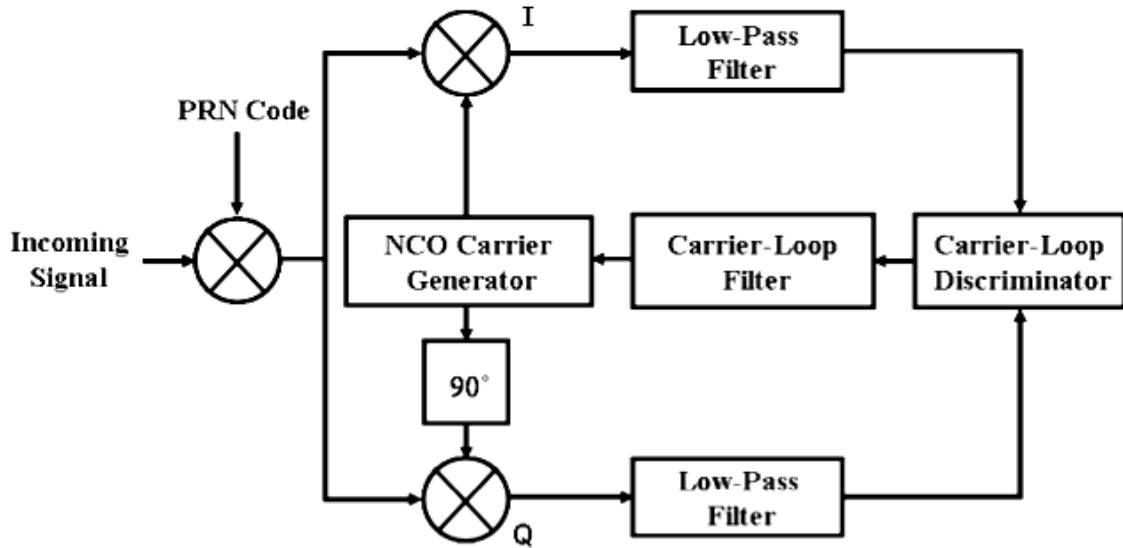


Figure 3.15: *Costas*-loop schematic, which is a 180° degrees phase-shift insensitive PLL

Figure 3.15 shows a *Costas*-loop. One property of this loop is that it is insensitive for 180° phase-shifts and hereby a *Costas*-loop is insensitive for phase transitions due to navigation bits. This is the reason for using this carrier-tracking loop in all GPS receivers.

The *Costas*-loop in Figure 3.15 contains two multiplications: The first multiplication is the product between the input signal and the local carrier-wave, and the second multiplication is between a 90° degree phase-shifted carrier-wave and the input signal (quadrature-arm Q).

The goal of the *Costas* loop is to try and keep all energy in the I (in-phase) arm. To keep the energy in the I arm some kind of feed-back to the oscillator is needed. If it is

assumed that the code-replica in Figure 3.15 is perfectly aligned, the multiplication in the I arm gives the following:

$$AC^k(\tau)\cos(\omega_{IF}t)\cos(\omega_{IF}t + \varphi) = \frac{A}{2}C^k(\tau)\cos(\varphi) + \frac{A}{2}C^k(\tau)\cos(2\omega_{IF}t + \varphi) \quad (3.25)$$

where φ is the phase-error between the local replica of the carrier-phase and the phase of the incoming signal, i.e., $\varphi = \phi_{rep} - \phi_{in}$, A is the amplitude, C^k is the auto-correlation function for satellite k , τ is the correlation time function, and ω_{IF} is the intermediate-frequency obtained through down-conversion. The multiplication in the quadrature-arm gives the following:

$$AC^k(\tau)\cos(\omega_{IF}t)\sin(\omega_{IF}t + \varphi) = \frac{A}{2}C^k(\tau)\sin(\varphi) + \frac{A}{2}C^k(\tau)\sin(2\omega_{IF}t + \varphi) \quad (3.26)$$

If the two signals (In-phase and Quadrature) are low-pass filtered after the multiplication as seen in Figure 3.15, the two terms with the double intermediate frequency are eliminated and the following two signals are achieved:

$$I^k = \frac{A}{2}C^k(\tau)\cos(\varphi) \quad (3.27)$$

$$Q^k = \frac{A}{2}C^k(\tau)\sin(\varphi) \quad (3.28)$$

To find a term to feed-back to the carrier-phase oscillator, it can be seen that the phase-error of the local carrier-phase replica can be found in this way:

$$\frac{Q^k}{I^k} = \frac{\frac{A}{2} C^k(\tau) \sin(\varphi)}{\frac{A}{2} C^k(\tau) \cos(\varphi)} \Leftrightarrow \frac{Q^k}{I^k} = \tan(\varphi) \quad (3.29)$$

From which we obtain:

$$\varphi = \tan^{-1}\left(\frac{Q^k}{I^k}\right) \quad (3.30)$$

Again, φ is the phase-error between input and local generated replica of the carrier-phase observable, and assuming that it does not contain any multipath. From Equation 3.25, it can be seen that the phase-error is minimized when the correlation in the quadrature-phase arm is zero and the correlation value in the in-phase arm is maximum.

The arc-tangent discriminator in Equation 3.30 is the most precise one amongst the *Costas* discriminators, but it is also the most time consuming discriminator. Table 3.1 describes other possible *Costas* discriminators.

| Discriminator | Description |
|---|---|
| $d = \sin(I^k) \cdot Q^k$ | Least computational load, the output of the discrimination is proportional to $\sin(\varphi)$ |
| $d = I^k \cdot Q^k$ | Moderate computational load, the discriminator output is proportional to $\sin(2\varphi)$ |
| $d = \tan^{-1}\left(\frac{Q^k}{I^k}\right)$ | High computational load, the discriminator output is the phase error. |

Table 3.1: Various types of Costas phase-lock loop discriminators (d)

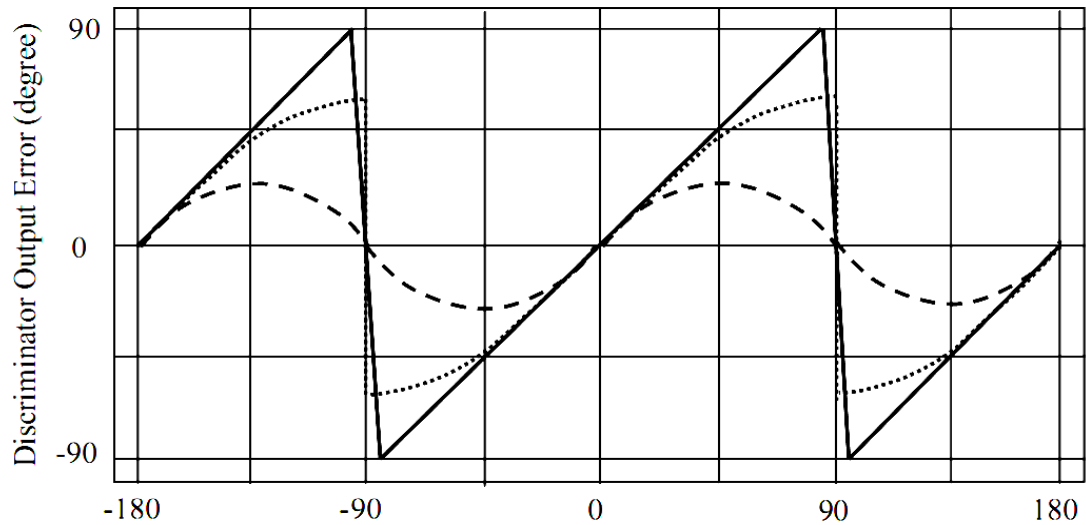


Figure 3.16: Discriminator input error (degrees), and:

$$\begin{array}{l} \sin(I^k) \cdot Q^K \text{} \\ I^K \cdot Q^k \text{ -----} \\ \tan^{-1}\left(\frac{Q^k}{I^k}\right) \text{ -----} \end{array}$$

If navigation bit transition occurs, the *Costas*-loop will still track the signal and nothing will happen. This property assures the *Costas*-loop is the commonly chosen phase-lock loop in receivers [Kaplan, 1996]. In Equation 3.30, the phase-error is also the discriminated value:

$$d = \varphi = \tan^{-1}\left(\frac{Q^k}{I^k}\right)$$

and the discriminator behavior can be seen in Figure 3.16 (solid continuous line). The output of the phase discriminator is filtered to predict and estimate any relative motion of the satellite (and the receiver if it is in kinematic mode), and to estimate the *Doppler* shift frequency. Using again Equation 3.29, but now assuming that the incoming direct signal is contaminated by several multipath reflections we then obtain the following equation:

$$\frac{Q^k}{I^k} = \frac{\frac{A}{2} C^k(\tau) \sin(\varphi) + \frac{A}{2} \sum_{j=0}^n \alpha_j C^k(\tau + \Delta\tau_j) \sin(\varphi + \Delta\gamma_j)}{\frac{A}{2} C^k(\tau) \cos(\varphi) + \frac{A}{2} \sum_{j=0}^n \alpha_j C^k(\tau + \Delta\tau_j) \cos(\varphi + \Delta\gamma_j)} = \tan(\tilde{\varphi}) \quad (3.31)$$

where α_j , $\Delta\tau_j$, and $\Delta\gamma_j$ are respectively the reflection coefficient, the multipath signal time-delay, and multipath path phase-delay from reflector j . The value $\tilde{\varphi}$ represents the incoming-to-replica phase difference error now contaminated by multipath. The previous equation can be simplified to (removing the common amplitude terms):

$$\frac{Q^k}{I^k} = \frac{C^k(\tau)\sin(\varphi) + \sum_{j=0}^n \alpha_j C^k(\tau + \Delta\tau_j)\sin(\varphi + \Delta\gamma_j)}{C^k(\tau)\cos(\varphi) + \sum_{j=0}^n \alpha_j C^k(\tau + \Delta\tau_j)\cos(\varphi + \Delta\gamma_j)} \quad (3.32)$$

We have been developing models dealing with strong multipath specular reflectors. Therefore it is reasonable to consider that the carrier-phase multipath signature, for a certain correlation period, is given by the composition (addition) of all secondary incoming signals, thus:

$$\frac{Q^k}{I^k} = \frac{C^k(\tau)\sin(\varphi) + \alpha_M C^k(\tau + \Delta\tau_M)\sin(\varphi + \Delta\gamma_M)}{C^k(\tau)\cos(\varphi) + \alpha_M C^k(\tau + \Delta\tau_M)\cos(\varphi + \Delta\gamma_M)} \Leftrightarrow \frac{Q^k}{I^k} = \tan(\tilde{\varphi}) \quad (3.33)$$

The main goal of the carrier lock-loop, depicted in Figure 3.15, is to try to minimize the discriminator function, i.e., the difference between the local replica and the incoming signal, which has unpredictable embedded dynamics. As soon as the feedback control loop achieves steady state, that is, the incoming signal is perfectly aligned with the local replica (meaning that the receiver is able to obtain the receiver-to-satellite *Doppler* shift)

then the phase-error (discriminator) φ is zero, or at least its mean value tends to zero.

Therefore:

$$\frac{Q^k}{I^k} = \frac{\alpha_M C^k(\tau + \Delta\tau_M) \sin(\Delta\gamma_M)}{C^k(\tau) + \alpha_M C^k(\tau + \Delta\tau_M) \cos(\Delta\gamma_M)} = \tan(M) \quad (3.34)$$

Where $\tilde{\varphi}$ is now the just carrier-phase multipath signal, that is $\tilde{\varphi} \equiv M$, which can be obtained from:

$$\tan(M) = \frac{\alpha_M C^k(\tau + \Delta\tau_M) \sin(\Delta\gamma_M)}{C^k(\tau) + \alpha_M C^k(\tau + \Delta\tau_M) \cos(\Delta\gamma_M)} \Leftrightarrow \quad (3.35)$$

$$M = a \tan \left[\frac{\alpha_M C^k(\tau + \Delta\tau_M) \sin(\Delta\gamma_M)}{C^k(\tau) + \alpha_M C^k(\tau + \Delta\tau_M) \cos(\Delta\gamma_M)} \right]$$

This is basically the discriminator output of the carrier tracking-loop when in steady-state mode, thus it is the carrier-phase observable multipath error from a specular strong reflector. Putting together the two correlation functions (the multipath-biased and the unbiased) in one:

$$\alpha' = \frac{C^k(\tau + \Delta\tau_M)}{C^k(\tau)} \quad (3.36)$$

and substituting in Equation 3.35 then we obtain:

$$M = a \tan \left[\frac{\alpha_M C^k(\tau + \Delta\tau_M) \sin(\Delta\gamma_M)}{C^k(\tau) + \alpha_M C^k(\tau + \Delta\tau_M) \cos(\Delta\gamma_M)} \left(\frac{\alpha'}{\alpha} \right) \right] \quad (3.37)$$

which results in the following equation:

$$M = a \tan \left[\frac{\alpha_M \alpha' \sin(\Delta\gamma_M)}{1 + \alpha_M \alpha' \cos(\Delta\gamma_M)} \right] \quad (3.38)$$

The quantity $\alpha_M \cdot \alpha'$, which represents the composed effect of the specular reflector reflection coefficient, and the receiver tracking-loop correlation function, is usually considered a damping factor (“absorbs” the energy of the non-LOS GNSS signal). It would be rather difficult (and uninteresting for that matter) to separate these two terms, thus the damping factor, $\beta = \alpha_M \cdot \alpha'$, can be introduced in Equation 3.38 resulting in:

$$M = a \tan \left[\frac{\beta \sin(\Delta\gamma_M)}{1 + \beta \cos(\Delta\gamma_M)} \right] \quad (3.39)$$

This is exactly the carrier-phase multipath equation provided in this dissertation second chapter (GNSS concepts and signal errors). In that chapter it was mentioned that the equation was based on rather simple geometric concepts, however we have just herewith demonstrated that despite that it clearly has a realistic physical meaning, at least from the receiver tracking point-of-view. One can see in next figures some examples of this one-

antenna multipath equation (using also the concrete-made reflection coefficient function) for two different reflector distances.

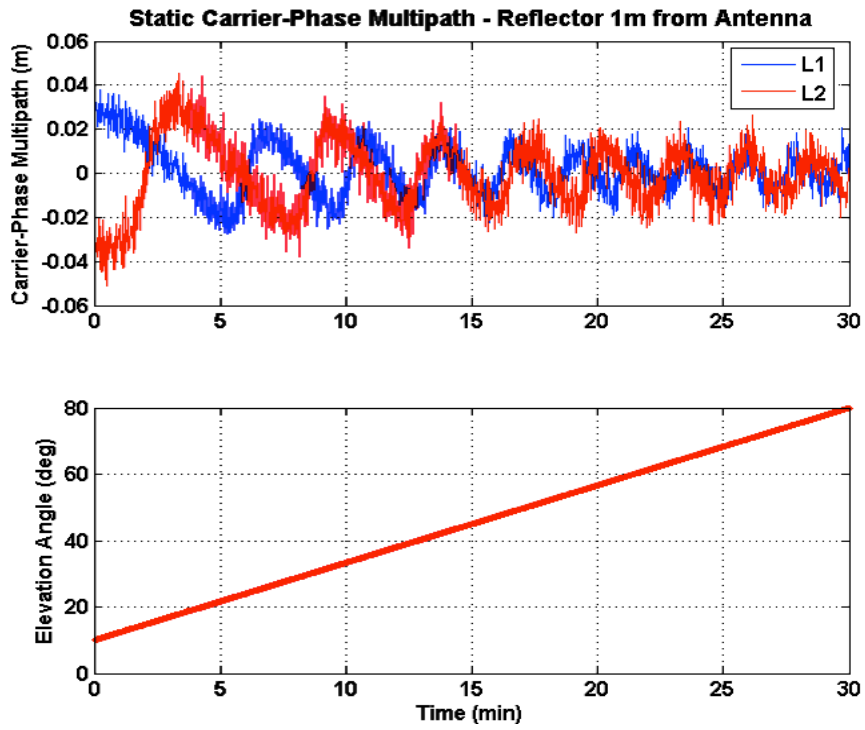


Figure 3.17: Static carrier-phase multipath for GPS L_1 and L_2 (1 meter distance reflector)

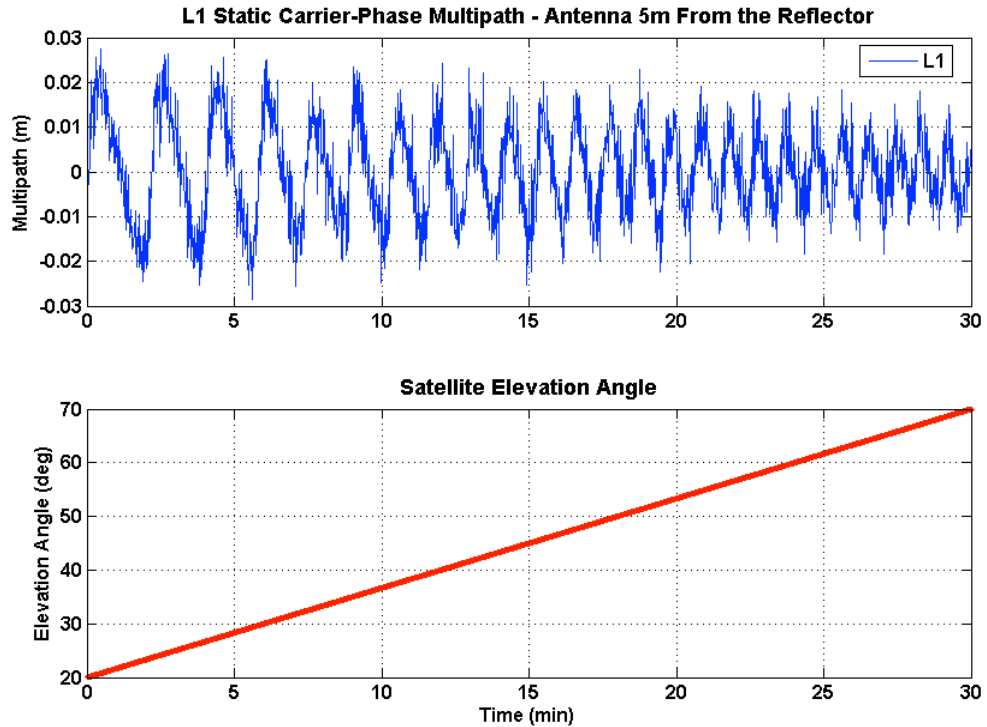


Figure 3.18: Static carrier-phase multipath for GPS L_1 (5 meter distance reflector)

We can take some evidences from the simulation results depicted in previous plots:

1. The carrier-phase multipath signal signature, unlike the code observable and despite being a very pronounced deterministic harmonic signal, is zero-mean valued (in the absence of colored noise). It would be possible to average out the multipath bias with a long time-series, and in a post-processing mode.

However for real-time applications, i.e. in GNSS-RTK scenarios, that simply is not an option, and therefore it remains one of the most difficult sources of error to model or mitigate.

2. The closer the antenna is to the reflector the lower the carrier-phase multipath frequency is. It makes sense because a bigger distance from a reflector creates more Fresnel zones which lead to a higher pool of potential frequency components.

3. The multipath signal amplitude is a function of the satellite elevation angle variation. This is due to the amplitude being affected by the energy absorbed by the reflector, and in turn this is a function of the satellite signal incidence angle (and obviously from the reflector-made material).

4. Not very clear from these plots (but later on from the dual antenna multipath plots) is the fact that carrier-phase multipath is uncorrelated even for short distances. This means that within two contiguous antennas multipath will not cancel out even in the face of a very strong reflector upon two antennas separated by just a few centimetres.

5. However carrier-phase multipath in a static antenna scenario, with unchangeable multipath reflector conditions and positioning is very repeatable on a daily basis, i.e., for same satellite orbit and some multipath scenario conditions [Bilich *et al.*, 2006]. Thus multipath is highly temporally correlated and not spatially correlated (unless of course one uses a zero-baseline single-antenna, dual-receiver system).

3.6 Carrier-phase multipath in a GNSS dual-antenna system

In order to obtain a composed carrier-phase multipath equation for a dual-antenna system one has to use again Eq. 3.34 and change the indexes for each antenna accordingly, that is:

$$M_0 = \arctan \left[\frac{\beta_0 \sin(\Delta\gamma_0)}{1 + \beta_0 \cos(\Delta\gamma_0)} \right] \quad M_1 = \arctan \left[\frac{\beta_1 \sin(\Delta\gamma_1)}{1 + \beta_1 \cos(\Delta\gamma_1)} \right]$$

Now using the following trigonometric identity:

$$\arctan \alpha \pm \arctan \beta = \arctan \left(\frac{\alpha \pm \beta}{1 \mp \alpha\beta} \right) \quad (3.40)$$

where α and β are the argument of the equations M_0 and M_1 respectively. We obtain then with simple algebraic manipulations:

$$\Delta M_{01} = \left(\frac{\beta_0 \sin \Delta\gamma_0 + \beta_0 \beta_1 \sin \Delta\gamma_0 \cos \Delta\gamma_1 - \beta_1 \sin \Delta\gamma_1 - \beta_0 \beta_1 \sin \Delta\gamma_1 \cos \Delta\gamma_0}{1 + \beta_1 \sin \Delta\gamma_1 + \beta_0 \beta_1 \cos \Delta\gamma_0 \cos \Delta\gamma_1 + \beta_0 \cos \Delta\gamma_0 + \beta_0 \beta_1 \sin \Delta\gamma_0 \sin \Delta\gamma_1} \right) \quad (3.41)$$

and using again another two trigonometric identities:

$$\begin{aligned} \sin(\alpha \pm \beta) &= \sin \alpha \cos \beta \pm \cos \alpha \sin \beta \\ \cos(\alpha \pm \beta) &= \cos \alpha \cos \beta \mp \sin \alpha \sin \beta \end{aligned} \quad (3.42)$$

we obtain then the composed carrier-phase multipath equation for a dual-antenna system:

$$\Delta M_{01} = \arctan \left[\frac{\beta_1 \sin(\Delta\gamma_1) - \beta_0 \sin(\Delta\gamma_0) + \beta_0 \beta_1 \sin(\Delta\gamma_1 - \Delta\gamma_0)}{1 + \beta_1 \cos(\Delta\gamma_1) + \beta_0 \cos(\Delta\gamma_0) + \beta_0 \beta_1 \cos(\Delta\gamma_1 - \Delta\gamma_0)} \right] \quad (3.43)$$

Because the specular reflector has bigger dimensions than the two antennas distance then the reflector reflection ratio is the same for both antennas. Plus the short distance among them also means that multipath time delay will be very similar and thus the receiver correlation properties will be very similar as well. In this case the dampening factor $\beta_0 \approx \beta_1$, and thus:

$$\Delta M_{01} = \arctan \left[\frac{\beta \sin(\Delta\gamma_1) - \beta \sin(\Delta\gamma_0) + \beta^2 \sin(\Delta\gamma_1 - \Delta\gamma_0)}{1 + \beta \cos(\Delta\gamma_1) + \beta \cos(\Delta\gamma_0) + \beta^2 \cos(\Delta\gamma_1 - \Delta\gamma_0)} \right] \quad (3.44)$$

Just for the sake of simplicity we will use one common dampening factor to the two antennas, and only when a considerable distance separates the antennas it makes sense to use two different ones. Substituting Equation 3.17, that is the multipath phase-delay difference between two antennas:

$$\Delta\gamma_1 = \Delta\gamma_0 - \left[\frac{2\pi}{\lambda_{L_r}} dist_{01} \cos(\phi_0 - \varphi_{01}) \cos(\theta_0) \cos(\varepsilon_{01}) \right]$$

in Equation 3.44, we then obtain our sought single-difference (between static or moving baseline antennas) carrier-phase multipath equation with the unknown state vector parameters $[\beta \ \Delta\gamma_0 \ \varphi_0 \ \theta_0]$ in an explicit mode:

$$\Delta M_{01} = a \tan \left[\frac{\beta \sin \left[\Delta\gamma_0 - \frac{4\pi}{\lambda_{L_i}} \text{dist}_{01} \cos(\varphi_0 - \varphi_{01}) \cos(\theta) \cos(\varepsilon_{01}) \right] - \beta \sin(\Delta\gamma_0) + \beta^2 \sin \left[-\frac{4\pi}{\lambda_{L_i}} \text{dist}_{01} \cos(\varphi_0 - \varphi_{01}) \cos(\theta) \cos(\varepsilon_{01}) \right]}{1 + \beta \cos \left[\Delta\gamma_0 - \frac{4\pi}{\lambda_{L_i}} \text{dist}_{01} \cos(\varphi_0 - \varphi_{01}) \cos(\theta) \cos(\varepsilon_{01}) \right] + \beta \cos(\Delta\gamma_0) + \beta^2 \cos \left[-\frac{4\pi}{\lambda_{L_i}} \text{dist}_{01} \cos(\varphi_0 - \varphi_{01}) \cos(\theta) \cos(\varepsilon_{01}) \right]} \right] \quad (3.45)$$

This equation represents the MIMICS algorithm basis used throughout this dissertation. The needed steps to obtain this observable, from dual-antenna raw carrier-phase measurements, will be approached in next chapter. An example using real-live signals will be given and its respective geometric concept is also provided (Figure 3.19):

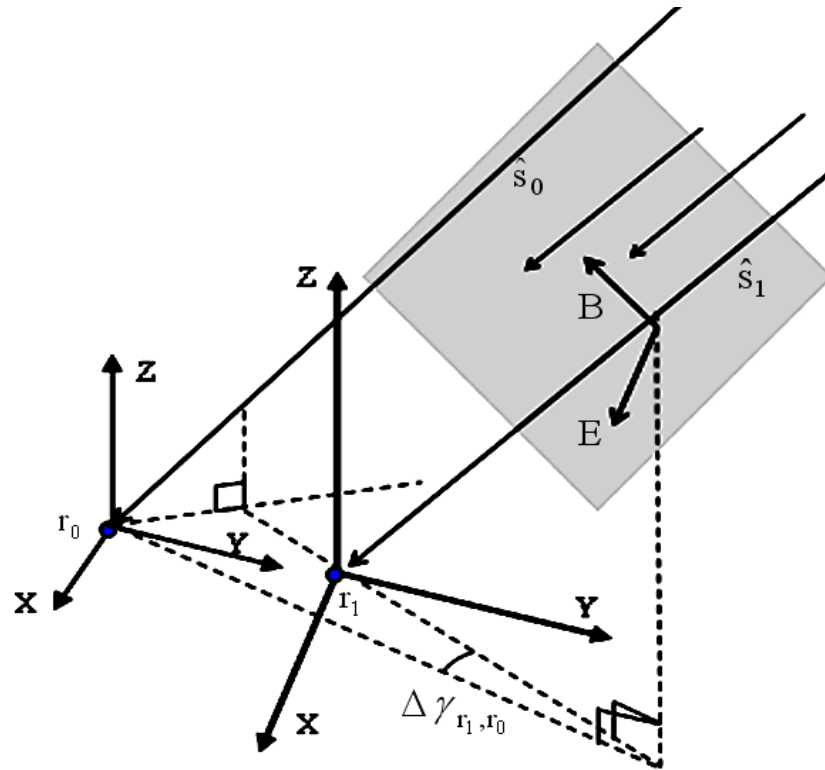


Figure 3.19: Geometric concept of a planar multipath wave incident upon a very short-spaced dual-antenna GNSS system

As explained before, uniform plane-waves are the most prolific tool in modeling and understanding electromagnetic multipath and near-field problems. Therefore we designed a system (Figure 3.20) that contains two closely-spaced antennas and a strong specular reflector (canvas with thin-foil) within a short distance from the antennas (around 1m).

With this setup we make sure that the multipath reflections arising from the specular reflector impact both antennas, as depicted in Figure 3.19. Moreover the antennas can rotate around the bore-sight-axis passing through the master antenna.

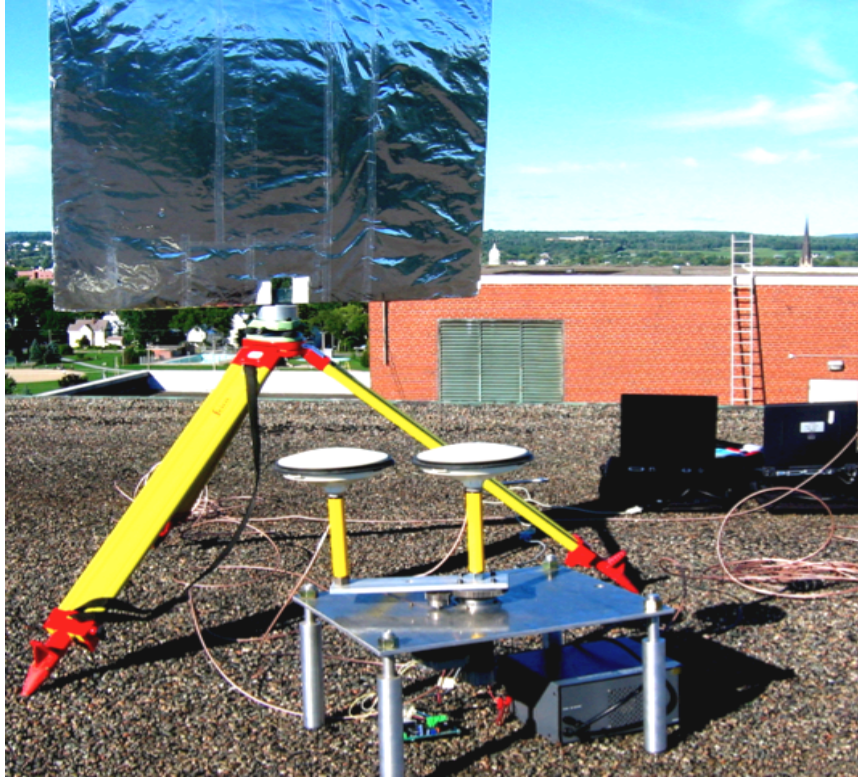


Figure 3.20: Short-spaced dual-antenna system with a strong specular reflector within 1m

The results from this test can be seen in next figures. The test itself was made on the roof of UNB's Engineering department to make sure that the only reflections tracked by the GNSS antennas would come from the simulated specular reflector.

As mentioned, the antennas can be rotated through a stepped motor attached to the master antenna axis (Figure 3.20). This way one can emulate more realistic scenarios, where a GNSS dual-antenna system orientation changes in respect to the specular reflector.

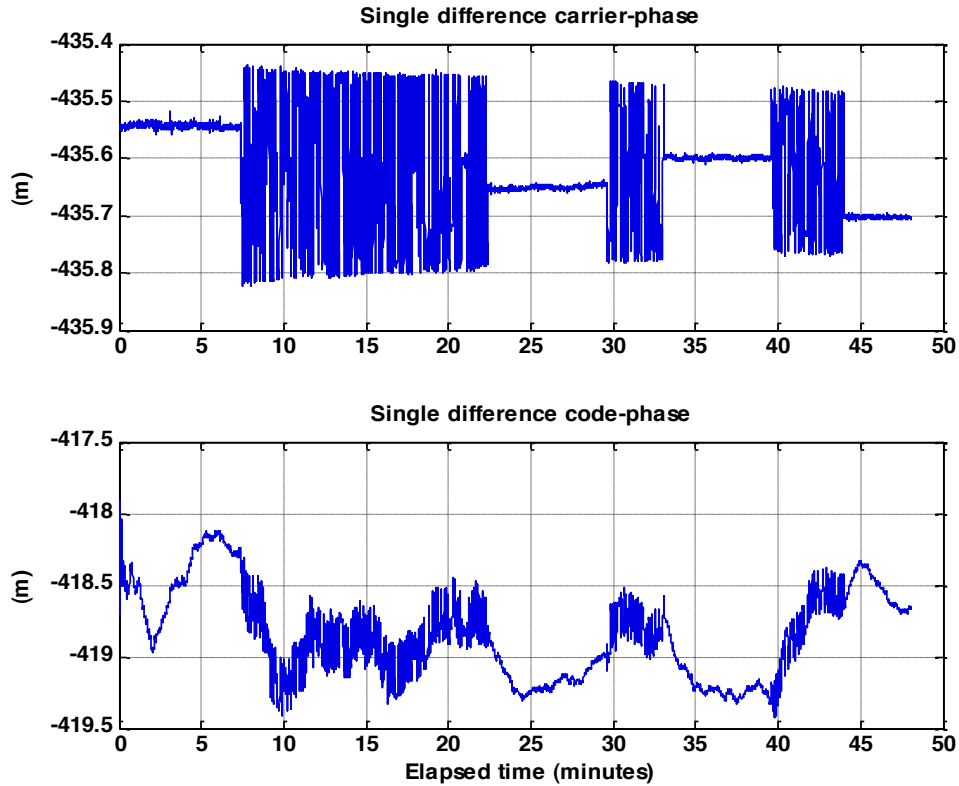


Figure 3.21: Results from the test setup depicted in previous figure

The top plot from Figure 3.21 depicts the results from the single-difference carrier-phase, and the bottom from single-difference code pseudo-ranges. The thicker part represents the periods when the antennas were performing a circular random motion. The thin noisy line represents obviously the moments when there was no motion.

Regarding just the single-difference code observable (bottom plot) one can see that throughout the test multipath is quite significant, regardless of the antennas being static or rotating. With such a short distance between the antennas, we can be sure that the

sinusoidal-shaped signal in the plot is due to the specular reflector multipath, as the remaining errors are cancelled out.

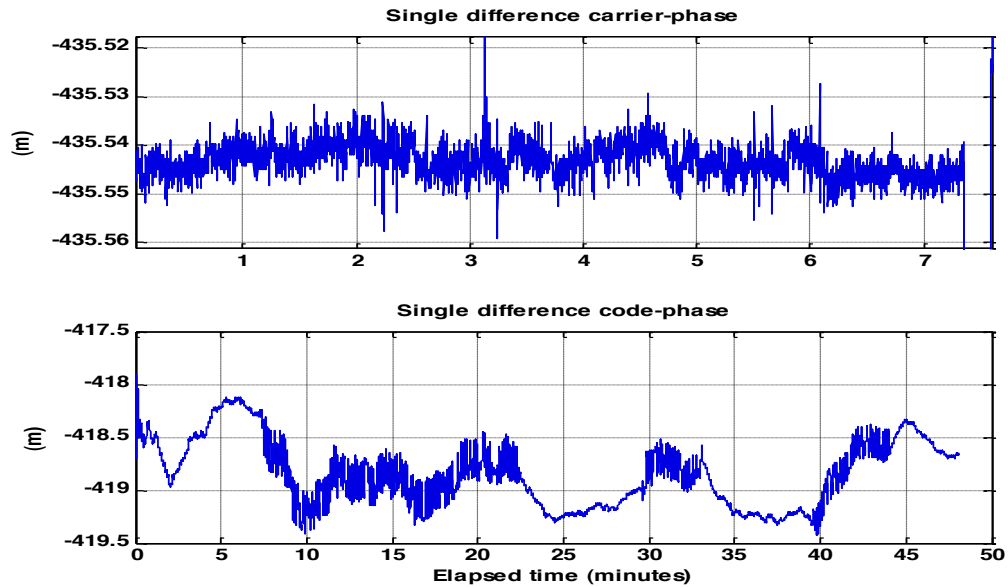


Figure 3.22: In the top plot we can see a zoom to the first seven minutes of carrier-phase data (no motion)

Making a zoom to the top plot in Figure 3.21 we can see the results from differencing the carrier-phase observable (between antennas). Analogous to the code observable differencing, the only remaining error is the carrier-phase multipath, plus an ambiguity).

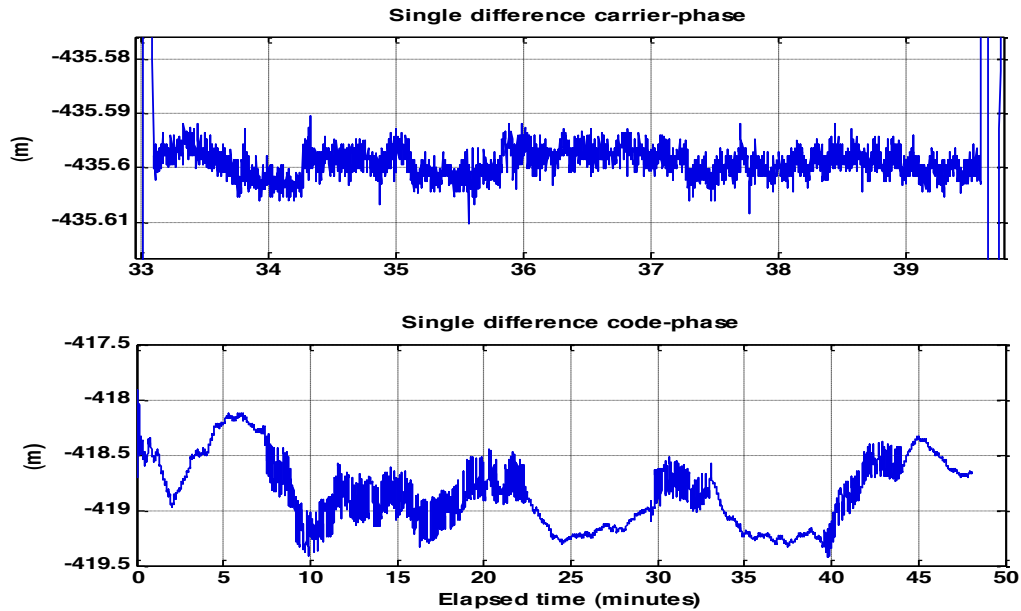


Figure 3.23: Zoom to another segment of carrier-phase data when in static mode (again the x-axis is in minutes)

Figure 3.22 refers to a zoom to the first 8 minutes, and Figure 3.23 to the period between 33 and 40 minutes, between two random rotation motions. As mentioned before, regardless of how close the antennas are, carrier-phase multipath will not be removed through differencing. Moreover one can appreciate the expected sinusoidal pattern with periods of a few minutes, and also the signal amplitude of a few centimetres.

We also used the previously developed multipath equations to simulate multipath in several scenarios, and depicted in the following figures (as a note, simulated data from Equation 3.39 for each antenna was differenced and compared with simulated data from

the composed model given by Equation 3.45 - both gave the same results). The first scenario is depicted in Figure 3.24:

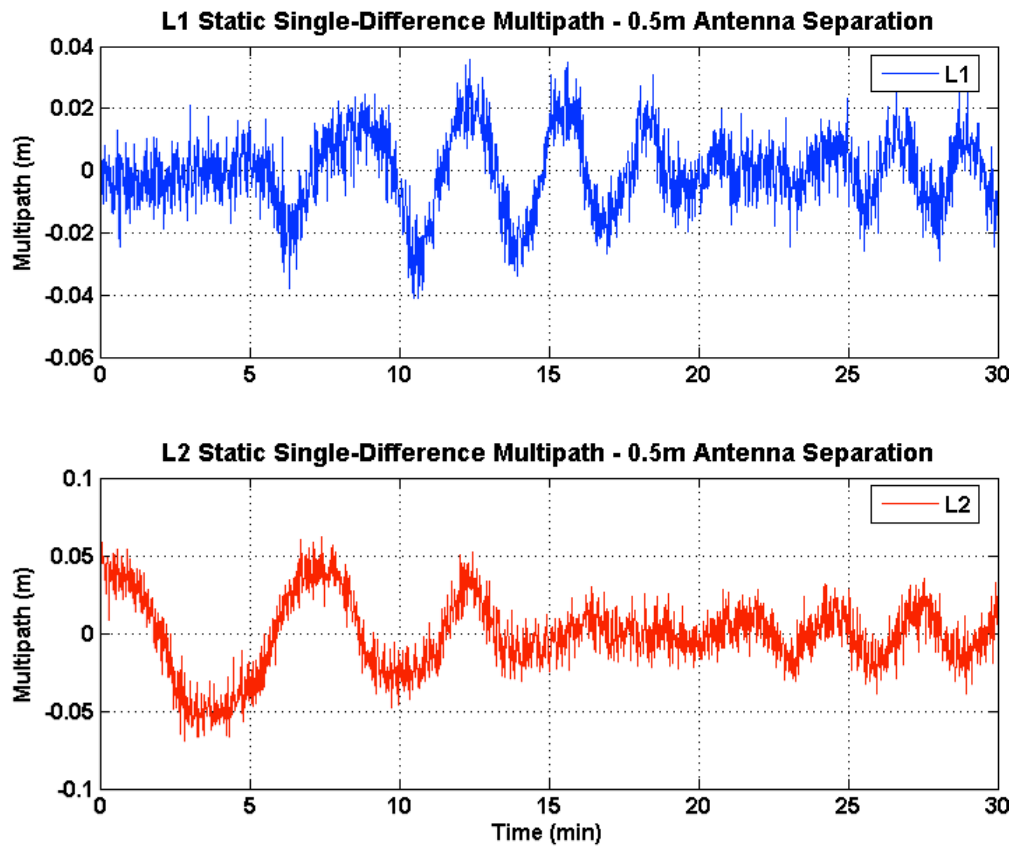


Figure 3.24: GPS L_1 and L_2 static carrier-phase multipath from a specular reflector (antenna separation is 0.5m and the reflector is at 1m distance)

One can see from the simulations that the single-difference multipath phase can vary considerably between GPS L_1 and L_2 signals, depending on the reflector's relative geometry to the GNSS dual-antenna system.

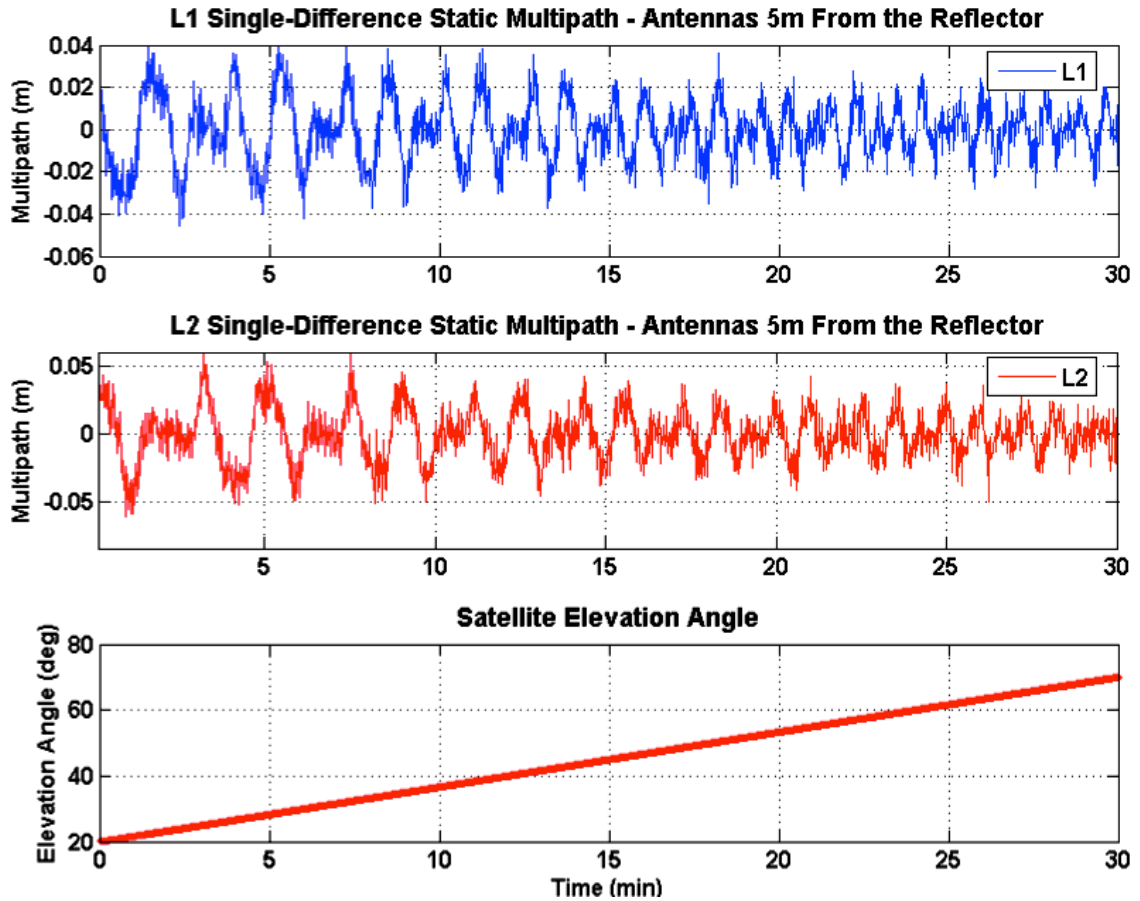


Figure 3.25: Same scenario as before (0.5m antenna separation) however the reflector is at a distance of 5m

In Figure 3.25 one used the same simulation scenario where the antennas are 0.5m spaced, and the common specular reflector is at a distance of 5m. As expected, the farther away the reflector, the higher the single-difference multipath frequency.

To conclude, we also wanted to appreciate, from software simulations, the single-difference carrier-phase multipath signature when the antennas are in kinematic mode (hence there is motion between them).

This is something very important, as we will notice in future chapters, that in order to separate the single-difference carrier-phase multipath signature from raw-data it is necessary that the antennas have some sort of motion, optimally random motion (which can be “forced” by the platform or obtained through a mathematical randomization).

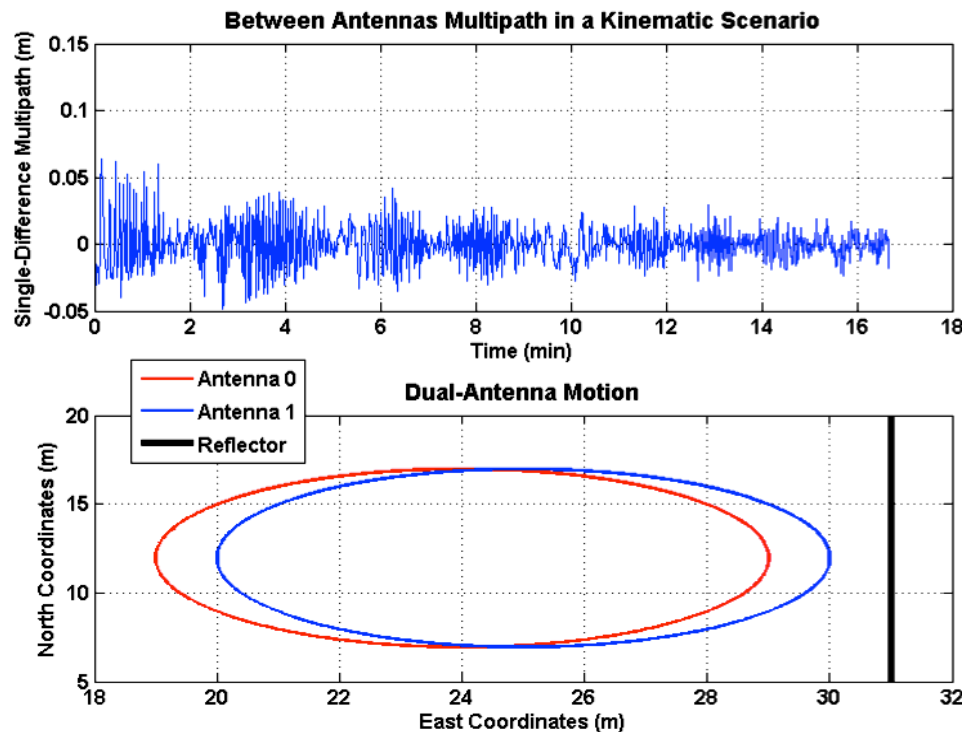


Figure 3.26: Carrier-phase multipath from a dual-antenna system performing a circular motion

This kind of random motion, from Figure 3.26, was implemented in the system depicted at Figure 3.20. In a real-life scenario it is not uncommon for machine operators to perform a similar random motion during the system initialization. For instances, this is

done with a dozer's blade with GNSS receivers on both masts (and usually with an inertial sensor system in the back of the blade) where the blade can rotate in 3 degrees of freedom.

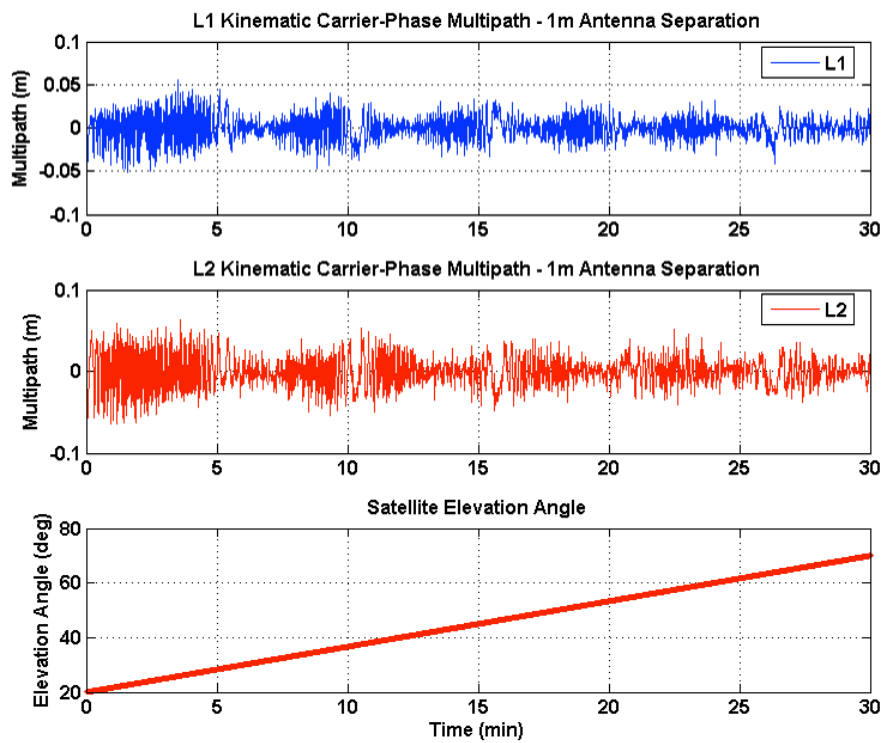


Figure 3.27: Same as before but showing the satellite elevation angle variation

The last plot (Figure 3.27) depicts the same simulation as in Figure 3.26, however here one can see the satellite elevation angle rising while the single-difference multipath amplitude shortens.

4 MIMICS Strategy

4.1 Concept behind the MIMICS algorithm

Differential carrier-phase GPS-based attitude determination represents an attractive and very smart alternative to expensive and complex inertial measurement units (IMUs) and attitude heading reference systems (AHRS), for aeronautical, marine and machine-guidance applications. Previous work in GPS-based attitude systems, using ultra-short baseline (less than a couple of metres) between three/four antennas, have been shown to provide high accuracies, most of the time to the sub-degree level in yaw, pitch and roll.



Figure 4.1: Inertial Aided GPS Based Attitude Heading Reference System (AHRS) for General Aviation Aircraft. Note the four GPS patch antennas on the aircraft body (figure taken from [Barrows *et al.*, 1996]).

If the relative position of three or more antennas can be determined with a real-time centimetre-level accuracy using the carrier phase observables (thus in RTK-mode) the three attitude parameters (heading, pitch and roll angles) of the platform can be estimated. The observation equation representing this concept is given by:

$$\Delta\nabla\Phi = E \cdot R_e^1 \cdot R_1^b \cdot X_b + \Delta\nabla N + \Delta\nabla M + \Delta\nabla \zeta \quad (4.1)$$

where $\Delta\nabla\Phi$ are the double-difference carrier-phase measurements (between two contiguous antennas and two satellites), E denotes the coefficient matrix of the double-differenced unit vectors between the antenna baselines to the satellites, X_b are the antenna vectors in the body-frame, and R_e^1 is the transformation matrix between the local-level frame and the e-frame (also known as the ECEF-frame), $\Delta\nabla N$ are the double-differenced ambiguities, and $\Delta\nabla M$ is the double-differenced multipath.

The transformation matrix R_1^b has different forms dependent on the rotation sequence around the axis of the body-frame [El-Mowafy *et al.*, 2005]. Attitude parameters estimated from any of these forms should be numerically equivalent. One of these forms is given by Equation 4.2:

$$\mathbf{R}_1^b = \begin{bmatrix} c(\psi)c(\varphi) - s(\psi)s(\theta)s(\varphi) & s(\psi)c(\varphi) + c(\psi)s(\theta)s(\varphi) & -c(\theta)s(\varphi) \\ -s(\psi)c(\theta) & c(\psi)c(\theta) & s(\theta) \\ c(\psi)s(\varphi) + s(\psi)s(\theta)c(\varphi) & s(\psi)s(\varphi) - c(\psi)s(\theta)c(\varphi) & c(\theta)c(\varphi) \end{bmatrix} \quad (4.2)$$

Where c, and s stand for the co-sinus and sinus functions, respectively. Therefore a simple estimation of the attitude parameters can be carried out as follows:

$$\begin{aligned} \text{Heading } (\psi) &= -a \sin\left(\frac{\mathbf{R}_l^b(2,1)}{\mathbf{R}_l^b(2,2)}\right) \\ \text{Pitch } (\theta) &= a \sin(\mathbf{R}_l^b(2,3)) \\ \text{Roll } (\varphi) &= -a \tan\left(\frac{\mathbf{R}_l^b(1,3)}{\mathbf{R}_l^b(3,3)}\right) \end{aligned} \quad (4.3)$$

From Equation 4.1 it is clear that carrier-phase multipath is one of the most limiting factors in accuracy and reliability (meaning that it will hinder the correct estimation of $\Delta\nabla N$) regarding GPS-based attitude systems. Even a small separation between the antennas causes different and de-correlated phase-multipath errors (thus not removed from differencing among the antennas).

Moreover using typical choke-ring antennas to reduce multipath is not practical (not to mention cost prohibitive) when employing three or four antennas in dynamic platforms.



Figure 4.2: A dual-antenna GNSS-based orientation system used on an excavator
(Trimble GCS900 on an excavator with dual GPS – Trimble website)

However, with only two GNSS antennas (as seen in the excavator depicted in Figure 4.2) it is possible to determine yaw and pitch angles, which for some applications are sufficient such as for precision agriculture, construction (Figure 4.2, though here heading and pitch angles are the most important), and maritime applications (Figures 4.3, and 4.4). Depending on their placement in the platform body it makes the determination of these two angles quite robust and efficient.



Figure 4.3: A dual-antenna GNSS-based orientation system used on maritime applications (Magellan 3011 system)



Figure 4.4: Another dual-antenna system used on maritime applications (Sperry Marine dual antenna system)

Based on that concept, at UNB we have been developing carrier-phase multipath-mitigation procedures for kinematic applications, using single-difference multipath

observables with a dual-antenna system. These observables are obtained from the higher-order range-dynamic observations coming from the two antenna pseudo-random motions in kinematic applications, and therefore these are dedicated algorithms independent of the receivers/antennas chosen.

Instead of developing complex navigation and fusion algorithms with the output of GNSS and IMUs (hence having to take care of their inherent biases and scale-factors [Gang *et al.*, 2007]), a GNSS-based attitude system provides a complete navigation solution (position, velocity, and heading/attitude). Thus one can concentrate on mitigating multipath errors only using raw GNSS measurements and using “truth” platform-dynamic information. This information arises from a GNSS 3DoF (Degrees of Freedom) motion-table, such as the one depicted in next figure:

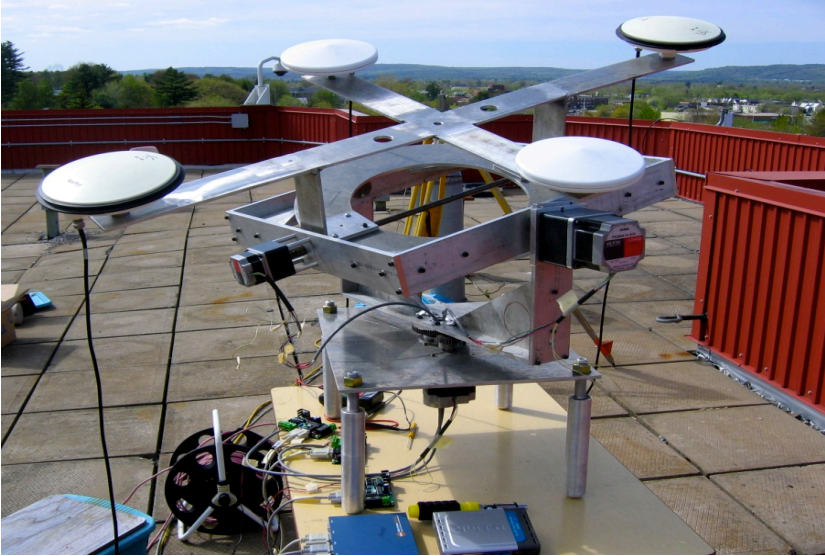


Figure 4.5: UNB motion-table platform for GNSS-based Heading/Attitude system studies

The motion-table allows us to easily compare synchronized kinematic data from the multi-antenna in the body-frame (measured *a priori* accurately) and data in the navigation-frame (as in any GNSS system output). Besides, it also allows the derivation of optimal lengths for the dual-antenna system baseline, depending on the platform structure and possible multipath reflectors.

4.2 MIMICS Algorithm and Specular Carrier-Phase Multipath

There are currently mainly three methods to mitigate, or at least ameliorate, the carrier-phase multipath error effect on precise (in real-time or post-processing) GNSS applications:

1. Receiver and antenna robust design against the multipath spectra (to the highest possible extent);
2. Careful selection of site or location on a platform of the antenna(s), in order to avoid to a maximal extent the multipath effect;
3. Carrier-phase multipath processing (dedicated algorithms);

The first method requires specific hardware design (with an emphasis on the research level and allocation of resources) and historically has been quite successful tackling most of the multipath errors, especially on the code observable.

The second method is the simplest and most cost-effective. However, it is very limited in terms of applicability, especially when the site scenario changes rapidly as is the case in kinematic applications.

The last method is the one chosen in this dissertation for tackling the carrier-phase multipath problem for several reasons: firstly, it does not require a big investment in the receiver/antenna design part (which for many companies is certainly a plus); secondly, it can be easily adaptable to several applications (since it is mainly dependent on the software/firmware side). Finally, it is independent of the hardware chosen (of course, with some adaptation in the software).

It certainly also has a few negative aspects. For example, the filtering of multipath will always have some time-latency in order to process the actual epoch of data being used. However, since most of the RTK applications use a high data rate of up to 20 Hz, this may not be a real problem. Besides, the more problematic low-frequency multipath has periods stretching from a few minutes to tens of minutes.

This approach uses a pair of antennas, connected to the same oscillator (to remove the common receiver clock bias), and distanced between each other sufficiently, but close enough to sense the same effective reflector (meaning that the reflector reflecting section is much bigger than the distance between the antennas). This method was developed having in mind how to obtain an observable that would physically mimic, or represent the between-antenna multipath effect.

Once this observable is found, its parameterization is based on the geometric parameters between the antennas and reflector(s). Therefore, the multipath effect at each antenna is recovered and its effect is corrected at each antenna.

It is almost impossible to obtain and separate a multipath observable for just one antenna, especially in near real-time scenarios. Therefore the two-antenna system would incorporate the advantages of eliminating most of the common biases to both antennas, while still keeping a clear and distinct multipath signature due to the high multipath decorrelation even for short distanced antennas.

This advantage is certainly a necessary condition in this study, and comes from the fact that carrier-phase multipath errors, unlike other biases, are not eliminated after differencing the measurements obtained from two close-by antennas. Furthermore, this fact can be accurately explained by the theory of uniform plane wave fields.

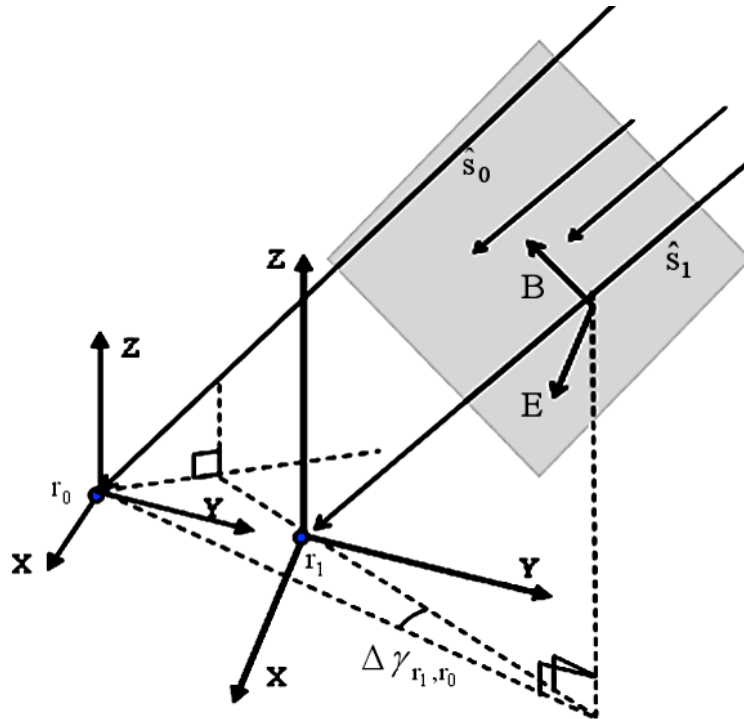


Figure 4.6: Geometric view of a uniform plane wave field with two antennas close to each other (r_0 and r_1 are the three-dimensional phase-center coordinates of master and slave antenna, respectively)

From the definition of a uniform plane wave, we note that such a wave not only is locally plane (i.e., it has B , E and \hat{s} everywhere spatially orthogonal to each other, where B is the magnetic field, E the electric field, and \hat{s} is the unit direction vector), but truly plane [McNamara *et al.*, 1990]. Uniform plane waves are the workhorse of engineering scattering problems due to the ease in defining trajectories for ray path tracing (which allows the study of polarization, as well as the variation of amplitude and phase along the ray path).

In practice, launching a single ray is not possible; however one can work with a selected axial ray plus an infinite number of rays surrounding it. Because the vectors \hat{s} are perpendicular to surfaces of constant phase (equi-phase surfaces), the rays defined earlier are normal to these surfaces. Therefore, B , E and \hat{s} are mutually perpendicular at any point on a ray, and there are no field components in the propagation direction.

The ray picture of such a uniform wave is shown in last figure (Figure 4.6), with all rays normal to the equi-phase surfaces. It emphasizes the fact that, as far as ray representation is concerned, such a uniform plane wave consists of infinitely many parallel rays propagating in the direction \hat{s} .

In our study, these relationships are very important due to the fact that we are considering the multipath errors arising from smooth, almost perfect reflectors, which cause the most serious multipath spectra (specular), especially when the reflector is located within a short distance of the antenna(s).

Any change in the relative position between antennas most likely will affect in a small scale the amplitude and polarization of the signals reflected and sensed by the two antennas (depending on their distance). However, the phase will definitely change significantly along the ray trajectory between the plane waves passing through each of the antennas.

This can be seen in Equation 3.43, which describes the single-difference multipath between two close antennas. It was mathematically derived in chapter 3 and it is given by:

$$\Delta M_{0,1}^q = M_0^q - M_1^q = \arctan\left(\frac{\beta_1 \sin \Delta\gamma_1 - \beta_0 \sin \Delta\gamma_0 + \beta_0 \beta_1 \sin(\Delta\gamma_1 - \Delta\gamma_0)}{1 + \beta_1 \cos \Delta\gamma_1 + \beta_0 \cos \Delta\gamma_0 + \beta_0 \beta_1 \cos(\Delta\gamma_1 - \Delta\gamma_0)}\right)$$

where the angle $\Delta\gamma_1 - \Delta\gamma_0 = \delta\Delta\gamma_{1,0}$ (depicted in Figure 2) is the relative multipath phase-delay between the antennas and a close effective reflector (β_0 and β_1 are the multipath signal amplitudes in master and slave antennas respectively, and are dependent on the reflector characteristics - reflection coefficient - and receiver tracking-loop).

Having this important concept in mind, which represents the physical foundation of the current study, one can define the steps involved in our strategy to mitigate (or ameliorate) the multipath effect.

4.3 MIMICS Algorithm Steps

As this study is based on an objective to mimic as much as possible the multipath effect from effective reflectors in kinematic scenarios with variable dynamics we decided to name the strategy **MIMICS** (**M**ultipath Profile From Between ReceIvers Dyna**MICS**).

The steps involved in this algorithm (which was meant and developed to be used in real-time applications), is given in next figure:

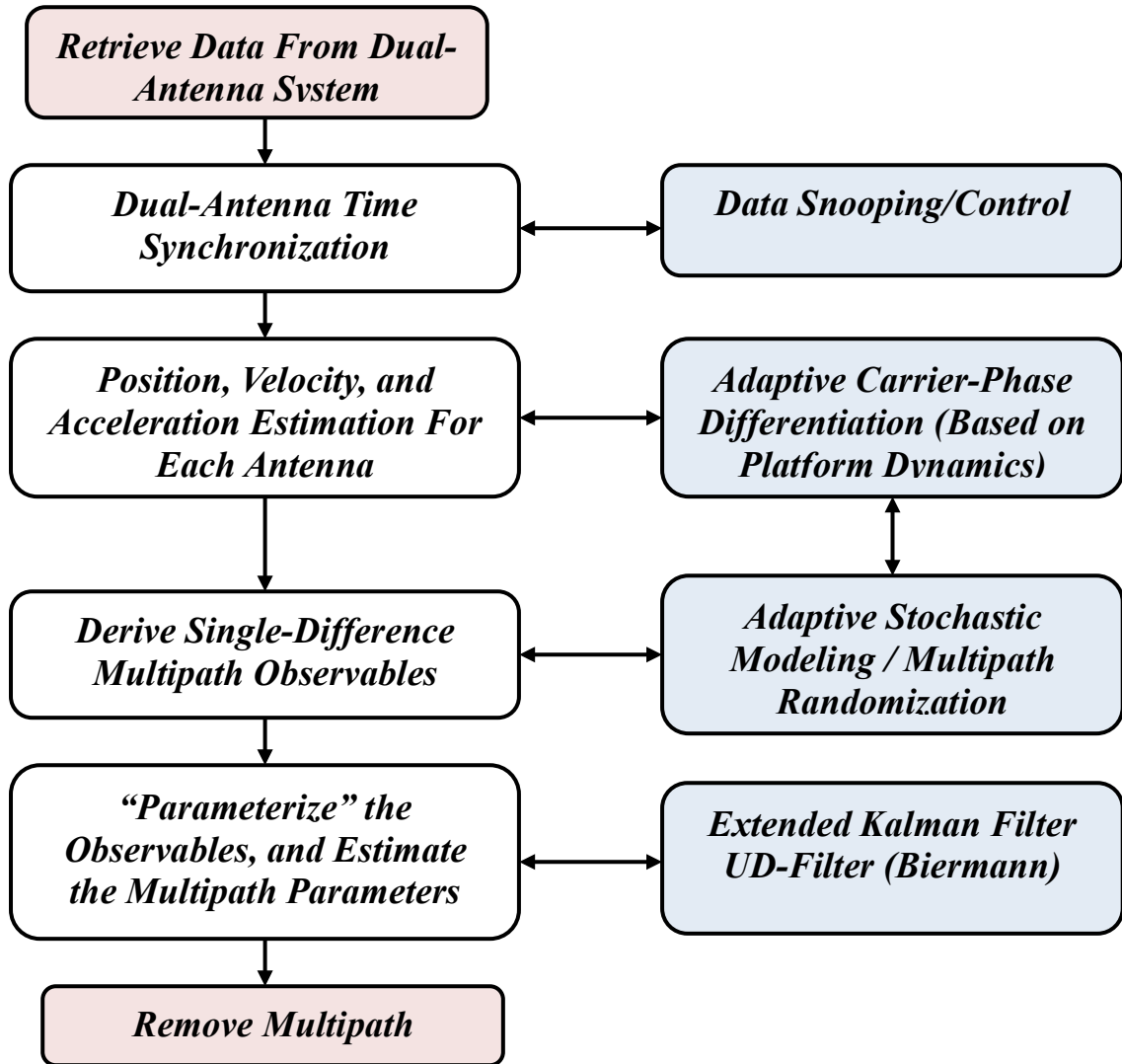


Figure 4.7: Steps involved in the **MIMICS** strategy

Starting with the first step, data from both receivers are collected and synchronized. An external oscillator is used to supply the same frequency to both receivers in order to eliminate, through differencing, the common receiver-clock biases (Figure 4.8).

This step also involves data quality control due to the fact that outliers are very common, where the most important are due to cycle-slips. Since the multipath observables are developed based on data time-filtering, it is essential to detect any nonconformity between measurements from the two receivers that could lead to erroneous multipath estimates.



Figure 4.8: Temex LPFRS-01/5M external oscillator used in our studies, connected to an oscilloscope

In the second step an approximate position for both antennas is necessary, but can be relaxed to a few metres using a standard code solution. This highlights the fact that one does not need to fix the ambiguities in order to fix multipath on carrier-phase (as long as we know the distance and orientation between the antennas), as is done in other approaches.

However, a very precise estimation of both antenna's velocity and acceleration (in real-time) is carried-out using the carrier-phase observable. Not only the antenna's velocity and acceleration estimates should be very precise (on the order of a few mm/s, and mm/s² respectively) but also immune to low-frequency multipath signatures.

This is another necessary condition in our approach, as we use the antenna's multipath-free dynamic information to separate multipath from raw data (this will explained later within the ideal digital differentiation concept).

The observation equation for a single-difference between receivers, using a common external clock (oscillator) to remove the common clock bias is given by:

$$\Delta\Phi_{m,s}^{prn}(t_k) = \Delta\rho_{m,s}^{prn}(t_k) + \Delta N_{m,s}^{prn} + \Delta M_{m,s}^{prn}(t_k) + \Delta\mathcal{E}_{m,s}^{prn}(t_k) \quad (4.4)$$

where the terms stand for:

m: master antenna

s: slave antenna

prn: satellite

Δ : operator for single-difference between receivers

Φ : carrier-phase observation

ρ : slant range between satellite and receiver

M: multipath

ε : system noise

By differencing in time (4.4) to remove the single-difference ambiguity from the observation equation, we obtain (as long as there is no loss-of-lock or cycle-slips):

$$\delta\Delta\Phi_{m,s}^{prm}(t_k, t_{k-1}) = \delta\Delta\rho_{m,s}^{prm}(t_k, t_{k-1}) + \delta\Delta M_{m,s}^{prm}(t_k, t_{k-1}) + \delta\Delta\varepsilon_{m,s}^{prm}(t_k, t_{k-1}) \quad (4.5)$$

where:

$$\delta\Delta\rho_{m,s}^{prm}(t_k, t_{k-1}) = \Delta\dot{\rho}_{m,s}^{prm}(t_{k-1}) + \dots + \frac{\partial^n \Delta\rho_{m,s}^{prm}}{\partial t^n}(t_{k-1}) \frac{\delta t^n}{n!} \quad (4.6)$$

One of the key ideas to derive the multipath observable from Equation 4.4 is to estimate $\delta\Delta\rho_{m,s}^{prm}(t_k, t_{k-1})$ given by Equation 4.6. From Equation 4.5, at the second epoch, for example, we will have:

$$\delta\Delta M_{m,s}^{prm}(t_1, t_0) = \delta\Delta\Phi_{m,s}^{prm}(t_1, t_0) - \delta\Delta\rho_{m,s}^{prm}(t_1, t_0) \approx \Delta M_{m,s}^{prm}(t_1) - \Delta M_{m,s}^{prm}(t_0) \quad (4.7)$$

If we continue this process up to the epoch n , we will obtain an ensemble of differential multipath observations as follows:

$$\begin{aligned}
\delta\Delta M_{m,s}^{prn}(t_1, t_0) &= \delta\Delta\Phi_{m,s}^{prn}(t_1, t_0) - \delta\Delta\rho_{m,s}^{prn}(t_1, t_0) \approx \Delta M_{m,s}^{prn}(t_1) - \Delta M_{m,s}^{prn}(t_0) \\
\delta\Delta M_{m,s}^{prn}(t_2, t_1) &= \delta\Delta\Phi_{m,s}^{prn}(t_2, t_1) - \delta\Delta\rho_{m,s}^{prn}(t_2, t_1) \approx \Delta M_{m,s}^{prn}(t_2) - \Delta M_{m,s}^{prn}(t_1) \\
&\vdots \\
\delta\Delta M_{m,s}^{prn}(t_n, t_{n-1}) &= \delta\Delta\Phi_{m,s}^{prn}(t_n, t_{n-1}) - \delta\Delta\rho_{m,s}^{prn}(t_n, t_{n-1}) \approx \Delta M_{m,s}^{prn}(t_n) - \Delta M_{m,s}^{prn}(t_{n-1})
\end{aligned} \tag{4.8}$$

If we take the numerical summation of (4.8), we will have:

$$\sum_{k=1}^n \delta\Delta M_{m,s}^{prn}(t_k, t_{k-1}) \approx \Delta M_{m,s}^{prn}(t_n) - \Delta M_{m,s}^{prn}(t_0) = \delta\Delta M_{m,s}^{prn}(t_n, t_0) \tag{4.9}$$

Note that n samples of differential multipath observations are used in (4.9). Therefore, we need $n+1$ observations.

Assume that we perform this process taking $n = 1$, then $n = 2$, and so on until we obtain r numerical summations of Equation 4.9 and then take a second numerical summation of them, we will obtain:

$$\begin{aligned}
\frac{1}{r} \sum_{n=1}^r \left[\sum_{k=1}^n \delta\Delta M_{m,s}^{prn}(t_k, t_{k-1}) \right] &\approx \sum_{n=1}^r \Delta M_{m,s}^{prn}(t_n) - \sum_{n=1}^r \Delta M_{m,s}^{prn}(t_0) \\
&= \sum_{n=1}^r \Delta M_{m,s}^{prn}(t_n) - r \cdot \Delta M_{m,s}^{prn}(t_0)
\end{aligned} \tag{4.10}$$

then,

$$\frac{1}{r} \sum_{n=1}^r \left[\sum_{k=1}^n \delta \Delta M_{m,s}^{prm}(t_k, t_{k-1}) \right] \approx \frac{1}{r} \sum_{n=1}^r \Delta M_{m,s}^{prm}(t_n) - \Delta M_{m,s}^{prm}(t_0) \quad (4.11)$$

Therefore we will end up with the following equation as:

$$E \left[\sum_{k=1}^n \delta \Delta M_{m,s}^{prm}(t_k, t_{k-1}) \right] \approx E \left[\Delta M_{m,s}^{prm}(t_n) \right] - \Delta M_{m,s}^{prm}(t_0) \quad (4.12)$$

where $E[]$ is the expectation operator. We can see in next figure (Figure 4.9) a graphical explanation on how one can obtain the aforementioned observation:

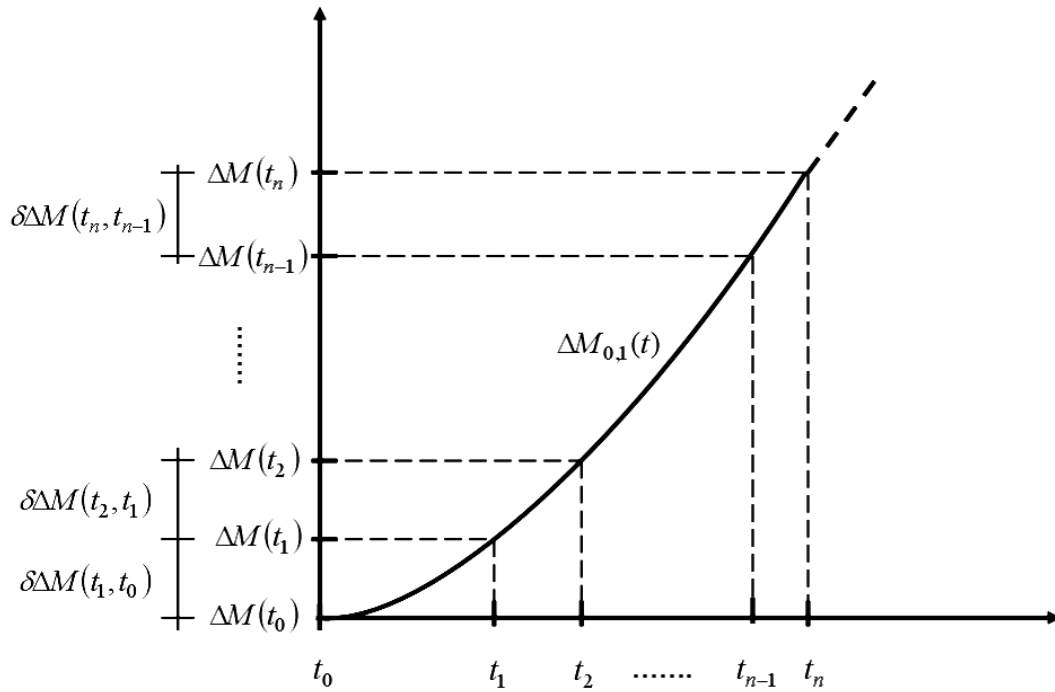


Figure 4.9: Graphic depicting the initial multipath bias to be obtained

To isolate the initial epoch multipath given by Equation 4.12, that is, $\Delta M_{m,s}^{prm}(t_0)$, from the differential multipath observations, the first term on the right-hand side, $E[\Delta M_{m,s}^{prm}(t_k)]$, should be removed.

This can be accomplished by mechanical calibration and/or numerical randomization. To summarize the idea, in order to separate the deterministic initial single-difference multipath bias, buried under correlated noise due to filter differentiations, it is necessary to “whiten” or randomize the differenced-in-time single-difference multipath observables.

The mechanical calibration may include the dual-antenna GNSS system performing random motions for a few minutes at the beginning of the test. The numerical randomization refers to the “whitening” algorithms included in the processing algorithms, and performed continuously on-the-fly. When the isolation of the initial multipath epoch is completed, we can recover the multipath observations at every epoch using (4.8) eventually.

4.4 - Central Difference Approximations

Because a digital differentiator is involved in the MIMICS strategy, it is important that one understands the concept of digital differentiators. An ideal digital differentiator can be written in the following form [Bruton *et al.*, 1999]:

$$H(e^{j\omega}) = j\omega, \text{ for } 0 \leq |\omega| \leq \frac{\omega_s}{2} \quad (4.13)$$

where ω is the frequency, ω_s is the sampling frequency and T is the corresponding sampling period. To differentiate a discrete time signal, such as GNSS data, one can use a discrete time convolution. In this case, the differentiator can be considered as a non-recursive or finite impulse response (FIR) filter. Practically, a FIR differentiator can be applied to a discrete data set, such as the (L_1) carrier-phase time series $\Phi(t)$, using a convolution as follows:

$$\dot{\Phi}(t) = \sum_{k=0}^{N-1} h(k)\Phi(t-k) \quad (4.14)$$

where $\dot{\Phi}(t)$ is the derivative of the input signal $\Phi(t)$ at time t , and h is the impulse response with order (N-1). Using sequentially this filter will create a time series of the carrier-phase $\dot{\Phi}(t)$. Applying the same convolution again, one obtains the range-rate change:

$$\ddot{\Phi}(t) = \sum_{k=0}^{N-1} h(k)\dot{\Phi}(t-k) \quad (4.15)$$

Theoretically, the relationship between the impulse response h and the ideal digital differentiator is given by:

$$h(nT) = \frac{1}{\omega_s} \int_{-\omega_s/2}^{\omega_s/2} H(e^{j\omega}) e^{j\omega nT} d\omega \quad (4.16)$$

Then, the design of a digital differentiator depends on the choice of the impulse response h and the order of the filter which is related to the length of the window. Ideally, the order should be chosen in a way that the filter frequency response should respect Equation 4.13. In case the digital differentiator is designed based on a central difference approximation, its order should be chosen to follow the “ideal” line depicted in next figure (Figure 4.10):

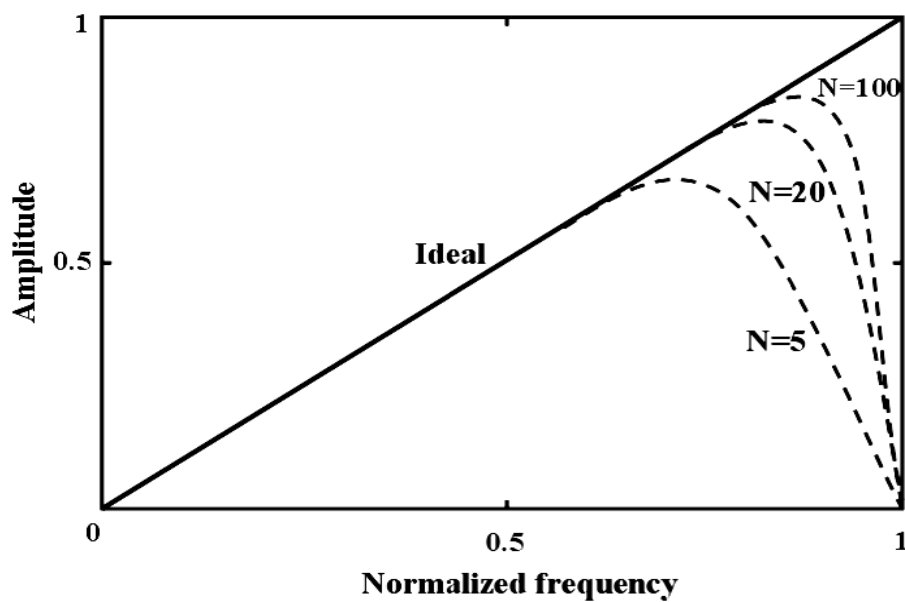


Figure 4.10: Central difference approximations of different orders

The approach of central difference approximations is one of important classes of FIR (Finite Impulse Response) differentiators, which are highly accurate at low to medium frequencies. In such an approach, both the backward and the forward values of a given function are used to approximate the derivative of the function. In this case, the derivative is obtained by solving a set of $2N$ equations obtained by $2N+1$ terms Taylor expansion of a function $f(t)$ at $t = kT$, $k = \pm 1, \pm 2, \dots, \pm N$. These equations can be written as:

$$\mathbf{f} = \mathbf{A} \cdot \mathbf{d} + \mathbf{r} \quad (4.17)$$

where \mathbf{f} and \mathbf{d} are the vectors of length $2N$, \mathbf{A} is a $2N \times 2N$ square matrix, and these are defined by the following matrices (Equations 4.18):

$$\mathbf{F}_C = \begin{bmatrix} f_1 - f_0 \\ f_{-1} - f_0 \\ f_2 - f_0 \\ f_{-2} - f_0 \\ \vdots \\ f_n - f_0 \\ f_{-n} - f_0 \end{bmatrix} \quad \mathbf{D}_C = \begin{bmatrix} f_0^{(1)} \\ f_0^{(2)} \\ f_0^{(3)} \\ f_0^{(4)} \\ \vdots \\ f_0^{(2n-1)} \\ f_0^{(2n)} \end{bmatrix}$$

$$A_C = \begin{bmatrix} T & T^2/2! & T^3/3! & \dots & T^{2n}/2n! \\ -T & (-T)^2/2! & (-T)^3/3! & \dots & (-T)^{2n}/(2n)! \\ 2T & (2T)^2/2! & (2T)^3/3! & \dots & (2T)^{2n}/(2n)! \\ -2T & (-2T)^2/2! & (-2T)^3/3! & \dots & (-2T)^{2n}/(2n)! \\ \vdots & \vdots & \vdots & \vdots & \vdots \\ nT & (nT)^2/2! & (-nT)^3/3! & \dots & (nT)^{2n}/(2n)! \\ -nT & (-nT)^2/2! & (-nT)^3/3! & \dots & (-nT)^{2n}/(2n)! \end{bmatrix} \quad (4.18)$$

and \mathbf{r} is a vector of length $2N$ representing the remainder terms, each of which is of the order T^{2N+1} , and contains derivatives of the function of order greater than $2N$ at $t = 0$. For smaller values of T this terms is negligible.

Digital differentiators are introduced in our approach to derive higher order range-dynamics (e.g., range-rate, range-rate change, and so on) using the single-difference (between receivers connected with a common external oscillator) carrier-phase observations. These higher-order range dynamics will be used in Equation 4.6 to substitute the integrated slant range in the most accurate possible way.

By solving the matrix Equation 4.18, it is possible to obtain tap coefficients for several-order differentiators. It was demonstrated [Khan *et al.*, 1999] that the coefficients of the maximally linear digital differentiator of order $2N + 1$ are the same as the coefficients of a central difference approximation of order N . For example, the tap coefficients $d_k^{(p)}$ for a second-order differentiator (i.e., $p=2$) used to obtain range-accelerations are given by:

$$d_k^{(2)} = \frac{2!(-1)^{k+1} N!^2}{k^2 (N-k)!(N+k)!}, \quad k = \pm 1, \dots, \pm N \quad (4.19)$$

and

$$d_0^{(2)} = -\sum_{k=1}^N d_k^{(2)} \quad (4.20)$$

is the tap coefficient for the central point. Thus the central difference approximation of the second-order derivative for the arbitrary order of $2N$ can be written as:

$$f_i^{(2)} = \frac{1}{T^2} \sum_{k=0}^N d_k^{(2)} f_{k+i} + O(T^N) \quad (4.21)$$

where again T is the data sample interval, f_{k+i} is the measurement time series, and $O(T^N)$ is the remainder.

Another advantage of the central difference approximation is that within a certain maximum allowable ripple on amplitude response of the resultant differentiator, its pass-band can be dramatically increased. Multipath in kinematic scenarios should be treated as a high-frequency correlated scattered signal (due to the fast changing multipath environment and reflectors characteristics) and therefore the central difference approximation should allow for the passing of these high frequencies.

This means that when the GNSS-based platform performs multiple manoeuvres the antennas acceleration can change considerably in a short time-span. Therefore, the system should be able to track these differences, that is, it must track the platform jerk (acceleration time-difference). This is possible through the application of a third-order differentiator to obtain range-jerks ($\Delta\ddot{\Phi}_{r,s}^{pm}$). Their tap coefficients are given by:

$$d_k^{(3)} = \frac{3!(-1)^k N!^2}{k(N-k)!(N+k)!} \sum_{\substack{i=1 \\ i \neq |k|}}^N \frac{1}{i^2}, \quad k = \pm 1, \dots, \pm N \quad (4.22)$$

The optimal filter order choice is a very sensitive issue when the goal is to make MIMICS a useful algorithm in practical applications. Orders of $N > 20$ would be more accurate as seen from Figure 4.10, however there should be a compromise between the achievable accuracy, processing time (latency), and receiver memory allocation.

Therefore in order to estimate the optimal filter order (so that we can remove carrier-phase bias, and yet “track” as much as possible the platform dynamics) the residuals of velocity and acceleration estimates between the antennas are assessed in our approach. We calculate precise kinematic velocities and accelerations (in the position domain) in order to derive, on a second-stage, accurate range-rates, and range-rate change (in the measurement domain) to be used in equation 4.6.

4.5 Carrier-Phase Based Kinematic Velocity and Acceleration Estimation

The estimation of velocity and acceleration using GPS is based on the differentiation of the carrier-phase measurements or the receiver-generated Doppler measurements.

Considering the level of noise, it is preferable to generate velocity and acceleration measurements from the differentiation of the carrier-phase rather than from the instantaneous Doppler measurement (which is noisier). For velocity estimation we need to obtain range-rates while we need range-rate change (range-acceleration) for the estimation of acceleration.

The optimal design of a differentiator is the key point for an accurate velocity and acceleration estimate from the carrier-phase measurements, which should make a compromise between the noise level reduction, thus the accuracy that can be achievable, and the spectral resolution of the differentiated signal (band-width), because the differentiation method may be aliased the platform dynamics information's contained in the resulted signal. Since this choice depends on the particular platform dynamics, we have investigated different test scenarios and platforms in real-time environments.

Previous studies on GPS velocity determination [Van Graas and Soloviev, 2003; Ryan *et al.*, 1997] show that it is possible to achieve accuracies of a few millimetres per second depending on receiver quality, whether in static or kinematic mode, stand-alone or relative mode, and the particular dynamics situation. The velocity of the receiver

mounted on a moving platform can be determined by using the carrier-phase-derived *Doppler* measurements or the receiver generated *Doppler* measurements.

A receiver-generated *Doppler* measurement is a measure of instantaneous velocity, whereas the carrier-phase-derived *Doppler* is a measure of mean velocity between observation epochs. The *Doppler* measurement is noisier than carrier-phase-derived *Doppler* because the receiver-generated *Doppler* is measured over a very small time interval. As carrier-phase-derived *Doppler* is computed over a longer time span than *Doppler*, the random noise is averaged and lowered. Therefore, very smooth velocity is obtained by carrier-phase-derived *Doppler* observation if there is no undetected cycle slips.

The carrier-phase-derived *Doppler* can be obtained by either differencing carrier phase observations in the time domain, normalizing them with the time interval of the differenced observations or by fitting a curve using polynomials of various orders with successive phase measurements (delta-ranges).

By extending this approach of the differentiation on the measurement domain, it is also possible to estimate GNSS-based kinematic accelerations, determined by differentiating range rates with respect to time to determine the line of sight range-rate change. Actually, one is differentiating twice in cascade the raw carrier-phase measurements, to obtain the range-rate change. As a simple example just for a first-order differentiation (thus applicable for a static receiver) we would obtain:

$$h = \frac{1}{2} [1 \quad 0 \quad -1]^T \quad (4.23)$$

which will result in the following differentiator for the carrier-phase range rate:

$$\dot{\Phi}(t) \approx \frac{\Phi(t + \Delta t) - \Phi(t - \Delta t)}{2\Delta t} \quad (4.24)$$

and for the carrier-phase range acceleration:

$$\ddot{\Phi}(t) \approx \frac{\dot{\Phi}(t + \Delta t) - \dot{\Phi}(t - \Delta t)}{2\Delta t} = \frac{\Phi(t + \Delta t) - 2\Phi(t - \Delta t) + \Phi(t - 3\Delta t)}{4\Delta t^2} \quad (4.25)$$

The advantage of this approximation is simplicity. As was demonstrated by [Szarmes *et al.*, 1997], the use of the first order central difference approximation of the carrier-phase observations to generate the *Doppler* observations is easy to implement and provides the most appropriate velocity estimates in low dynamics environments. The same approach can be applied for estimating acceleration.

The trade-off is that the approximation cannot reflect quite well the receiver dynamics in kinematic situations with unknown dynamics. The first order central difference approximation is a linear prediction of the Doppler shift, which corresponds to a band-pass filter with cut-off frequencies at 0.125 and 0.375 Hz. The cut-off frequency of the

filter is determined at the frequency where the amplitude reaches around 70% (i.e., $1/\sqrt{2}$) of the maximum amplitude.

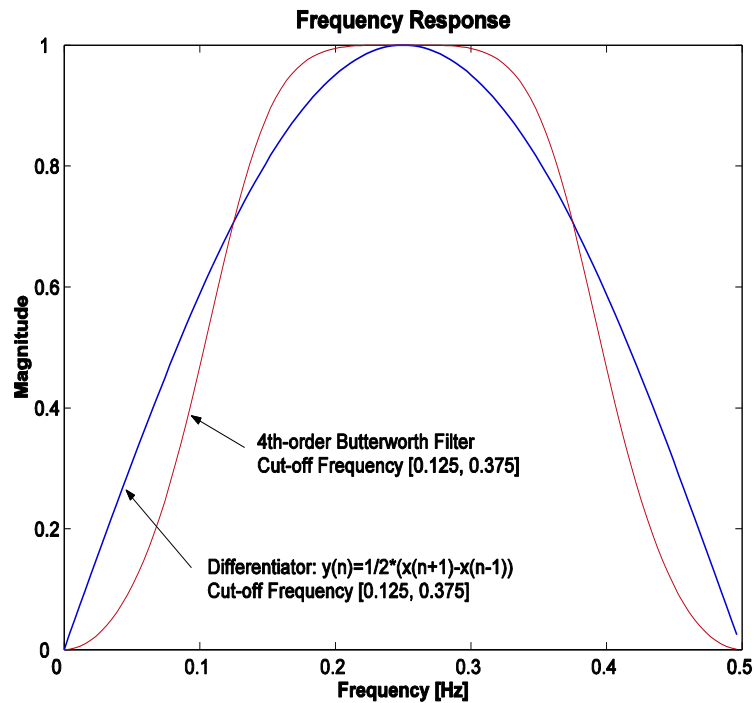


Figure 4.11: Frequency response of the filter to the amplitude at a 1 Hz sampling rate.

The fourth-order Butterworth filter with cut-off frequencies at 0.125 and 0.375 Hz is also plotted in the figure as an example of the conventional band-pass filters, which have more or less similar frequency responses

As is illustrated in Figure 4.11, the filter of the first order central difference approximation stops the signals at 0 and 0.5 Hz (i.e., *Nyquist* frequency). At a half of the *Nyquist* frequency (0.25 Hz), this filter passes the signals without filtering. Therefore, this filter can perfectly remove constant biases in the signals.

However, this filter will reduce the amplitudes of the signals over all frequency components except for a half of the *Nyquist* frequency. If we carry out a kinematic test at a 1 Hz data rate, the higher-order effects (e.g., all frequency components higher than the *Nyquist* frequency, 0.5 Hz) of the receiver dynamics will be aliased in the approximation of the carrier phase [Ifeachor and Jervis, 1993].

The first step of our approach to determine the precise platform antennas velocities and accelerations is to compute the satellite velocities and accelerations in real time, i.e. from the broadcast ephemerides. Until now, it is not very common to see works on this subject, probably because when one wants acceleration information in real time it is easier to get those very precise (in a short term) from accelerometres, or for other applications, a post-processing procedure using precise ephemerides is adopted.

However, if we can prove that satellite velocities and accelerations can be estimated at the order of mm/s and mm/s² respectively using broadcast ephemerides by properly modeling the other error sources, it is reasonable to assume that one can also estimate in real time user velocities and accelerations with the same order of magnitude. This proof comes from solid concepts on satellite dynamics and the close relationship between the satellite orbital broadcast parameters and their differentiation in time to obtain not only satellite velocities and acceleration in the orbital plane but also in the Earth-Centre-Earth-Fixed (ECEF) reference frame. The next figures and explanations come from [Kennedy, 2002], and are very well detailed and explained.

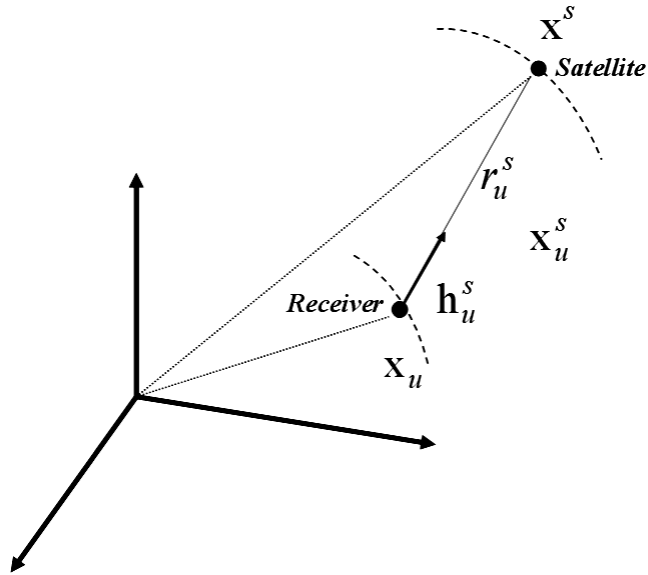


Figure 4.12: Line-of-sight relative geometry between satellite and user

$$\mathbf{x}_u^s = r_u^s \cdot \mathbf{h}_u^s \quad (4.26)$$

- \mathbf{x}_u^s is the relative position vector between the user u and the satellite s .
- r_u^s is the geometric range between the user and the satellite.
- \mathbf{h}_u^s is the unit direction vector between the user and the satellite.

A more useful way of seeing Equation 4.26 is putting it in view point of the geometric distance, that is:

$$r_u^s = \mathbf{h}_u^s \cdot \mathbf{x}_u^s \quad (4.27)$$

By differentiating Eq. (4.27), one obtains the geometric range rate:

$$\begin{aligned}\dot{r}_u^s &= \dot{\mathbf{h}}_u^s \cdot \mathbf{x}_u^s + \mathbf{h}_u^s \cdot \dot{\mathbf{x}}_u^s \\ &= \mathbf{h}_u^s \cdot \dot{\mathbf{x}}_u^s \quad (\because \dot{\mathbf{h}}_u^s \perp \mathbf{x}_u^s \Rightarrow \dot{\mathbf{h}}_u^s \cdot \mathbf{x}_u^s = 0)\end{aligned}\tag{4.28}$$

and by differentiating Equation 4.27 two times, one obtain the geometric range-acceleration between the user u and the satellite s :

$$\ddot{r}_u^s = \mathbf{h}_u^s \cdot \ddot{\mathbf{x}}_u^s + \dot{\mathbf{h}}_u^s \cdot \dot{\mathbf{x}}_u^s\tag{4.29}$$

where their two components (radial and tangential) can be seen in the next figure:

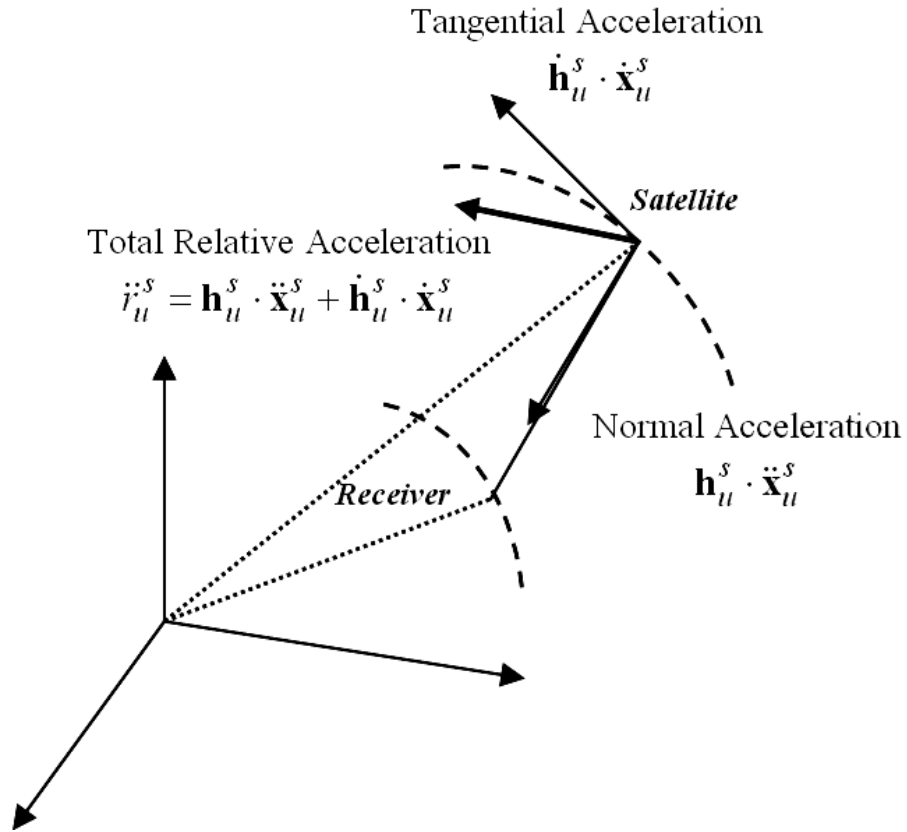


Figure 4.13: Mechanics of satellite acceleration

The two quantities \dot{r}_u^s and \ddot{r}_u^s , are respectively the true geometric range-rate and range-rate change, which can be approximated by the differentiation of the carrier-phase in time, as explained before.

The satellite velocities are obtained through an analytical differentiation in time of the ECEF parameter equations (ICD-GPS-200C):

$$\dot{x}_k = \frac{\delta x_k}{\delta t} \quad \dot{y}_k = \frac{\delta y_k}{\delta t} \quad \dot{z}_k = \frac{\delta z_k}{\delta t} \quad (4.30)$$

and accelerations:

$$\ddot{x}_k = \frac{\delta^2 x_k}{\delta t^2} \quad \ddot{y}_k = \frac{\delta^2 y_k}{\delta t^2} \quad \ddot{z}_k = \frac{\delta^2 z_k}{\delta t^2} \quad (4.31)$$

where these ECEF coordinates are given by:

$$\begin{aligned} x_k &= x'_k \cos \Omega_k - y'_k \cos i_k \sin \Omega_k \\ y_k &= x'_k \sin \Omega_k + y'_k \cos i_k \cos \Omega_k \\ z_k &= y'_k \sin \Omega_k \end{aligned} \quad (4.32)$$

and the orbital plane coordinates are:

$$\begin{aligned} x'_k &= r_k \cos u_k \\ y'_k &= r_k \sin u_k \end{aligned} \quad (4.33)$$

and Ω_k is the corrected longitude of ascending node:

$$\Omega_k = \Omega_0 + (\dot{\Omega} - \dot{\Omega}_e)t_k - \dot{\Omega}_e t_{oe} \quad (4.34)$$

and r_k , i_k , and u_k are, respectively, the corrected radius, corrected inclination, and corrected argument of latitude.

Another way to see it is through a differentiation in time of the orbital plane coordinates and the differentiation of the rotation matrices, to convert the orbital plane coordinates to ECEF. Both methods give identical results, as one can see from next equation:

$$\ddot{\mathbf{x}}^s = \begin{pmatrix} \ddot{x}_k \\ \ddot{y}_k \\ \ddot{z}_k \end{pmatrix} = \ddot{\mathbf{R}} \begin{pmatrix} x'_k \\ y'_k \\ 0 \end{pmatrix} + 2\dot{\mathbf{R}} \begin{pmatrix} \frac{\delta x'_k}{\delta t} \\ \frac{\delta y'_k}{\delta t} \\ 0 \end{pmatrix} + \mathbf{R} \begin{pmatrix} \frac{\delta^2 x'_k}{\delta t^2} \\ \frac{\delta^2 y'_k}{\delta t^2} \\ 0 \end{pmatrix} \quad (4.35)$$

where \mathbf{R} is given by:

$$\mathbf{R} = \mathbf{R}_3 \{-\Omega_k\} \mathbf{R}_1 \{-i_k\} \mathbf{R}_3 \{-\omega_k\} = \begin{bmatrix} \cos \Omega_k \cos \omega_k & \cos \Omega_k \sin \omega_k & \sin \Omega_k \sin i_k \\ -\sin \Omega_k \sin \omega_k \cos i_k & -\sin \Omega_k \cos \omega_k \cos i_k & -\cos \Omega_k \sin i_k \\ \sin \Omega_k \cos \omega_k & -\sin \Omega_k \sin \omega_k & \cos i_k \\ +\cos \Omega_k \sin \omega_k \cos i_k & +\cos \Omega_k \cos \omega_k \cos i_k & \\ \sin \omega_k \sin i_k & \cos \omega_k \sin i_k & \end{bmatrix} \quad (4.36)$$

Here we only depict the derivation of the satellite accelerations, as this is a more complex operation (however the same method is applied for the velocities). After the derivation of the satellite velocities and accelerations from the broadcast ephemeris, one can validate them comparing with those derived from a NGA (National Geo-Spatial Agency - <http://earth-info.nga.mil/GandG/sathtml/> - accessed as of February, 2013) SP3 file which contains precise positions and velocities. This can be done using a 9th order

Lagrange interpolating polynomial and generate solutions with the rate that best fits one purposes:

$$L_j(x) = \prod_{\substack{k=0 \\ k \neq j}}^n \frac{(x - x_k)}{(x_j - x_k)} \quad (4.37)$$

and the polynomial:

$$P(x) = \sum_{j=0}^n f(x_j) L_j(x) \quad (4.38)$$

As for the accelerations, since the SP3 file does not contain them, it is easier to use the interpolated velocities and through numerical differentiation obtain them. Our choice was again a first order central difference approximation using a *Taylor's* expansion, which can also shed some light on the error involved in using the approximation:

$$f'(x) = \frac{f(x+h) - f(x-h)}{2h} - \frac{f'''(\zeta)}{6} h^2 \quad (4.39)$$

Figure 4.14 shows the differences of the velocity and acceleration estimates using the broadcast ephemeris and the SP3 precise ephemeris. One can see a proof that the satellite velocity and acceleration predicted by using the broadcast ephemeris in the navigation message is sufficiently accurate.

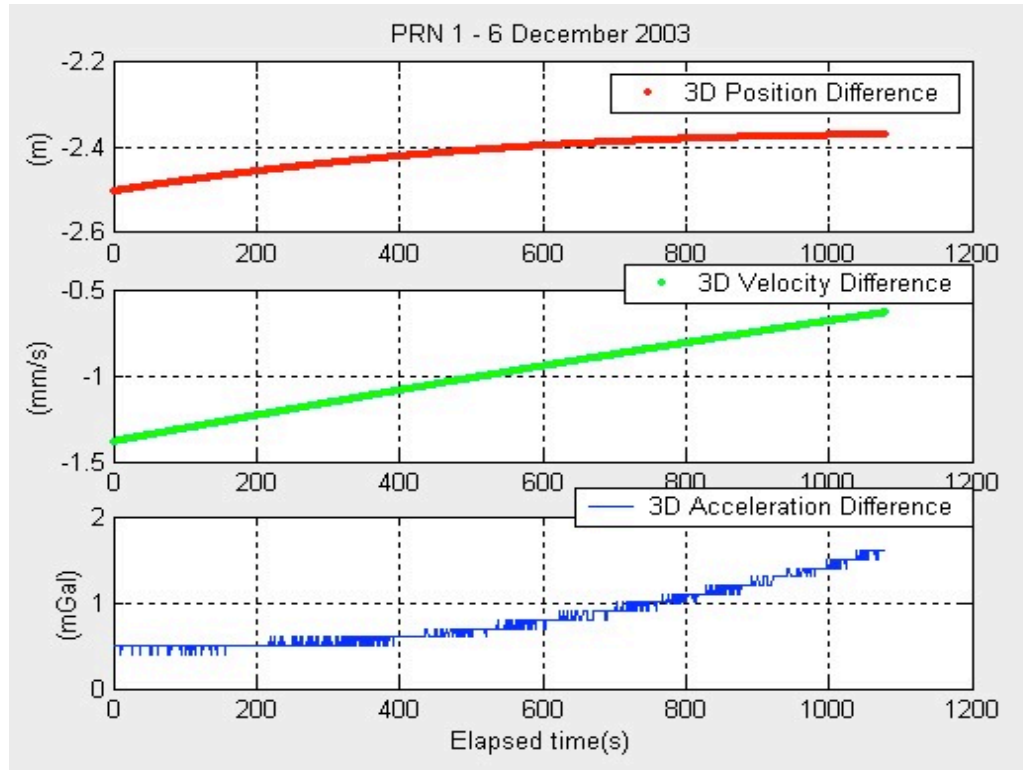


Figure 4.14: Satellite velocity and acceleration accuracy assessment using broadcast ephemeris

Before giving the mathematics behind the observables, it is important to understand that although the position solutions are relaxed in the carrier-phase method, their precise determination is nonetheless important to the precise determination of velocity and acceleration. At least, positioning accuracy of DGPS, *i.e.*, 10 m, is required for the errors caused by the wrong coordinates to be negligible [Itani et al. 2000]. An error of 10m in the position could provide the velocity estimation with negligible deviation. In this case, errors were absorbed in the least-squares solution and we obtained a noisier solution with an error of few mm/s.

At this point, one is ready to see the relationship between the true geometric range-rate \dot{r}_u^s and the range-rate derived from the carrier-phase differentiation in time $\dot{\Phi}_u^s$. The same can be extended for the geometric range-rate change \ddot{r}_u^s and the derived range-rate change $\ddot{\Phi}_u^s$. Equation 4.40 shows the observation equation for the velocity determination.

$$\begin{aligned}\dot{\Phi}_u^s &= \dot{r}_u^s + (\dot{B} - \dot{b}) + \dot{I}_u^s + \dot{T}_u^s + \delta V^s + \dot{\xi} \\ \dot{\Phi}_u^s &= \dot{r}_u^s + \dot{B} + \varepsilon_{u_{\dot{\Phi}}}^s\end{aligned}\quad (4.40)$$

where \dot{r}_u^s stands for the geometric-range rate between the receiver u and satellite s , \dot{B}_u for the receiver clock drift, \dot{b}^s for the satellite clock drift, \dot{I} for the ionospheric delay rate, \dot{T} for the tropospheric delay rate, δV^s the error in satellite velocity derivation, and $\dot{\xi}$ for the receiver system noise. For the range-acceleration, the same can be applied:

$$\begin{aligned}\ddot{\Phi}_u^s &= \ddot{r}_u^s + (\ddot{B} - \ddot{b}) + \ddot{I}_u^s + \ddot{T}_u^s + \delta A^s + \ddot{\xi} \\ \ddot{\Phi}_u^s &= \ddot{r}_u^s + \ddot{B} + \varepsilon_{u_{\ddot{\Phi}}}^s\end{aligned}\quad (4.41)$$

Through all the modeled quantities in the equation are of a 2nd order, and δA^s is the error in satellite acceleration calculation.

Since one use the pseudo-range measurements for the position solutions and the carrier-phase for deriving range-rates and range-rate change, we model out some of the errors in

the raw observations. For the carrier-phase, they are the errors in satellite clock, propagation effects in the ionosphere and troposphere, and receiver system noise, which can be summarised as in equation 4.42:

$$\begin{aligned}\mathcal{E}_{u\phi}^s &= -\dot{b}^s + \dot{I}_u^s + \dot{T}_u^s + \delta V^s + \dot{\xi} \\ \mathcal{E}_{u\phi}^s &= -\ddot{b}^s + \ddot{I}_u^s + \ddot{T}_u^s + \delta A^s + \ddot{\xi}\end{aligned}\tag{4.42}$$

The effects of satellite clock bias and drift were modeled out using the coefficients in the navigation message [ICD-GPS-200, 1999]. The relativistic effect and group delay differential are also accounted for using appropriate algorithms with values given in the navigation message.

To reduce the effect of the tropospheric delay in the measurements, we use the UNB3 tropospheric prediction model [Collins and Langley, 1997], which is based on the zenith delay algorithms of Saastamoinen [1973], the mapping functions of Niell [1996], and a table of sea-level atmospheric values derived from the U.S. 1966 Standard Atmosphere Supplements, and lapse rates to scale the sea-level values to the receiver height.

For reducing the effects of ionospheric delay, we use the standard Klobuchar model [Klobuchar, 1987], using the parameter values in the navigation message. Since we use the time-differenced measurements over a short time interval (that is, less than or equal to 2 seconds) for velocity and acceleration determination, the residual effects of the tropospheric and ionospheric delays, if any, are normally negligible. After modeling

accordingly the measurements, the observation equations for velocity and acceleration are now given by:

$$\begin{aligned}\dot{\Phi}_u^s &= \mathbf{h}_u^s \cdot (\mathbf{v}_u - \mathbf{V}^s) + \dot{B}_u + \varepsilon_{u\phi}^s \\ \ddot{\Phi}_u^s &= \dot{\mathbf{h}}_u^s \cdot (\mathbf{v}_u - \mathbf{V}^s) + \mathbf{h}_u^s \cdot (\mathbf{a}_u - \mathbf{A}^s) + \ddot{B}_u + \varepsilon_{u\phi}^s\end{aligned}\tag{4.43}$$

where one can see explicitly the relation between the derived observations through differentiation, and those from equation (4.27) and (4.28), that is:

$$\begin{aligned}\dot{r}_u^s &= \mathbf{h}_u^s \dot{\mathbf{x}}_u^s \\ \ddot{r}_u^s &= \dot{\mathbf{h}}_u^s \cdot \ddot{\mathbf{x}}_u^s + \mathbf{h}_u^s \cdot \dot{\mathbf{x}}_u^s\end{aligned}$$

where \mathbf{V}^s and \mathbf{A}^s stand for the satellite velocity and acceleration vectors, \mathbf{v}_u and \mathbf{a}_u for the receiver velocity and acceleration vectors, and \mathbf{h} represents the directional cosine vector between the receiver and satellite. Hence, it is easier to describe the unknown parameters for both the velocity and acceleration, in the least-squares sense:

$$\hat{\mathbf{x}}_v = [v_x \quad v_y \quad v_z \quad \dot{B}_u]^T \text{ and } \hat{\mathbf{x}}_a = [a_x \quad a_y \quad a_z \quad \ddot{B}_u]^T \quad . \tag{4.44}$$

5 Adaptive Estimation Using Auto-Regressive Models

5.1 Auto-Regressive (AR) Adaptive Estimation

Up to now we have assumed that the AR model parameters are known a priori. In practical applications (i.e. real-time), however, these parameters must be estimated from noisy observations. Therefore, the key point for the performance of our multipath signal enhancement system is the estimation of AR parameters in the presence of colored noise.

The AR parameters are estimated using an iterative procedure, i.e. filtering of signal block and parameter estimation is alternated several times. Obviously, this approach results in a high computational complexity even when implementing using high-level languages such as C/C++.

The adaptive *Kalman* filter used in our enhancement system is based on the adaptive setup as shown in Figure 5.1, and may be designed to suppress combinations of colored noise and impulsive noise. The enhanced signal at the output of the *Kalman* filter is fed to the AR parameter estimation subsystem. At the beginning of the system's convergence period the colored noisy signal (that is, the time-differenced single-difference multipath measurements) is used for AR parameter estimation.

Convergence of this system is ensured as long as the AR signal contains signal components that are stronger than the disturbing noise. Due to the feedback loop the parameter estimation of the AR signal is further improved.

The system requires a minimum of *a priori* knowledge of signal and noise parameters (that's why we can input approximate multipath reflector characteristics in any environment) and is capable of tracking short-time stationary signals as is usual in high multipath-reflective and diffractive scenarios.

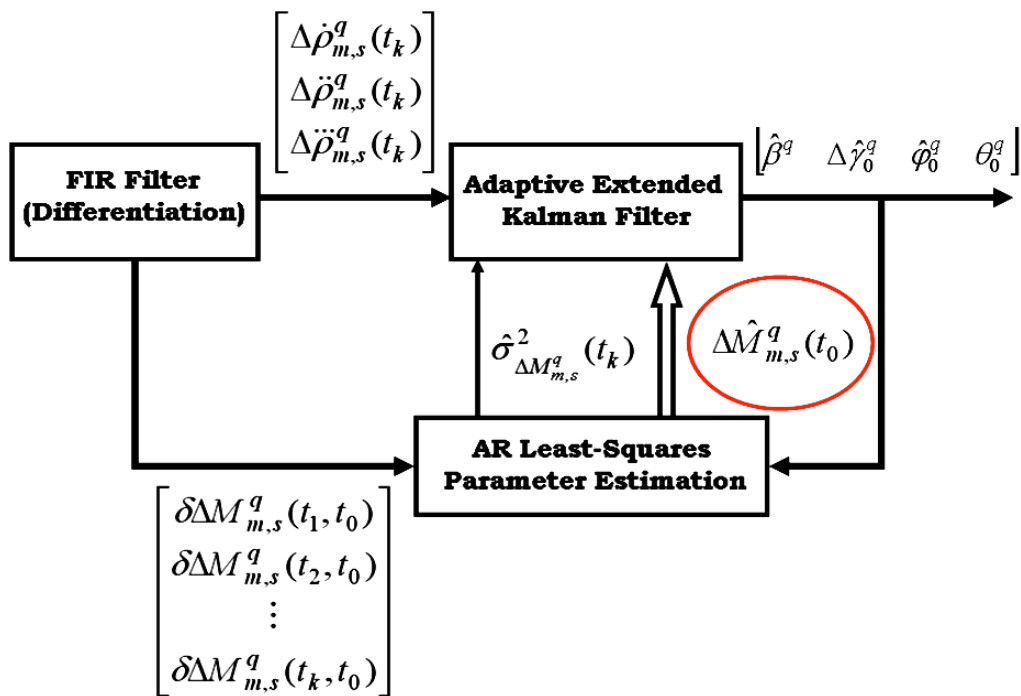


Figure 5.1: MIMICS algorithm flow-chart (the initial steps of multi-antenna carrier-phase handling, and pre-processing are not depicted)

At the first stage to derive single-difference multipath at the initial epoch, $\Delta M_{m,s}^{prn}(t_0)$, mechanical and mathematical randomization of the single-difference multipath observables is performed in our approach. A time series of the single-difference multipath observables to be randomized is given as:

$$\delta\Delta M_{m,s}^{prn}(t_1, t_0), \delta\Delta M_{m,s}^{prn}(t_2, t_0), \dots, \delta\Delta M_{m,s}^{prn}(t_n, t_0) \quad (5.1)$$

Then our goal is to achieve the following condition, which enables us to isolate the initial single-difference multipath bias (if there is no loss-of-lock so that we can guarantee continuity), as:

$$\mathbb{E}[\Delta M_{m,s}^{prn}(t_0)] = 0 \quad (5.2)$$

where $\mathbb{E}[\bullet]$ is the expectation operator. Obviously this equation will equal zero only if multipath behaves truly as a random stochastic process (thus a white-noise stochastic process).

Although multipath in a kinematic scenario tends to be more or less random, its temporal correlation should not be ignored in our approach. To guarantee random multipath, instead, our approach tries to de-correlate the between-antenna relative multipath through the introduction of a pseudo-random motion. As one cannot completely rely only on a mechanical de-correlation through the platform calibration motion, one also has to do it through the mathematical “whitening” of the time-series.

White noise is defined as a stationary random process whose power spectral density function is constant. That is, it contains all frequencies of equal amplitude. If the constant spectral amplitude is A , then the corresponding autocorrelation function is given by the inverse Fourier transform of a constant, which is the *Dirac delta* $\delta(\tau)$ (τ is the time-lag):

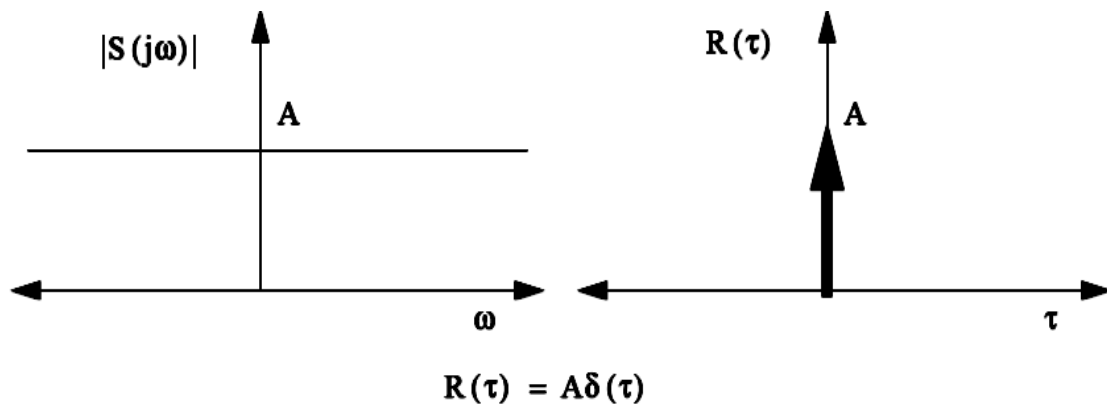


Figure 5.2: White noise model, power-spectral density functional (left), and auto-correlation function (right)

The white noise model is unbiased, that is, have zero mean for all time, and thus it is exactly what we sought to obtain an unbiased estimate of the initial single-difference multipath from the (colored) noisy time-difference multipath observables.

However this model (Figure 5.2) is a mathematical idealization (or abstraction) since white noise cannot really occur in nature because it requires infinite energy. Nevertheless

white noise model processes can be mapped onto variance, co-variance and auto-correlation functions of stochastic random processes, which are easier to implement algorithmically.

The ensemble of data given in Equation 5.1 can be modeled as an oscillatory random process, for which second or higher-order auto-regressive (AR) models can provide more realistic modeling in kinematic scenarios.

We estimate the parameters of this model in real time, in a block-by-block analysis using the *Yule-Walker* equations [Park, 2004]. A whitening filter can then be formed from the estimated parameters. An auto-regressive process is one represented by a difference equation of the form:

$$\hat{x}(n) = \sum_{i=1}^p \theta_{p,i} x(n-i) + e(n) \quad (5.3)$$

where $x(n)$ is the real random-sequence, $\theta_{p,i}$ and $\theta_{p,p} \neq 0$ are parameters, where p is the order of the AR model (for instances, $p=1$ corresponds a 1st-order *Gauss-Markov* model), and $e(n)$ is a sequence of independent and identically distributed zero-mean Gaussian random variables, that is:

$$\begin{aligned} E[e(n)] &= 0 \\ E[e(n)e(j)] &= \begin{cases} \sigma_n^2, & n = j \\ 0, & n \neq j \end{cases} \end{aligned} \quad (5.4)$$

The sequence $e(n)$ is called white *Gaussian* noise. Thus an autoregressive process is simply another name for a linear difference equation model where the input or forcing function is white Gaussian noise.

The prediction is forward in the sense that the estimate at time index n is based on p samples indexed earlier in time. The complex forward linear prediction error is given as:

$$e^f(n) = x(n) - \hat{x}(n) = x(n) - \sum_{i=1}^p \theta_{p,i} x(n-i) \quad (5.5)$$

and its functional representation is given by the flow-chart depicted in Figure 5.3, that is:

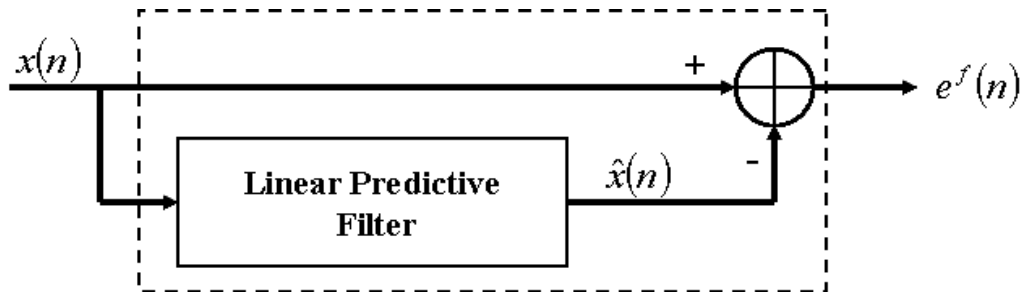


Figure 5.3: Flow-chart of a linear prediction function

where the superscript f is used here to denote that this is a forward estimate. Equation 5.3 can be easily reduced to a state model of the form:

$$X(n) = \Theta \cdot X(n-1) + E(n) \quad (5.6)$$

which is more easily applied to real-time processing algorithms. The AR coefficients vector can be obtained through:

$$\mathbf{r}_{XX} = \mathbf{R} \cdot \Theta \quad (5.7)$$

where \mathbf{R} is the correlation coefficient matrix, \mathbf{r}_{XX} is the auto-correlation coefficient vector, and Θ is the auto-regressive coefficient vector. This vector-matrix equation is called the *Yule-Walker* equation. More important, because \mathbf{R} is invertible, we can obtain:

$$\Theta = \mathbf{R}^{-1} \mathbf{r}_{XX} \quad (5.8)$$

where the scalar auto-correlation function r_{XX} for a random process $x(t)$ is defined as:

$$r_{XX}(t_1, t_2) = E[x(t_1), x(t_2)] = \int_{-\infty}^{+\infty} \int_{-\infty}^{+\infty} x_1 x_2 f(x_1, x_2) dx_1 dx_2 \quad (5.9)$$

where $f(x_1, x_2)$ is the joint probability distribution. Therefore Equation 5.9 can be used to estimate the parameters $\theta_{p,i}$ of the model. In general Equation 5.7 has the following matrix form:

$$\begin{bmatrix} r_{XX}(1) \\ r_{XX}(2) \\ \vdots \\ r_{XX}(p) \end{bmatrix} = \begin{bmatrix} 1 & r_{XX}(1) & r_{XX}(2) & \cdots & r_{XX}(p-1) \\ r_{XX}(1) & 1 & r_{XX}(1) & \cdots & r_{XX}(p-2) \\ \vdots & \vdots & \vdots & \vdots & \vdots \\ r_{XX}(p-1) & \cdots & \cdots & \cdots & 1 \end{bmatrix} \begin{bmatrix} \theta_{p,1} \\ \theta_{p,2} \\ \vdots \\ \theta_{p,p} \end{bmatrix} \quad (5.10)$$

Therefore one can estimate the parameters $\theta_{p,i}$ using the usual linear weighted least-squares solution equation:

$$\hat{\mathbf{x}}_k = (\hat{\mathbf{A}}_k \mathbf{C}_{l_k}^{-1} \mathbf{A}_k)^T \mathbf{A}_k^T \mathbf{C}_{l_k}^{-1} \mathbf{l}_k \quad (5.11)$$

Where $\mathbf{C}_{l_k}^{-1}$ is the weight matrix, that is, the inverse of the observations covariance-matrix, and can be given by the standard-deviation of the auto-correlation estimates r_{XX} . The other terms in Equation 5.11 are given by:

$$\mathbf{l}_k = \begin{bmatrix} r_{XX}(1) \\ r_{XX}(2) \\ \vdots \\ r_{XX}(p) \end{bmatrix} \quad \hat{\mathbf{A}}_k = \begin{bmatrix} 1 & r_{XX}(1) & r_{XX}(2) & \cdots & r_{XX}(p-1) \\ r_{XX}(1) & 1 & r_{XX}(1) & \cdots & r_{XX}(p-2) \\ \vdots & \vdots & \vdots & \vdots & \vdots \\ r_{XX}(p-1) & \cdots & \cdots & \cdots & 1 \end{bmatrix} \quad \hat{\mathbf{x}}_k = \begin{bmatrix} \theta_{p,1} \\ \theta_{p,2} \\ \vdots \\ \theta_{p,p} \end{bmatrix} \quad (5.12)$$

The *Yule-Walker* method constructs the Equation 5.6 by using the estimates of auto-correlation sequences from the sample data (in Equation 5.1), and by the minimization of the forward prediction error in the least-squares sense, and therefore it fits as whitening filtering method to real-time systems.

The selection of the model-order p of the $AR(p)$ “whitener” is a critical one as the determination of the order of stochastic models is unknown and needs to be estimated. That is, an order too low results in a poor whitener of the background coloured noise, while an order too large might affect the embedded original signal, which we are interested in detecting.

Since the order of the coefficients estimation depends on the multipath spectra (dependent on the platform dynamics and reflector distance), we use in MIMICS a cost-function to estimate in real-time the proper order. The order was set to vary between one (a *Gauss-Markov* model) and five. For instances, in the case when $p = 2$ (second-order autoregressive model), $X(n)$ is given by:

$$X(n) = \theta_{2,1}X(n-1) + \theta_{2,2}X(n-2) + e(n) \quad (5.13)$$

Where

$$\theta_{2,1} = \frac{r_{XX}(1)[r_{XX}(0) - r_{XX}(2)]}{[r_{XX}(0)]^2 - [r_{XX}(1)]^2} \quad (5.14)$$

And

$$\theta_{2,2} = \frac{r_{XX}(0)r_{XX}(2) - [r_{XX}(2)]^2}{[r_{XX}(0)]^2 - [r_{XX}(1)]^2} \quad (5.15)$$

The respective second-order cost function uses the residual sum of squared error, which can be used to estimate $\hat{\sigma}^2$, and is given by:

$$\hat{\sigma}^2 = \frac{1}{N-4} \left\{ \sum_{j=3}^N [X(j) - \hat{\theta}_{2,1}X(j-1) - \hat{\theta}_{2,2}X(j-2)]^2 \right\} \quad (5.16)$$

The order estimation that gives the lowest error is the one chosen, and this task is done iteratively until it reaches a minimum threshold value (given by the standard-deviation of the single-difference carrier-phase observable).

Once this stage is fulfilled the initial single-difference multipath observable can be easily obtained and fed to the *Kalman* filter. The next figure (Figure 5.4) illustrates the frequency of actual orders, coming from a real-live signal test scenario (using a vehicle as the dynamic platform, and overviewed in next chapter), determined based on the cost function given by Equation 5.16:

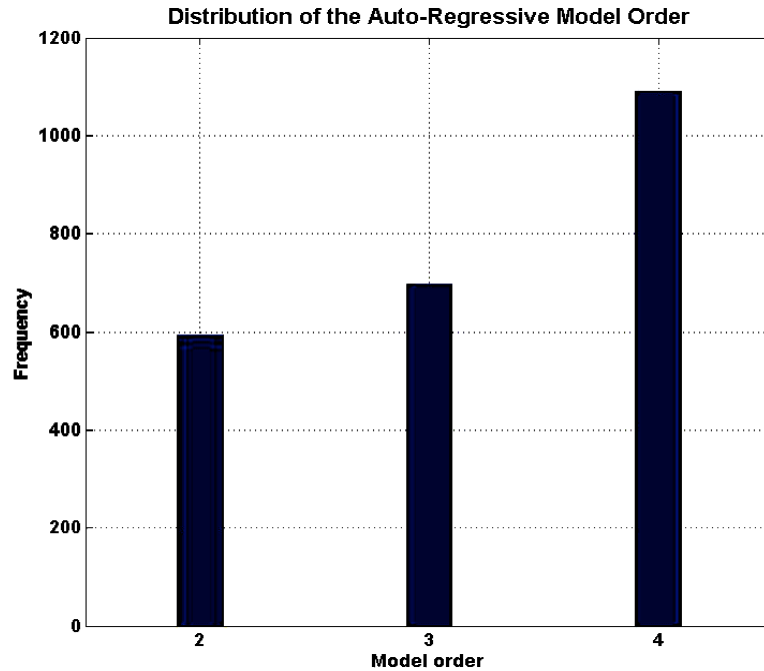


Figure 5.4: The distribution of the AR order models for the estimated multipath observables

A good example is given by a periodogram of the original time series (Figure 5.5) from one of the satellite signals observed in the aforementioned test scenario. It clearly shows strong temporal correlations and they mostly reflect the outcome of the raw carrier-phase differentiators to obtain the higher-order range dynamics (and possibly as well from time-correlated multipath signatures such as multipath fading).

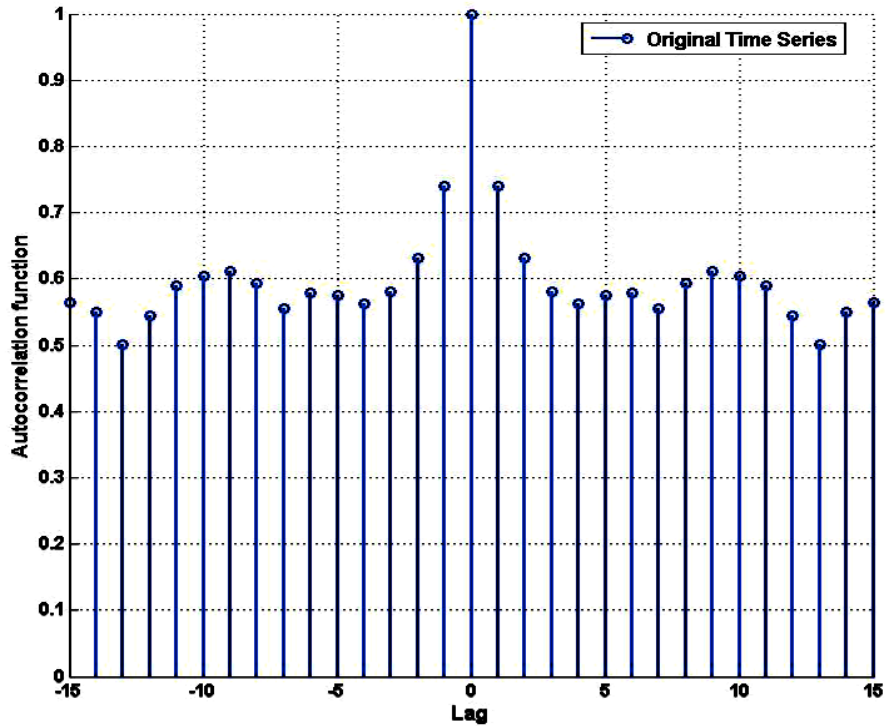


Figure 5.5: Periodogram of the original time series (used to generate a multipath observable)

After applying the *Yule-Walker* method to whiten the data, the operation described from previous equations can be applied on the coloured noisy correlated data and one can now see that the ensemble of time-differenced, single-difference multipath observables, that is, the residuals that represent a truly random stochastic process (Figure 5.6):

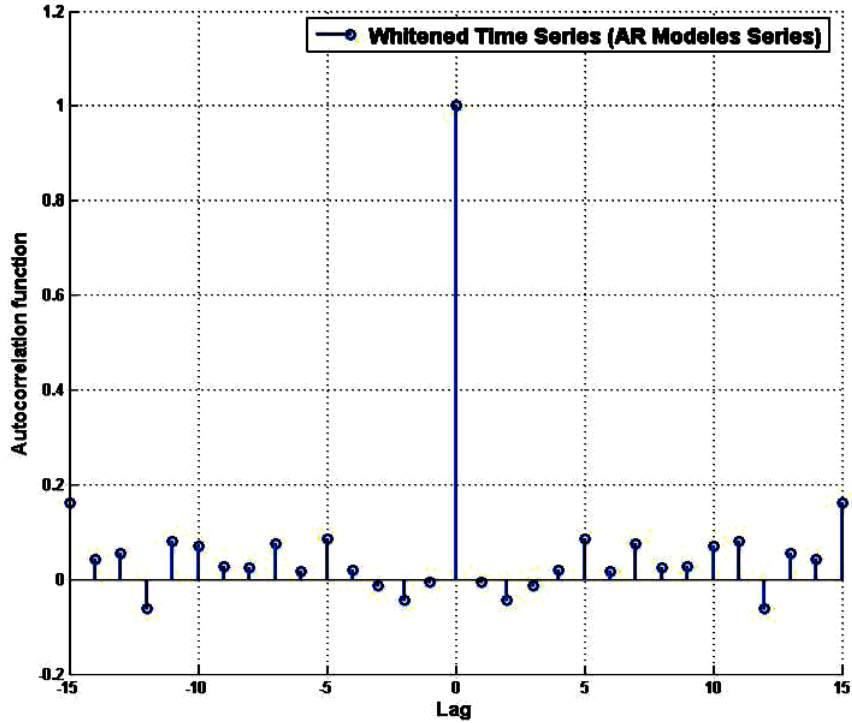


Figure 5.6: Periodogram of the whitened time series (used to generate the original multipath observable)

Then the combination of an initial mechanical calibration (dynamic platform forced random motion – see Figure 5.7), and the whitening signal processing technique mentioned before should be enough to derive the multipath observables.

This type of calibration is very common in the surveying and construction machine control business. Any experienced surveyor working with GNSS-RTK systems knows that moving the GNSS antenna (usually the pole) in a random fashion improves the initial ambiguity fixing.

On the other hand, construction machine (dozers, motor-graders, etc.) operators initialize their positioning and orientation systems by performing initial blade random motions, where the sensors are mounted.

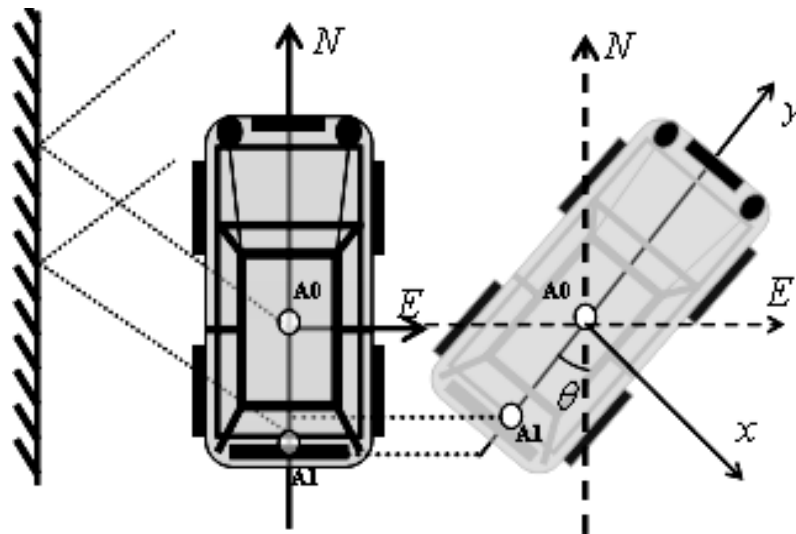


Figure 5.7: Dual-antenna system initial calibration, where the vehicle random vehicle motion causes a continuous variation in the between-antennas angle (θ), and thus leads to a multipath time-decorrelation

5.2 Kalman Filter Multipath Parameters Estimation

Once single-difference multipath observables are derived, on a satellite by satellite basis, it is possible to estimate the parameters (β composed term for reflection coefficient and correlation function - dampening factor, $\Delta\gamma_0$ phase-delay on master antenna, φ_0

azimuth of reflected signal, θ_0 elevation angle of reflected signal) of the multipath observable for each PRN (Figure 5.8):

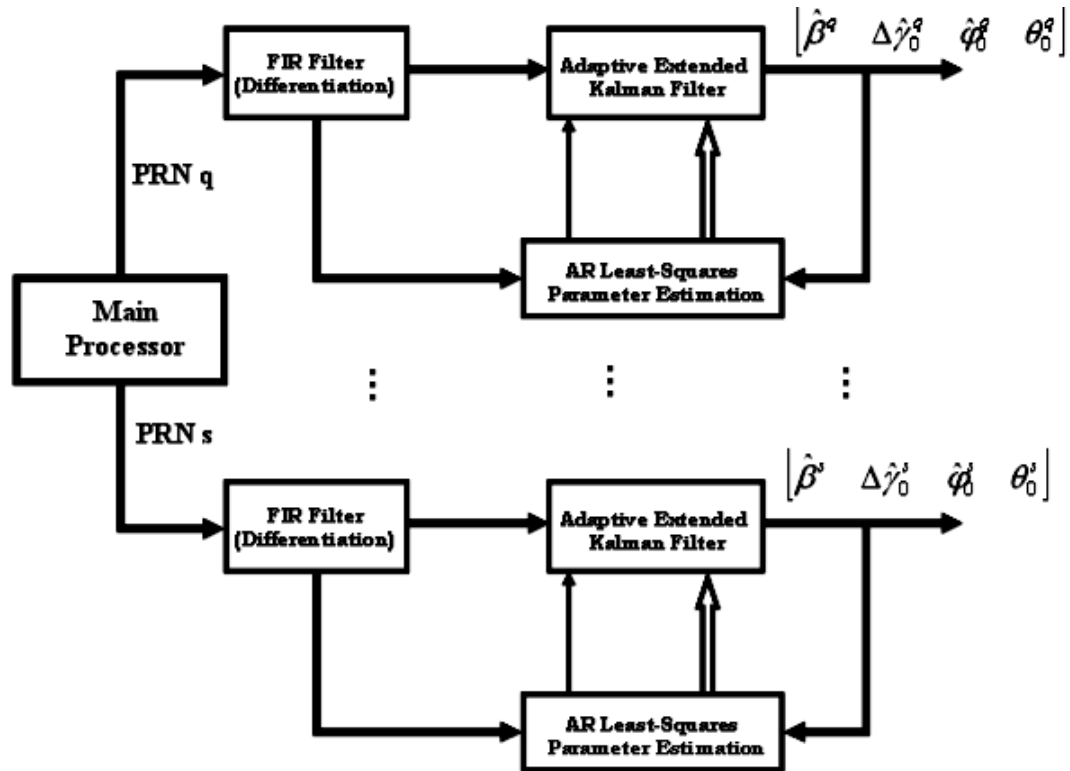


Figure 5.8: Multipath parameters estimation for each visible satellite (*per epoch and simultaneously*)

An Extended Kalman Filter (EKF) is applied, and the observation vector is formed by:

$$\hat{y}_k = \begin{bmatrix} \Delta\hat{M}_{a_0,a_1}^q(t_0) \\ \vdots \\ \Delta\hat{M}_{a_0,a_1}^q(t_n) \end{bmatrix} \quad (5.17)$$

where a_0 , and a_1 represent the master and slave antennas, respectively, and q refers to the satellite being modeled. n is the length of the data window used to form the observation vector for each epoch. This value can vary from 1 (hence, only one measurement update per epoch), to 10. Both have advantages and disadvantages. Using 10Hz as data update-rate it means that in 1 second the 10 measurements are able to capture the multipath properly for most kinematic applications.

The measurements are combined with the previous state estimate using the standard form as:

$$\hat{\mathbf{x}}_k^+ = \hat{\mathbf{x}}_k^- + \mathbf{K}_k \left[\mathbf{y}_k - \hat{\mathbf{h}}_k(\hat{\mathbf{x}}_k^-) \right] \quad (5.18)$$

$$\mathbf{P}_k^+ = (\mathbf{I} - \mathbf{K}_k \mathbf{H}_k) \mathbf{P}_k^- (\mathbf{I} - \mathbf{K}_k \mathbf{H}_k)^T + \mathbf{K}_k \hat{\mathbf{R}}_k \mathbf{K}_k^T$$

where $\mathbf{h}_k(\cdot)$ is the non-linear function relating the state to the measurement. The observation matrix in Equation 5.18 is the *Jacobian* matrix, given by Equation 5.19 (Note that the arrangement of this matrix reflects the use of the *Kalman* filter PVA – Position, Velocity, and Acceleration stochastic model):

The *Kalman* gain \mathbf{K}_k is determined by:

$$\mathbf{K}_k = \mathbf{P}_k^- \mathbf{H}_k^T (\mathbf{H}_k \mathbf{P}_k^- \mathbf{H}_k^T + \hat{\mathbf{R}}_k)^{-1} \quad (5.20)$$

where $\hat{\mathbf{R}}_k$ is the expected noise covariance. As the multipath observables are estimated from the whitened time series, their noise variance is also obtained straight-forwardly and in fact we can say that from the Kalman filter point of view they are realistic (i.e., they represent the “true” measurement noise covariance). The state and covariance are propagated between updates using:

$$\begin{aligned}\hat{\mathbf{x}}_{k+1}^- &= \mathbf{\Phi}_k(\hat{\mathbf{x}}_k^+) \\ \mathbf{P}_{k+1}^- &= \mathbf{\Phi}_k \mathbf{P}_k^+ \mathbf{\Phi}_k^T + \hat{\mathbf{Q}}_k\end{aligned}\tag{5.21}$$

where $\mathbf{\Phi}_k$ is the state propagation matrix, which is a linearization of the dynamic function defined before. When the platform experiences higher dynamics, such as the rapid rotations, acceleration is no longer constant and jerk is present. Therefore a Gauss-Markov model may be more suitable and can be implemented through a position-velocity-acceleration (PVA) dynamic model. Hence, the acceleration is modeled as a Gauss-Markov process with parameter $\alpha = 1/\tau_{\ddot{x}}$ where $\tau_{\ddot{x}}$ is the correlation time of the system acceleration. Then, the state vector is given by:

$$\hat{\mathbf{x}}_k = \left[\delta\beta \quad \delta\dot{\beta} \quad \delta\Delta\gamma_0 \quad \delta\Delta\dot{\gamma}_0 \quad \delta\Delta\ddot{\gamma}_0 \quad \delta\varphi_0 \quad \delta\dot{\varphi}_0 \quad \delta\ddot{\varphi}_0 \quad \delta\theta_0 \quad \delta\dot{\theta}_0 \quad \delta\ddot{\theta}_0 \right] \tag{5.22}$$

The parameter $\delta\beta$ is modeled as PV model, whereas the remainder follow a PVA model. This is because the reflection coefficient/dampening factor does not vary much for the same surface where the reflections originate.

This is not the case for the other parameters, where variations depict higher-order dynamics depending on the user platform-to-satellite relative dynamics. This is easily seen in simulated data.

The propagation matrix takes the following form (for each parameter):

$$\Phi_{PV_{GM}/PVA_{GM}} = \begin{bmatrix} \Phi_{\beta_{GM}}^{2 \times 2} & 0 & 0 & 0 \\ 0 & \Phi_{\Delta\gamma_{0GM}}^{3 \times 3} & 0 & 0 \\ 0 & 0 & \Phi_{\varphi_{0GM}}^{3 \times 3} & 0 \\ 0 & 0 & 0 & \Phi_{\theta_{0GM}}^{3 \times 3} \end{bmatrix} \quad (5.23)$$

where:

$$\Phi_{3 \times 3}^{GM-PVA} = \begin{bmatrix} 1 & \Delta t & \frac{\alpha\Delta t + e^{-\alpha\Delta t} - 1}{\alpha^2} \\ 0 & 1 & \frac{1 - e^{-\alpha\Delta t}}{\alpha^2} \\ 0 & 0 & e^{-\alpha\Delta t} \end{bmatrix} \quad (5.24)$$

The process noise matrix is given by (following the same PVA *Gauss-Markov* system model):

$$Q_{PV_{GM}/PVA_{GM}} \equiv E[w_k w_k^T] = \begin{bmatrix} Q_{\beta_{GM}}^{2 \times 2} & 0 & 0 & 0 \\ 0 & Q_{\Delta\gamma_{0GM}}^{3 \times 3} & 0 & 0 \\ 0 & 0 & Q_{\varphi_{0GM}}^{3 \times 3} & 0 \\ 0 & 0 & 0 & Q_{\theta_{0GM}}^{3 \times 3} \end{bmatrix} \quad (5.25)$$

where

$$\mathbf{Q}_{\Delta\gamma_{0GM}}^{3\times 3} = \mathbf{Q}_{\varphi_{0GM}}^{3\times 3} = \mathbf{Q}_{\theta_{0GM}}^{3\times 3} = \begin{bmatrix} q_{11} & q_{12} & q_{13} \\ q_{21} & q_{22} & q_{23} \\ q_{31} & q_{32} & q_{33} \end{bmatrix} \quad (5.26)$$

and the matrix coefficients are given by:

$$\begin{aligned} q_{11} &= \frac{e^{-2\alpha\Delta t} S_M}{6\alpha^5} \left[-3 - 12\alpha e^{\alpha\Delta t} \Delta t + e^{2\alpha\Delta t} (3 + 6\alpha\Delta t - 6\alpha^2\Delta t^2 + 2\alpha^3\Delta t^3) \right] \\ q_{12} &= \frac{e^{-2\alpha\Delta t} S_M}{2\alpha^4} \left[1 + e^{\alpha\Delta t} (-1 + \alpha\Delta t) \right]^2 \\ q_{13} &= \frac{S_M}{2\alpha^3} \left[1 - e^{-2\alpha\Delta t} - 2\alpha e^{-\alpha\Delta t} \Delta t \right] \\ q_{21} &= q_{12} \\ q_{22} &= -\frac{S_M}{2\alpha^3} \left[3 + e^{-2\alpha\Delta t} - 4e^{-\alpha\Delta t} - 2\alpha\Delta t \right] \\ q_{23} &= \frac{e^{-2\alpha\Delta t} S_M}{2\alpha^2} \left[e^{\alpha\Delta t} - 1 \right]^2 \\ q_{31} &= q_{13} \\ q_{32} &= q_{23} \\ q_{33} &= \frac{S_M}{2\alpha} \left[1 - e^{-2\alpha\Delta t} \right] \end{aligned}$$

The term $\alpha = 1/\tau_{\ddot{x}}$ is again the correlation time of the system acceleration, as used in the transition matrix (Eq. 5.24), and S_M represents the multipath parameters spectral amplitudes (being S_β , $S_{\Delta\gamma_0}$, S_{φ_0} , S_{θ_0}) associated with the white noise driving functions.

The partial derivative, from the *Jacobian* matrix H_k , for the state-vector parameter β (multipath reflection-coefficient/dampening factor) is given by:

$$\frac{\partial \Delta \hat{M}_{01}^g}{\partial \beta} = \left(\frac{1}{u^2 + v^2} \right) \left\{ \begin{array}{l} \left[\begin{array}{l} \sin \left(\Delta \gamma_0 - \frac{2\pi}{\lambda_{L_i}} \text{dist}_{01} \cos(\varphi_0 - \phi_{01}) \cos \theta_0 \right) \\ - \sin \Delta \gamma_0 - 2\beta \sin \left(\frac{2\pi}{\lambda_{L_i}} \text{dist}_{01} \cos(\varphi_0 - \phi_{01}) \cos \theta_0 \right) \end{array} \right] \cdot v - \\ \left[\begin{array}{l} \cos \Delta \gamma_0 + \cos \left(\Delta \gamma_0 - \frac{2\pi}{\lambda_{L_i}} \text{dist}_{01} \cos(\varphi_0 - \phi_{01}) \cos \theta_0 \right) \\ + 2\beta \cos \left(\frac{2\pi}{\lambda_{L_i}} \text{dist}_{01} \cos(\varphi_0 - \phi_{01}) \cos(\theta_0) \right) \end{array} \right] \cdot u \end{array} \right\} \quad (5.27)$$

and for the parameter multipath phase-delay, that is $\Delta \gamma_0$:

$$\frac{\partial \Delta \hat{M}_{01}^g}{\partial \Delta \gamma_0} = \left(\frac{1}{u^2 + v^2} \right) \left\{ \begin{array}{l} \left[\begin{array}{l} \beta \left(\cos \left(\Delta \gamma_0 - \frac{2\pi}{\lambda_{L_i}} \text{dist}_{01} \cos(\varphi_0 - \phi_{01}) \cos \theta_0 \right) - \cos \Delta \gamma_0 \right) \end{array} \right] \cdot v + \\ \left[\begin{array}{l} \beta \left(\sin \Delta \gamma_0 + \sin \left(\Delta \gamma_0 - \frac{2\pi}{\lambda_{L_i}} \text{dist}_{01} \cos(\varphi_0 - \phi_{01}) \cos \theta_0 \right) \right) \end{array} \right] \cdot u \end{array} \right\} \quad (5.28)$$

The multipath geometric parameters partial derivatives, starting with the reflector azimuth angle, φ_0 , upon the master-antenna are given by:

$$\frac{\partial \Delta \hat{M}_{01}^q}{\partial \varphi_0} = \left(\frac{1}{u^2 + v^2} \right) \left\{ \begin{array}{l} \left[\left(\beta^2 \cos \left(\frac{2\pi}{\lambda_{L_i}} dist_{01} \cos(\varphi_0 - \varphi_{01}) \cos \theta_0 \right) + \right. \right. \\ \left. \left. \beta \cos \left(\Delta \gamma_0 - \frac{2\pi}{\lambda_{L_i}} dist_{01} \cos(\varphi_0 - \varphi_{01}) \cos \theta_0 \right) \right] \cdot v - \\ \left(\frac{2\pi}{\lambda_{L_i}} dist_{01} \sin(\varphi_0 - \varphi_{01}) \cos \theta_0 \right) \\ \left[\left(-\beta \sin \left(\Delta \gamma_0 - \frac{2\pi}{\lambda_{L_i}} dist_{01} \cos(\varphi_0 - \varphi_{01}) \cos \theta_0 \right) + \right. \right. \\ \left. \left. \beta^2 \sin \left(\frac{2\pi}{\lambda_{L_i}} dist_{01} \cos(\varphi_0 - \varphi_{01}) \cos \theta_0 \right) \right] \cdot u \\ \left(\frac{2\pi}{\lambda_{L_i}} dist_{01} \sin(\varphi_0 - \varphi_{01}) \cos \theta_0 \right) \end{array} \right\}$$

(5.29)

and for the reflector azimuth-angle upon the master-antenna, θ_0 , by:

$$\frac{\partial \Delta \hat{M}_{01}^q}{\partial \theta_0} = \left(\frac{1}{u^2 + v^2} \right) \left\{ \begin{array}{l} \left[\left(\beta^2 \cos \left(\frac{2\pi}{\lambda_{L_i}} dist_{01} \cos(\varphi_0 - \varphi_{01}) \cos \theta_0 \right) + \right. \right. \\ \left. \left. \beta \cos \left(\Delta \gamma_0 - \frac{2\pi}{\lambda_{L_i}} dist_{01} \cos(\varphi_0 - \varphi_{01}) \cos \theta_0 \right) \right) \right] \cdot v - \\ \left(\frac{2\pi}{\lambda_{L_i}} dist_{01} \cos(\varphi_0 - \varphi_{01}) \sin \theta_0 \right) \\ \left[\left(-\beta \sin \left(\Delta \gamma_0 - \frac{2\pi}{\lambda_{L_i}} dist_{01} \cos(\varphi_0 - \varphi_{01}) \cos \theta_0 \right) + \right. \right. \\ \left. \left. \beta^2 \sin \left(\frac{2\pi}{\lambda_{L_i}} dist_{01} \cos(\varphi_0 - \varphi_{01}) \cos \theta_0 \right) \right) \right] \cdot u \\ \left(\frac{2\pi}{\lambda_{L_i}} dist_{01} \cos(\varphi_0 - \varphi_{01}) \sin \theta_0 \right) \end{array} \right\} \quad (5.30)$$

where, for all the parameters partial derivatives, we have:

$$v = [\sin(\Delta \gamma_1) - \sin(\Delta \gamma_0) + 2\alpha_0 \sin(\Delta \gamma_1 - \Delta \gamma_0)] \quad (5.31)$$

$$u = [\cos(\Delta \gamma_1) + \cos(\Delta \gamma_0) + 2\alpha_0 \cos(\Delta \gamma_1 - \Delta \gamma_0)] \quad (5.32)$$

5.3 Observability

The *Kalman* filter has been used extensively in the real-time precise positioning and navigation area, particularly in the field of tracking and parameter estimation such as with GNSS and INS systems, or a combination of both. By contrast, another two issues raised by *Kalman* during his seminal work, *controllability* and *observability* are seldom seen in the immense GNSS literature although they are the two fundamental tools to design properly a Kalman filter.

In this dissertation (and respective implementation in a C++ algorithm) the real-time estimation of multipath parameters, per satellite, and posterior filtering of carrier-phase multipath relies and is achieved upon time-continuous “derived” multipath measurements. Therefore, it is always important to guarantee within the MIMICS algorithm that there are enough measurements in the entire estimation process to predict the system state over the long term.

This problem is covered in the system *observability* analysis, and in some situations it can be fixed by reducing the number of state variables, or by adding additional sensors. Formally, a system is observable if the initial state can be determined by observing the output for some finite period of time. Using again the *Kalman* filter equations:

$$x_{k+1} = \Phi_k x_k, \text{ where } z_k = Hx_k \quad k = 0, \dots, m-1$$

then we can use the following expressions:

$$\begin{aligned}
z_0 &= \mathbf{H}x_0 \\
z_1 &= \mathbf{H}x_1 = \mathbf{H}\Phi x_0 \\
z_2 &= \mathbf{H}x_2 = \mathbf{H}(\Phi)^2 x_0 \\
&\vdots \\
z_{n-1} &= \mathbf{H}x_{n-1} = \mathbf{H}(\Phi)^{n-1} x_0
\end{aligned} \tag{5.33}$$

which leads to the following *observability* equation:

$$\Xi = \begin{bmatrix} \mathbf{H}^T & \Phi^T \mathbf{H}^T & \dots & (\Phi^T)^{n-1} \mathbf{H}^T \end{bmatrix} \tag{5.34}$$

A system with state vector x_k of dimension n is observable if the *observability* matrix Ξ has row rank (that is, n linearly independent rows). The implementation of an *observability* module within the thesis software suite was quite straight-forward, and throughout the tests performed the system was always observable.

6 Tests and Results

Machine control and automation has always been perceived as an intermediate process to increase industrial productivity (and thus profitability), operability, comfort, and safety net gain for human lives and goods. However one of the biggest limitation factors to achieve and implement successful automation systems for the markets of surveying, precision agriculture, aircraft precision approach, maritime ship guidance, and construction automation (just to name a few) has been difficult to prove that the

underlying positioning system can provide reliably and continuously position and navigation information throughout all conditions, and scenarios.

Moreover, with the growing establishment of continuously operating GNSS reference stations employed in network-RTK services of which machine automation has been one of the keenest users, some of the GNSS residual biases (mostly atmospheric) have been successfully ameliorated.

Therefore it was very important to assess thoroughly throughout this dissertation if assumptions and modeling of multipath spectra in dual-antenna systems, when the platform has variable dynamics, were accurate and representative of real-live scenarios. Therefore, based on the data obtained from those assumptions, the MIMICS algorithm developed in this dissertation can be employed and process the raw multipath-contaminated data, in real-time, and check if this approach is successful.

6.1 GNSS Software Simulation

The first step was to develop specific Matlab/C++ functions for this purpose as it is always a good idea to develop simulation software sub-routines modeling signal phenomena in dynamical systems. This is due to the ease of obtaining data repeatability and consistency, especially when changing simulation parameters to reflect multiple simulation dynamic scenarios.

As seen in next figure (Figure 6.1) urban canyons are typical kinematic scenarios where dual-antenna GNSS systems can be used not only to derive vehicle pitch and yaw angles (depending on the antennas configuration) as well as to remove multipath in real-time as proposed in this dissertation.

Actually, nowadays many new vehicles already possess dynamic control systems, using a combination of sensors such as inertial, odometres, and GNSS (all collected/processed using CAN-bus - Controller Area Network – protocols) which automatically assist the vehicle wheel-control in icy/slippery roads. The estimation of vehicle pitch/yaw from GNSS dual-antenna systems is very important in these situations as it can help to determine the vehicle slip angle, that is, the difference between a platform's intended heading angle, and the true heading.

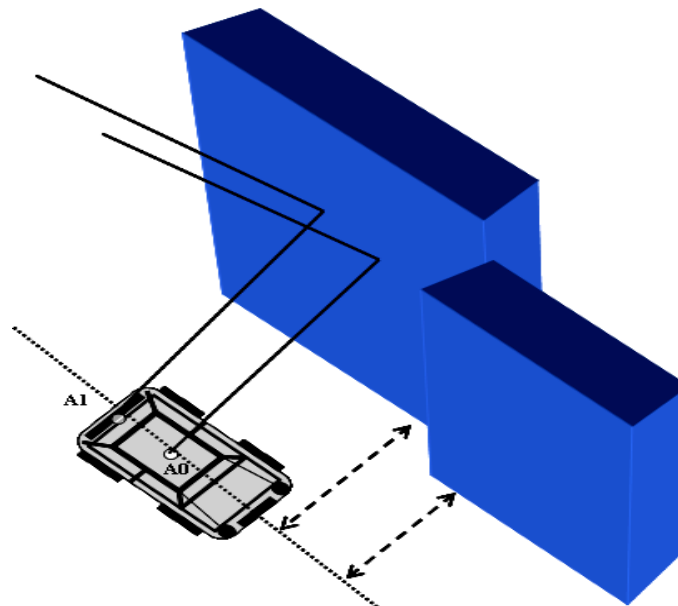


Figure 6.1: Illustration of one of the possible scenarios implemented in the simulator

For this scenario the software simulation routines generated data containing dual-antenna multipath signals arising from strong specular reflectors with variable dimensions and fast changing reflector distance to the vehicle (as seen in Figure 6.1). The processing results from this typical simulation scenario can be seen in next figure (Figure 6.2) where the *Kalman* filter takes about 90 seconds to achieve steady state and estimate the four multipath parameters.

Note that in this simulation, rather simplistic, one assumed that all but the multipath phase delay had constant values. This is due to multipath phase delay changing continuously along the satellite path, even for static platforms, and its intrinsic correlation with the reflector distance, depending if the satellite is rising or setting (one can see this quantity decreasing in the second plot starting from the top). The MIMICS algorithm was able to detect and properly estimate these features.

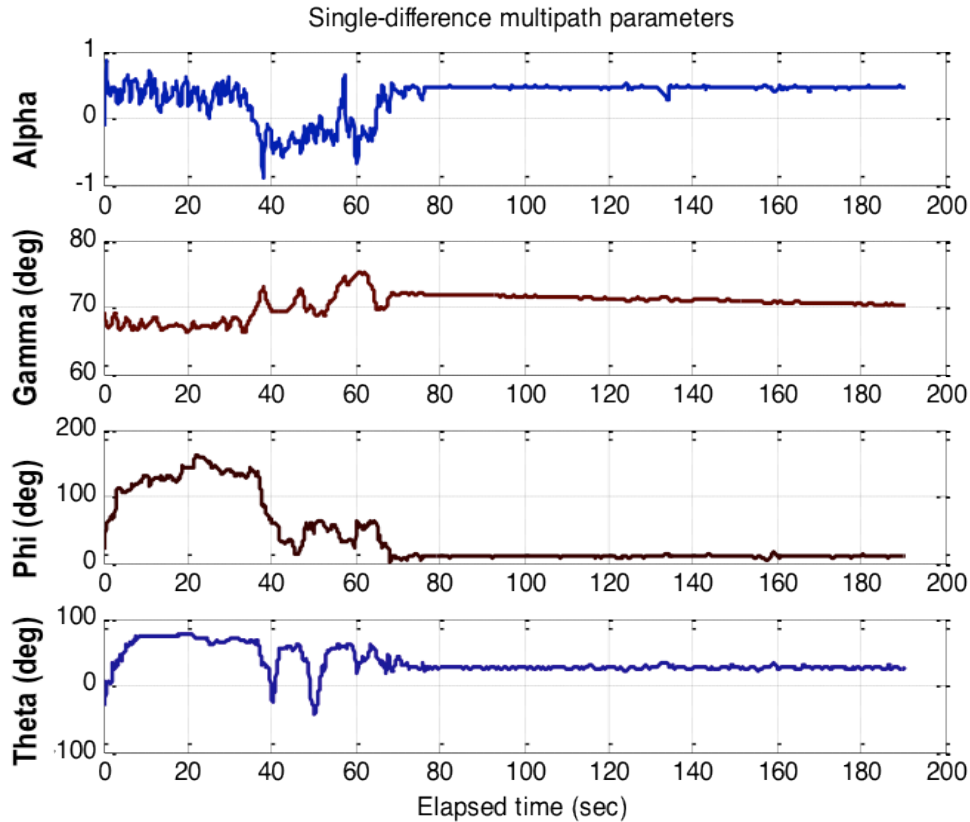


Figure 6.2: Multipath parameters estimation using software simulations

In this model the intention is to mimic scenarios where GNSS dual-antenna performs either an initial random motion calibration (part of the system initialization, as it is done with certain inertial navigation systems with initial alignment), or during a vehicle long-term random dynamic behavior.

Nevertheless, as it is necessary to assure GNSS dual-antenna random motion helps decorrelating multipath from specular reflectors, I developed a simple yet powerful mean (Figure 6.3) to easily perform as many as possible dual-antenna random rotations, while

at the same time estimating between-antennas distance to fit in many dynamic platforms as possible yet still respecting MIMICS underlying theoretical assumptions.

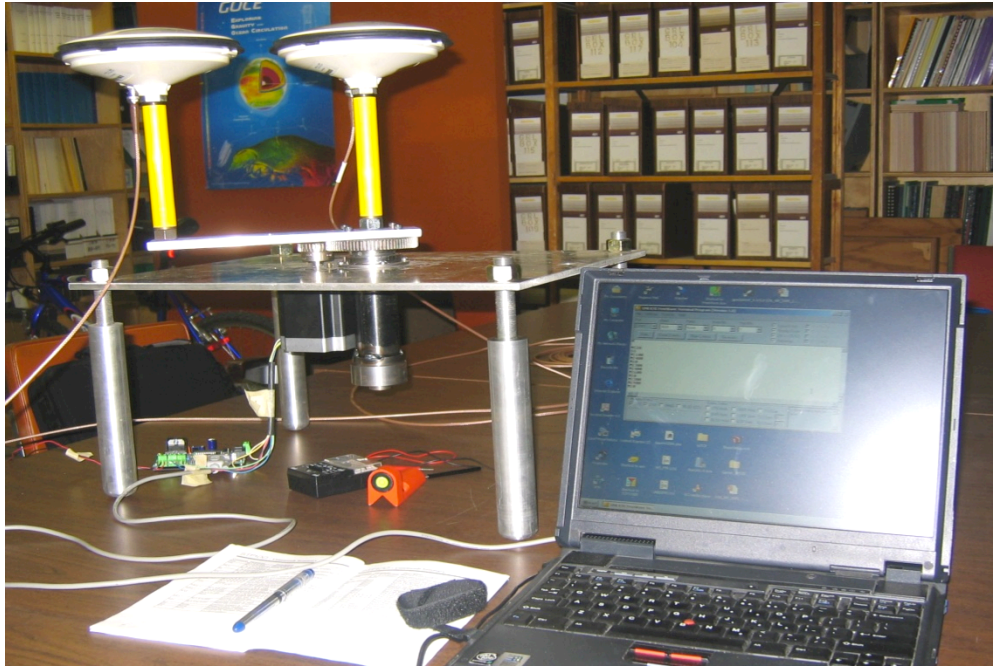


Figure 6.3: Mechanical setup for dual-antennas random motion, and antenna optimal distance

6.2 GNSS Hardware Simulation

The exact test scenario was implemented with the same GNSS antenna/receiver hardware, however using data from a hardware-simulator (Spirent 4760) to validate this approach instead of real-live satellite signals. In the next figure (Figure 6.4) one can see

both receivers connected to the two simulator RF outputs, and the external oscillator connected to the receivers via a splitter.

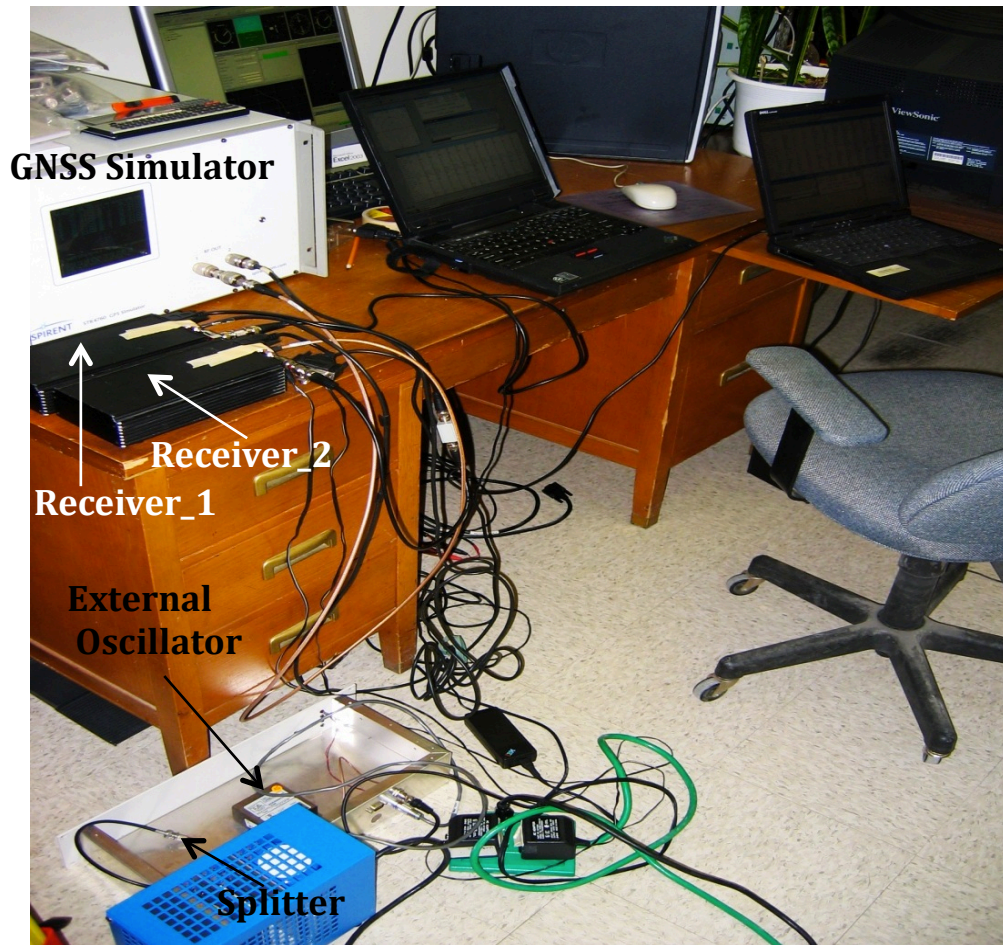


Figure 6.4: Hardware simulator setup with all the required equipment

In Figure 6.5 one can see the potential in using multipath hardware-simulated data through the use of pre-defined perfect reflectors in the vicinity of the antenna(s). For each multipath path, one channel is allocated and superimposed on the direct signal.

Its location (thus working as a reflector) can be defined and even pre-programmed to change its dimensions and relative offsets to the vehicle where the antennas are located, while the vehicle roves. Besides, the vehicle dynamics can also be programmed to vary accordingly.

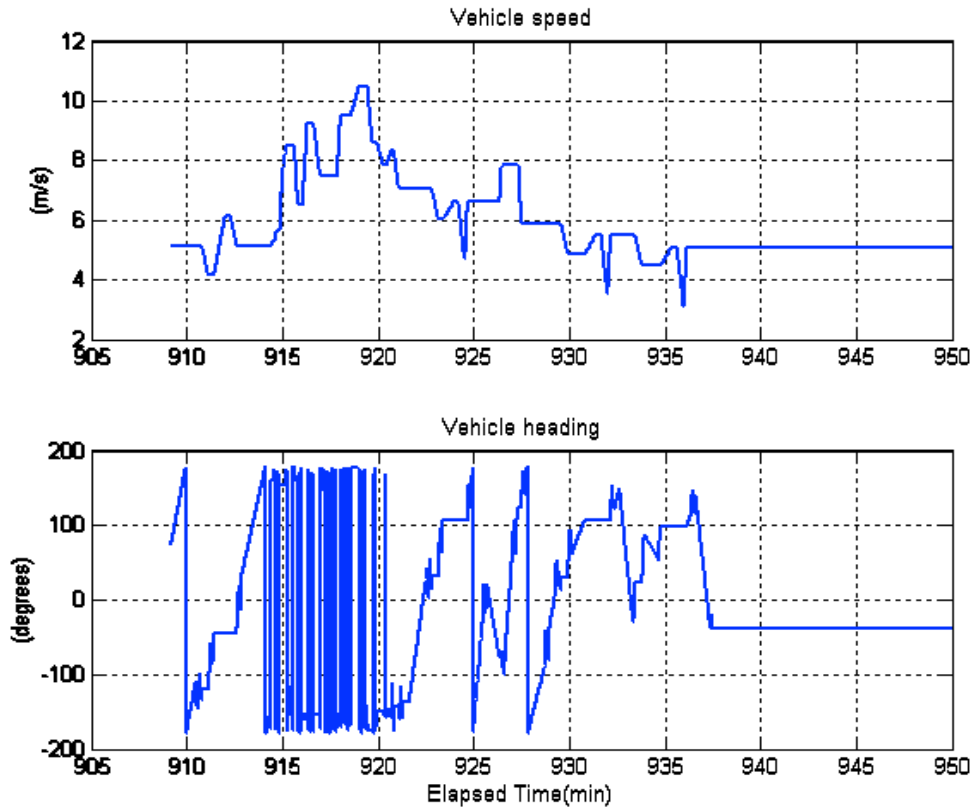


Figure 6.5: Vehicle speed and heading pre-programmed in the simulator scenario set-up

In the top panel of next figure (Figure 6.6), one can see the results from the hardware-simulated data for a specific satellite (in blue). This single-difference multipath data is obtained from the difference between the described scenario with the channels-allocated reflector active, and the same test running a *posteriori* without these channels active.

Besides the receiver noise, the only error source remaining after differencing should be multipath (atmospheric errors are eliminated due to the short spacing between antennas).

In the bottom panel are depicted the results using the MIMICS processing strategy (in red) from the data set containing the multipath.

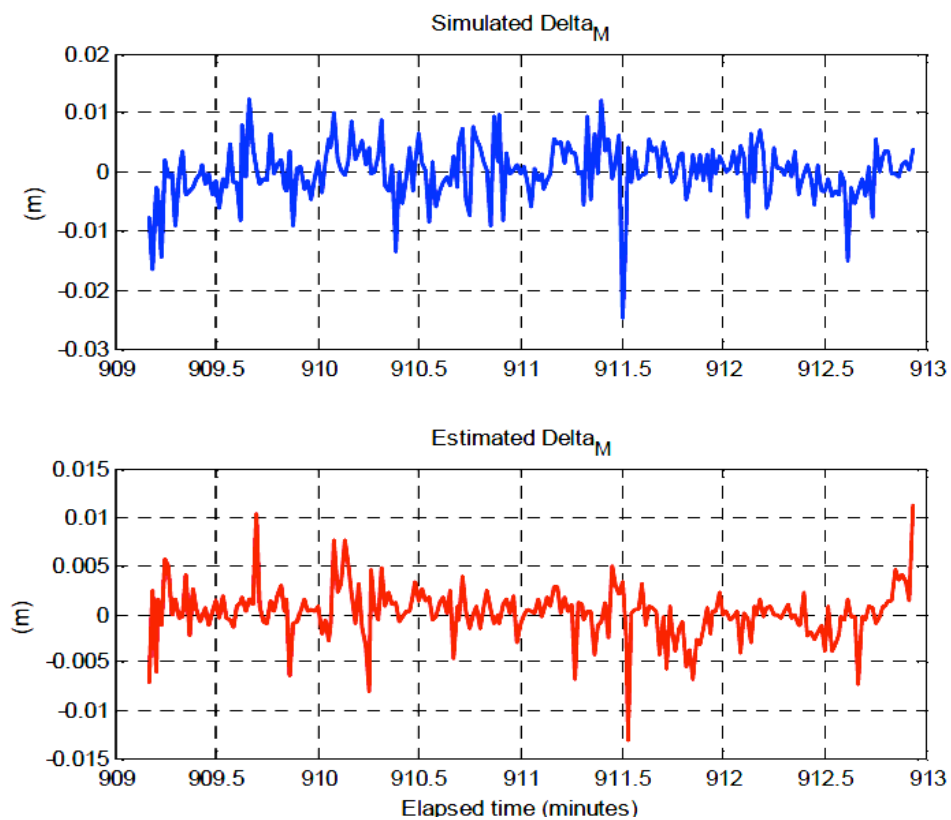


Figure 6.6: Top plot is the simulated multipath and in the bottom the estimated

At first glance, it is easy to see that both plots have many similarities. However, we must acknowledge that we are not looking for exact multipath signatures since it is mostly a high-frequency multipath spectrum (thus including other noise frequency components),

coming from a kinematic test. More important is to assess if the estimated multipath amplitude and phase are related to the simulated ones.

This becomes clear when one reckons that these multipath-estimated observables and the observable depicted in equation 1 are the same (therefore dependent on the multipath relative amplitude and phase). The statistics from both plots are quite similar, where the mean value is close to zero (which confirms that carrier-phase multipath is zero-mean valued, unlike code multipath), and their amplitudes vary well within the range of $\pm 5\text{mm}$.

We would expect bigger multipath values; however in this tests a couple of high-end receivers/antennas, which already eliminate to a big extent its effect. As it is difficult to compare frequency components from both plots as explained before, we do the comparison in the time domain (and because we consider multipath as a highly-correlated random error with different periods).

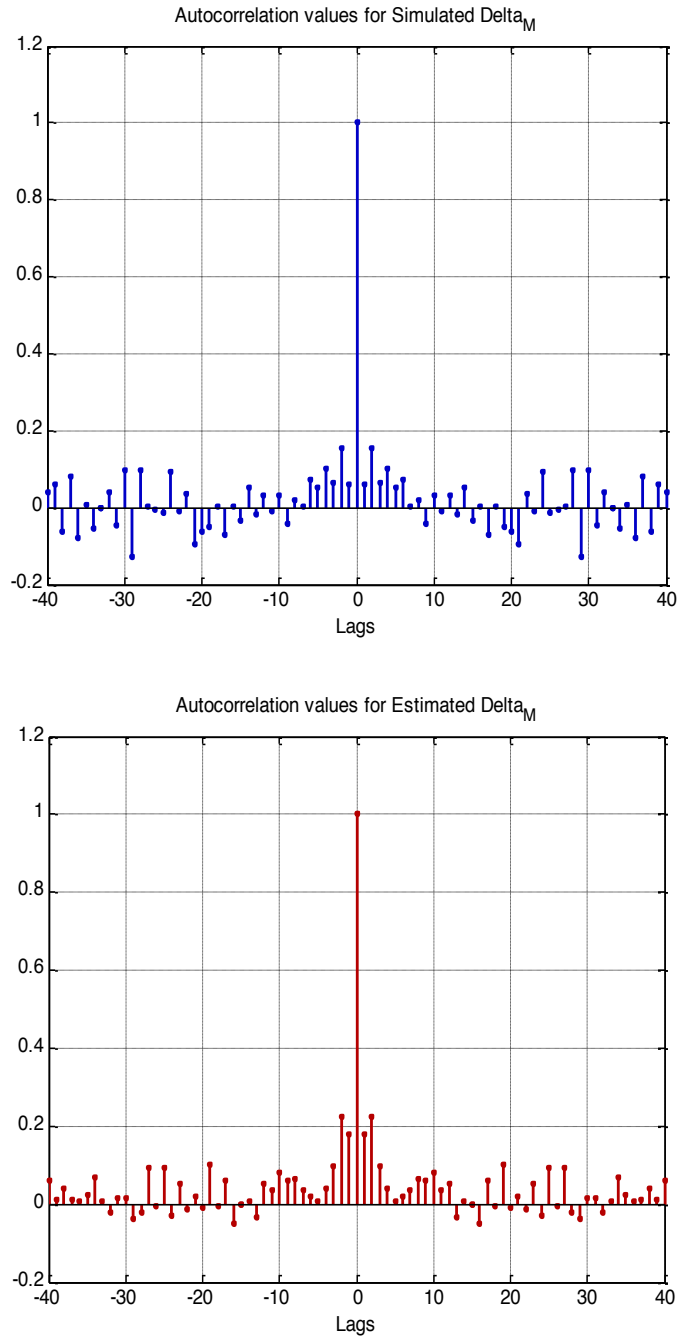


Figure 6.7: Autocorrelation values for simulated data (in blue) and estimated data (in red)

In Figure 6.7 one can see the time-domain signals behavior (of the simulated and estimated). It is worth noting, however, that, in each plot, although there is clear evidence

of different correlation periods, there is also a rapid decay between consecutive lags. The simulated velocity of the vehicle was programmed to vary between 0 and 40 km/h with accelerations and constant velocities (normal in an urban environment). This originated the kind of multipath we were expecting and assumed in our models, i.e., a quasi-random error depicted in the previous figure.

6.3 Real-Live Signal Tests

To mimic carrier-phase multipath on dual-antenna dynamic systems it was critical to obtain real-live signal data following same approach as during all the simulation scenarios. This was achieved through the use of a GNSS dual-antenna setup on top of a vehicle (Figure 6.8). As seen in figure, there were actually three non-collinear antennas, as used in GNSS-based attitude systems, as part of the system setup.

This real-live signal test can be considered realistic regarding typical dual-antenna GNSS systems employed in precision agriculture, construction, etc. The test included a mix of straight-paths with varying velocity along with sharp curves (subjecting the antennas to high dynamics) repeatedly, with a constant strong reflector located nearby. Some undesirable effects, such as vibration, experienced by heavy machinery, were not simulated or retrieved.

However, for this study only data from the dual-antenna setup, positioned along the longitudinal section and aligned with the vehicle's direction, was processed and used

with the MIMCS algorithm. The antennas in this configuration are able to capture multipath from the specular reflector surfaces more effectively while the vehicle moves along its path.



Figure 6.8: Adaptation of a GNSS dual-antenna system to a typical vehicle



Figure 6.9: Site location where the kinematic real-live signal test was performed

Next figure (Figure 6.10) is an aerial view of the site scenario (parking lot of the Engineering Building at the University of New Brunswick in Fredericton).



Figure 6.10: Aerial view of the real-live signal test scenario

The red line depicts the area where the car performed the kinematic test for more than 2 hours, with variable speeds and rotations, and the blue lines superimposed on the building façade represent the specular reflection surfaces. One can see in this figure that the building façade is behaving as the effective reflector. The vehicle performed several motions always in the parking lot hence the view to some satellites, mostly arising from southern hemisphere, was constantly blocked by the building.

The results from this test can be seen in next figure (Figure 6.11). In the bottom figure one can see the kind of motion performed by the platform. Accelerations, jerk, idling, and several stops were performed on purpose to see the resultant multipath spectra between the antennas. The reference station was located no more than 110m away from the vehicle antennas during the test. As such, most of the usual biases were removed from

the solution and the only remaining bias can be attributed to multipath. In the top figure one can see the geometric distance calculated from the fixed-solutions of both antennas.

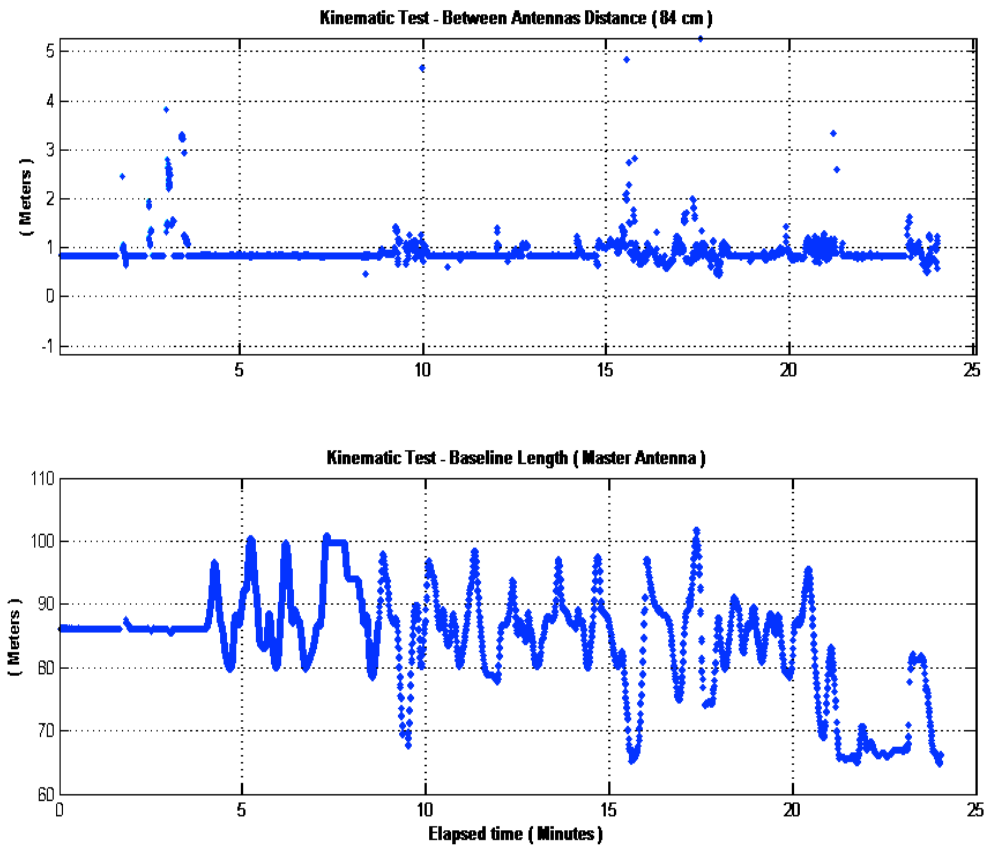


Figure 6.11: Results from the kinematic test (top plot RTK-based moving baseline estimation, and bottom plot RTK-based baseline distance between rover master antenna and base station)

Since the bar was accurately measured before (84 cm) it is easier in this way to evaluate the solution quality. The “outliers” seen in the picture come from code solutions because the building mentioned before was blocking most of the satellites towards the southeast. As such, many times fewer than 5 satellites were available.

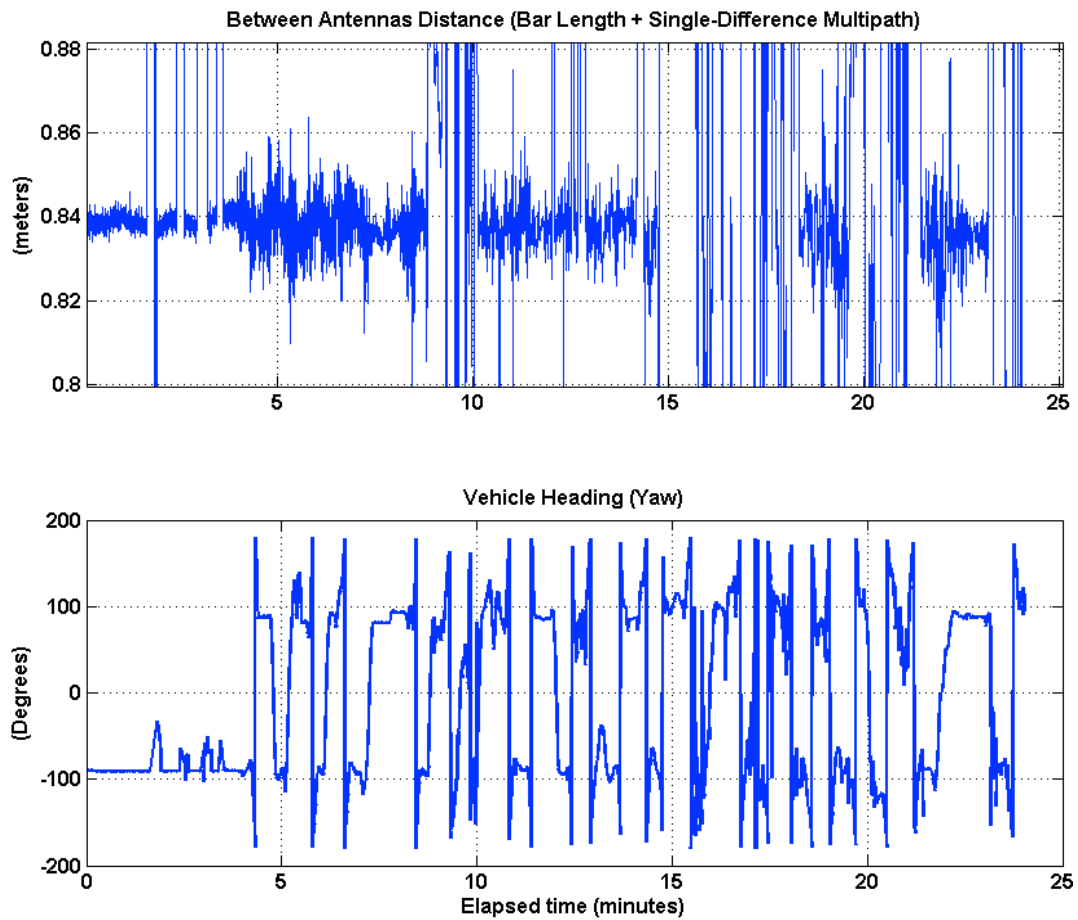


Figure 6.12: Correlation between vehicle dynamics (heading angle) and the multipath spectra

Previous figure (Figure 6.12) depicts the highly visible correlation between the vehicle dynamics, especially heading (performed on purpose during the tests to assess this phenomena), and multipath spectra.

It is also visible that at certain intervals the combination of strong multipath, lack of sufficient visible satellite, and most likely the very short distance to the reflector facades caused the system to lose periodically RTK-derived solutions.

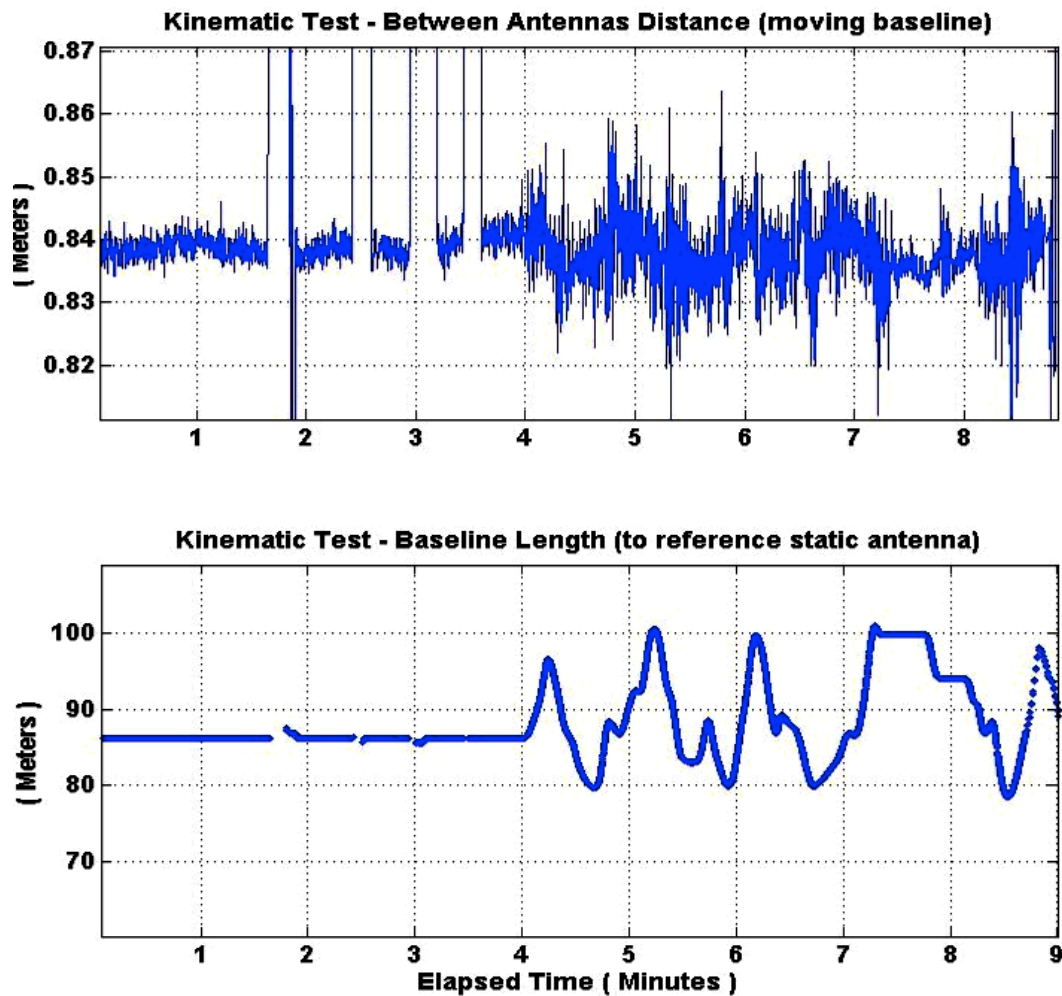


Figure 6.13: Results from kinematic tests. Zoom to first 9 minutes

Looking at the first 9 minutes of results (Figure 6.13), one can see that when the car is still stopped the multipath has a very clear quasi-sinusoidal behaviour with a period of a

few minutes. Also, one can see that it is zero-meant as expected (unlike code multipath). When the car starts moving (at about the 4 minute mark), the noise figure is amplified (depending on the platform velocity), but one can still see a mixture of low-frequency components coming from multipath (although with shorter periods).

These results indicate, firstly, that regardless of the distance between two antennas, multipath will not be eliminated after differencing, as with other biases. Secondly, when the platform has multiple dynamics, multipath spectra will change accordingly starting from the low-frequency components towards the high-frequency (*diffraction*, probably also coming from the building edges and corners).

This proves, firstly, that regardless of the distance between two antennas multipath will not be eliminated after differencing, as with other biases. Secondly, the building façade acting as a constant smooth reflector creates the most problematic kind of multipath: the deterministic specular reflection.

Thirdly, when the platform has varied dynamics, multipath spectra will change accordingly starting from the low-frequency components towards the high-frequency (diffraction, probably also coming from the building edges and corners). As such, our approach to adaptively model multipath in real time as a quasi-random process makes sense.

6.4 Multipath Observables

The multipath observables are obtained through the MIMICS algorithm. It is quite flexible in terms of latency and filter order when it comes to deriving the observables. Basically, it is dependent on the platform dynamics and the amplitude of the residuals of the whitened time-series (meaning that if they exceed a certain threshold then the filtering order doesn't fit the data).

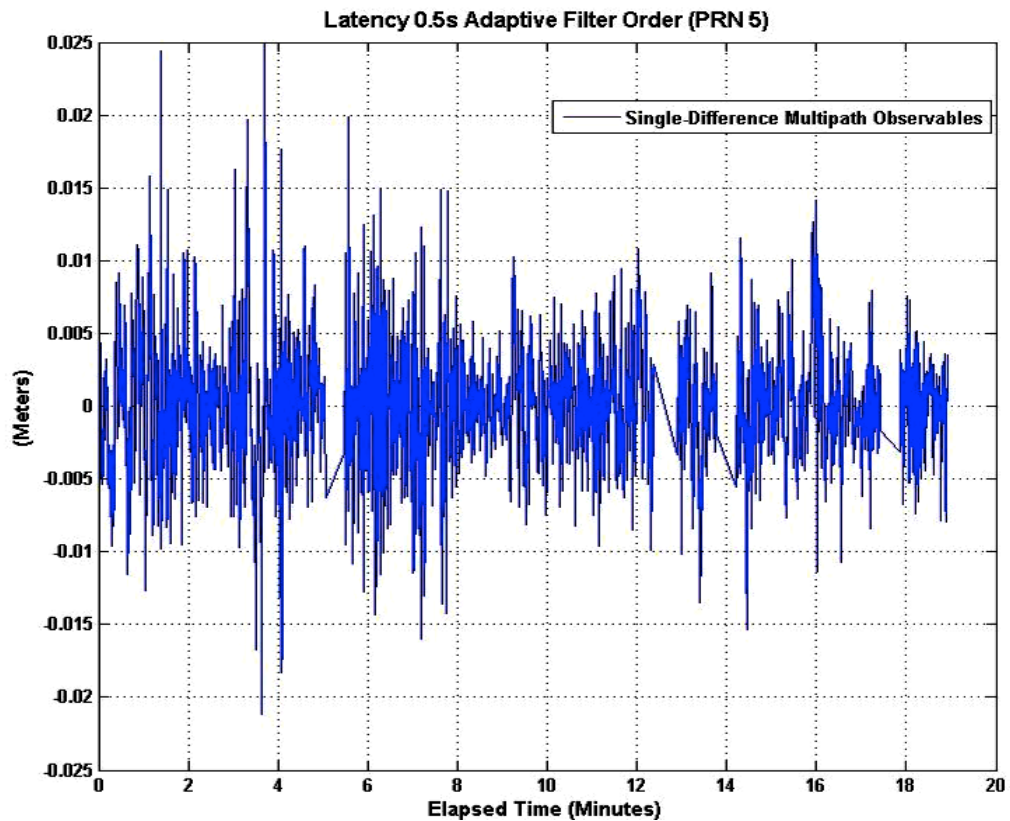


Figure 6.14: PRN 5 multipath observables delivered every 0.5 seconds

When comparing the observables delivered every half-second (Figure 6.14) for PRN 5 with the ones from every second (Figure 6.15), it is clear, from the sinusoidal behaviour of the 1s-latency data, that the bigger the interval the better to recover the true biased sinusoidal behaviour of multipath.

However in machine control, some applications require a very low latency. Therefore there must be a compromise between the multipath observables accuracy and the rate at which they are generated.

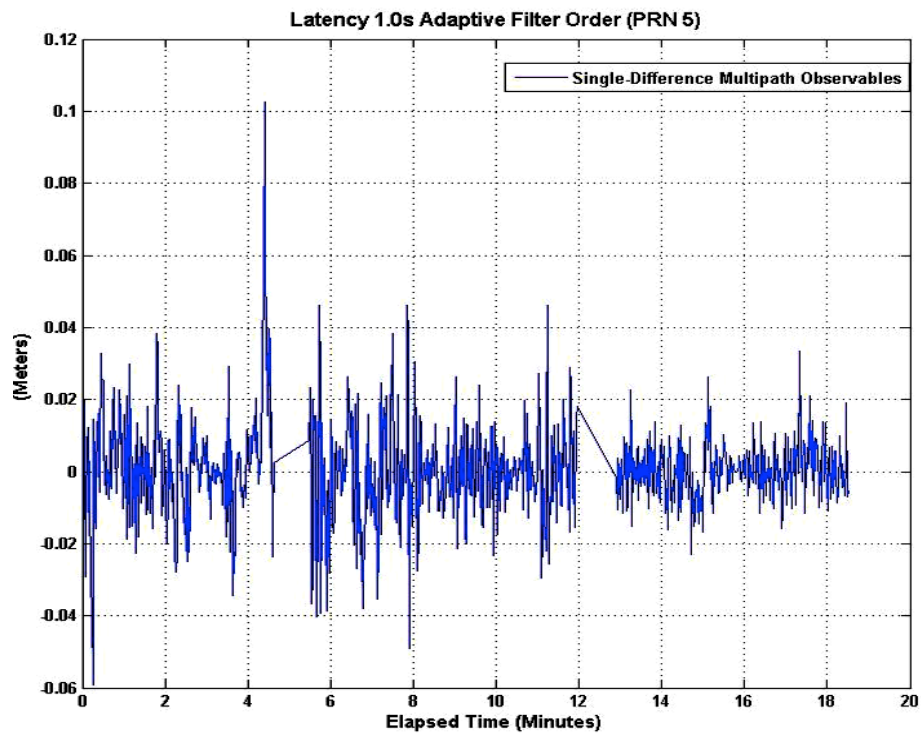


Figure 6.15: PRN 5 multipath observables delivered every second

One can see this same kind of behaviour for a different satellite (PRN 13).

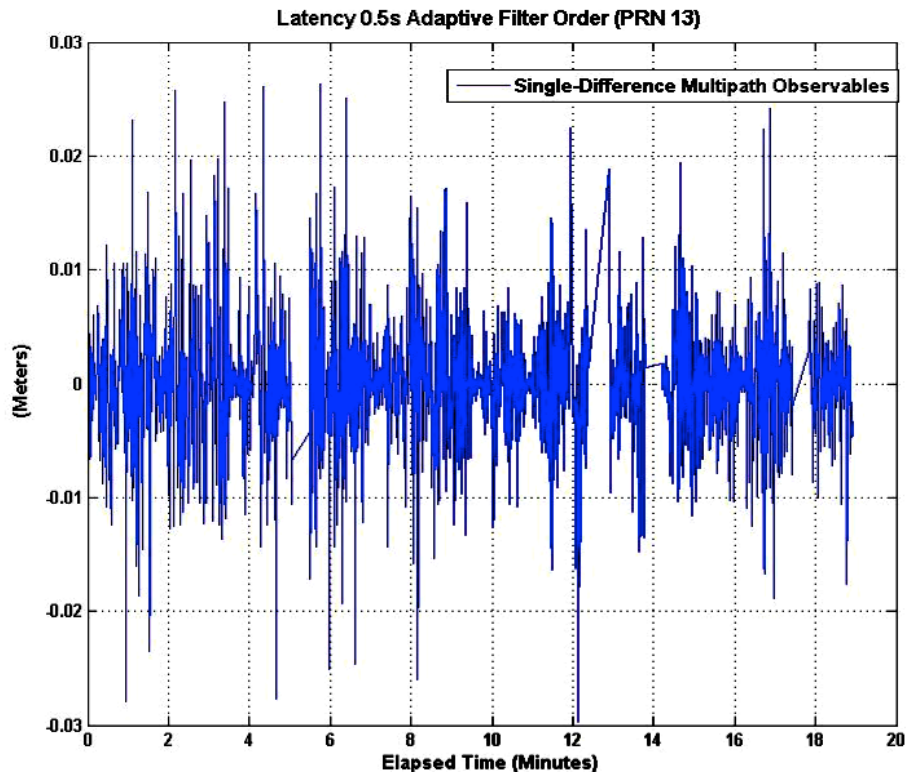


Figure 6.16: PRN 13 multipath observables delivered every 0.5 seconds

One interesting thing in the plots is that even though the amplitude and noise envelope between 0.5 seconds and 1 second sampling are different, the signal phase is very identical (as expected). This means that regardless of the variation in the observable accuracy due to latency issues, the most important parameter, reflected signal phase-delay, is still being captured.

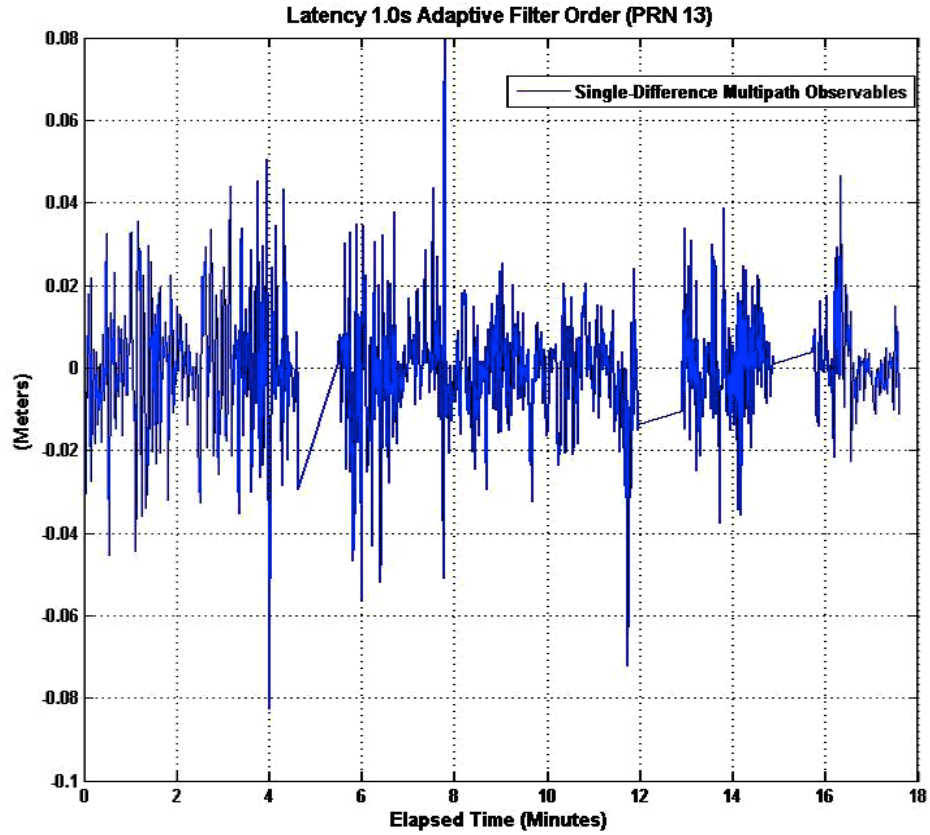


Figure 6.17: PRN 13 multipath observables delivered every second

The spectra of the derived multipath observables can be seen in the next two plots (Figures 6.18 and 6.19). Carrier-phase multipath is known to have sinusoidal periods stretching from a few tens of seconds to several minutes, depending on the reflector distance. When the antennas are mounted on a moving platform and the reflectors are within a short distance, then we can expect very short periods.

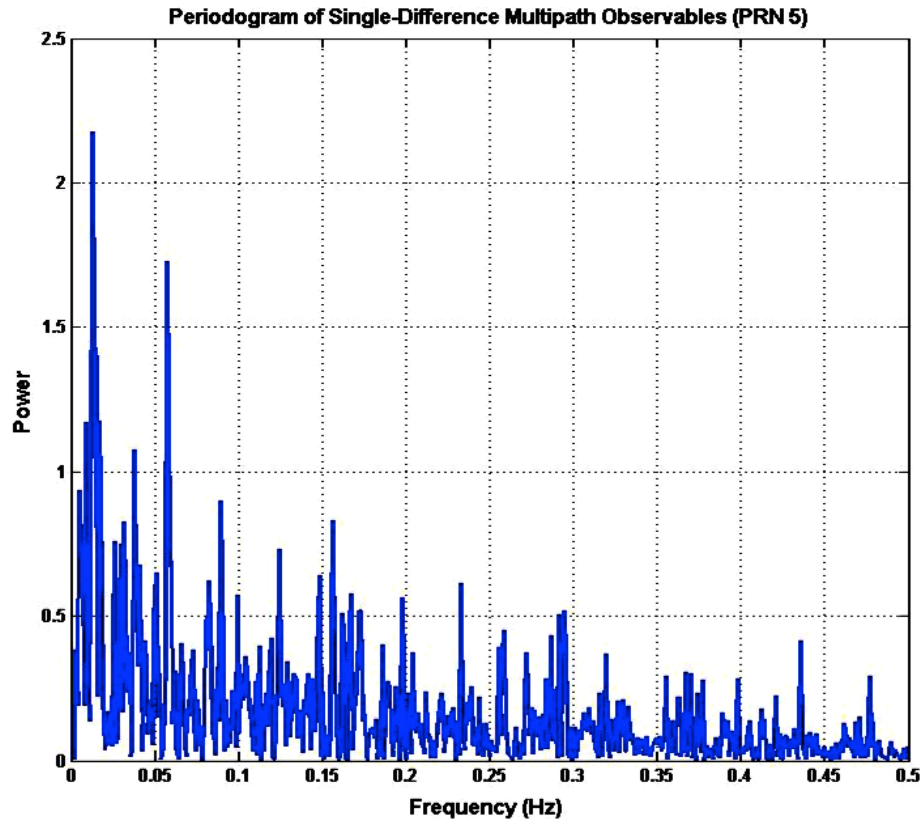


Figure 6.18: Spectra of PRN 5 multipath observables

The spectra plot from PRN 5 (Figure 6.18) has two main peaks, one at about 0.05Hz (20 seconds) and the other at about 0.0125Hz (80 seconds). The spectra plot from PRN 13 (Figure 19) has four clear peaks within the interval of 0.04Hz and 0.125Hz (8 to 25 seconds).

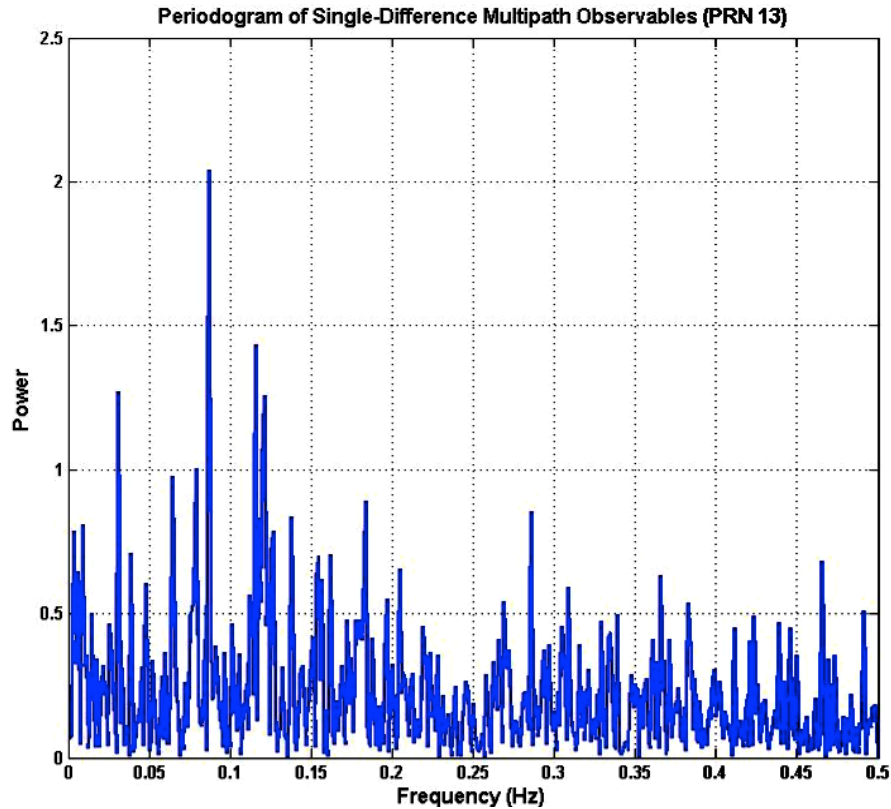


Figure 6.19: Spectra of PRN 13 multipath observables

These two satellites were chosen in particular because one had a much higher elevation angle than the other during the test, which is why they have different multipath periods.

After going through all the MIMICS algorithmic steps, from the initial data tracking and synchronization, between the dual-antenna system, up to the multipath observables estimation for each continuous satellite observed, we are now in position to generate the multipath corrections. This is done in real-time, and thus corrects each raw carrier-phase observation within the extended *Kalman* filter.

It was a recurring intention that the software developed within this dissertation must emulate real-live GNSS-RTK firmware requirements performance, that is, all steps involved in MIMICS could be implemented within usual commercial on-board GNSS-RTK pre-processing routines without affecting too much the overall processing and latency requirements.

Only in this way this proposed method could truly be considered as a state-of-the-art real-time multipath mitigation technique.

6.5 Extended Kalman Filter (EKF) Estimation

A *Kalman* filter is developed to use multipath-corrupted measurements from the dual-antenna system to estimate the multipath phase-delay and geometric parameters, from which the multipath errors in the carrier-phase measurements at each antenna can be computed.

One can see in next figure (Figure 6.20) in the solution domain three different positioning solution (up-component) plots using the original raw (multipath contaminated) measurements (top), the estimated carrier-phase multipath signal (middle), and the difference between the two above time series, that is, the GPS-RTK multipath “ameliorated” solution.

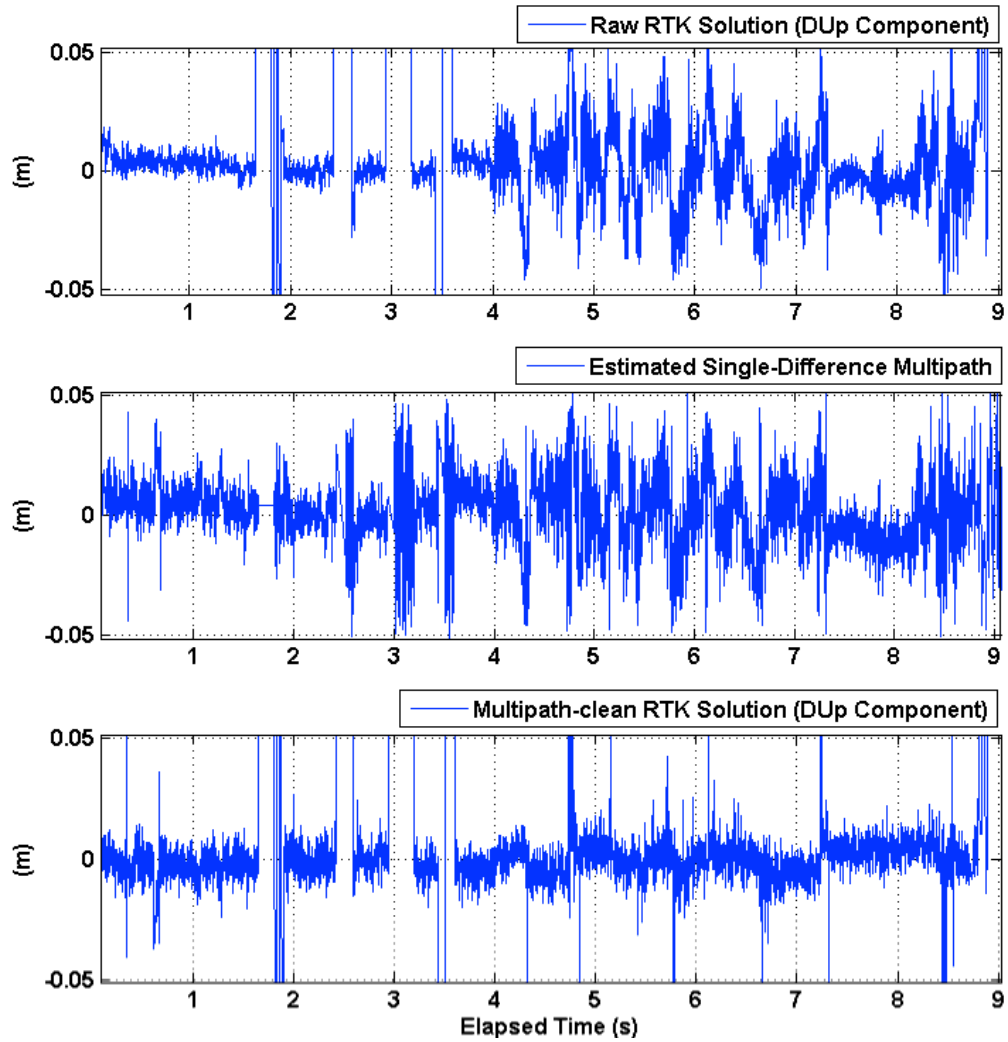


Figure 6.20: Results from the MIMICS algorithm strategy in a real-time, kinematic real-time signal scenario (a zoom-in of the first 9 minutes)

Looking (Figure 6.20) at the periods where losses-of-lock/cycle-slips did not occur, hence it is possible to extract multipath-ameliorated RTK solutions one can see clearly an improvement in the up component. The typical multipath sinusoidal behaviour is still there (quite visible between 5 and 10 minutes) however its amplitude is greatly reduced.

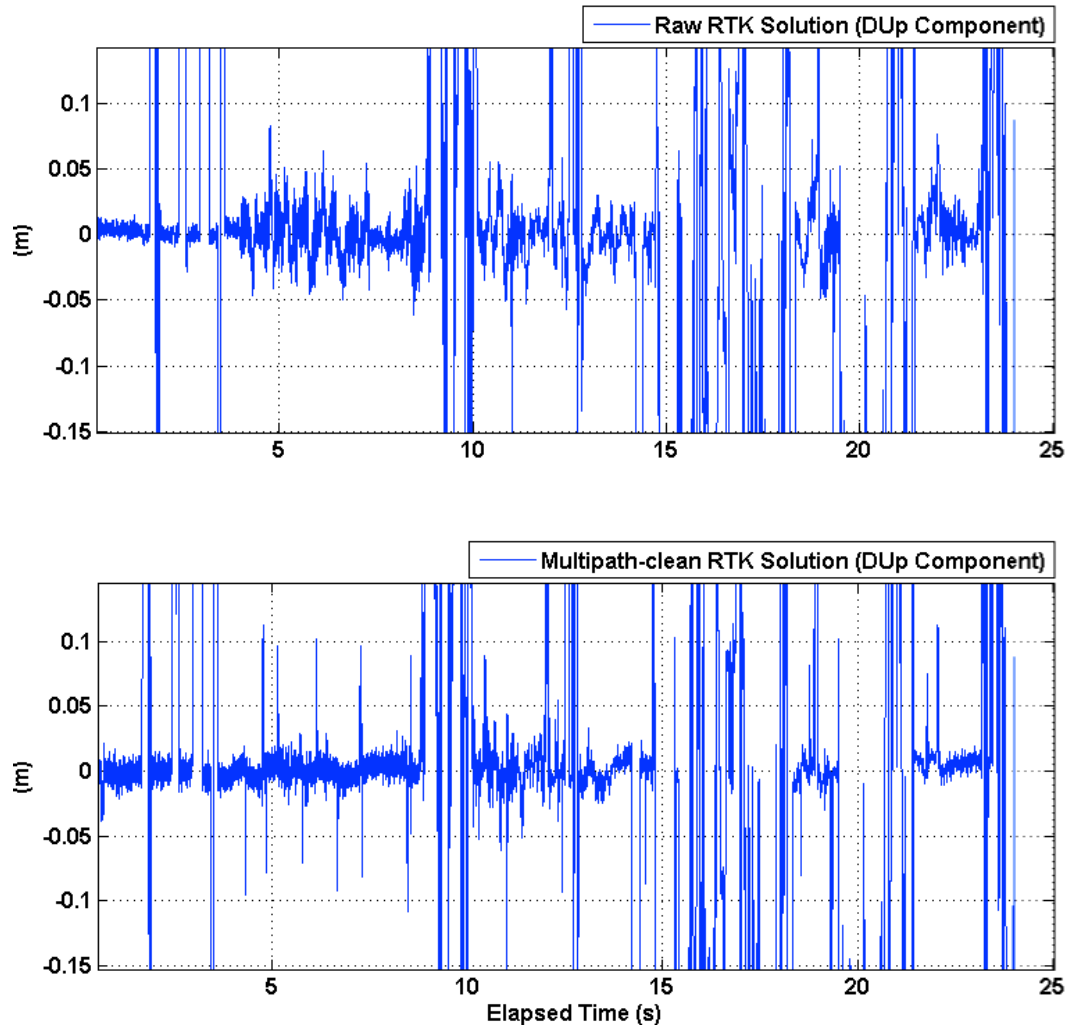


Figure 6.21: Same signals as in last figure, however just depicting the two solutions, before (top) and after (bottom) the MIMICS multipath mitigation, for 25 minutes' worth of data (the spikes represent periods when RTK solutions were not available)

Code and carrier multipath will be mapped mostly to the height solution component, therefore the high emphasis on this component throughout this dissertation. We can see in the next figure the comparison between the raw (therefore without filtering multipath using MIMICS) RTK horizontal solution against the vertical one.

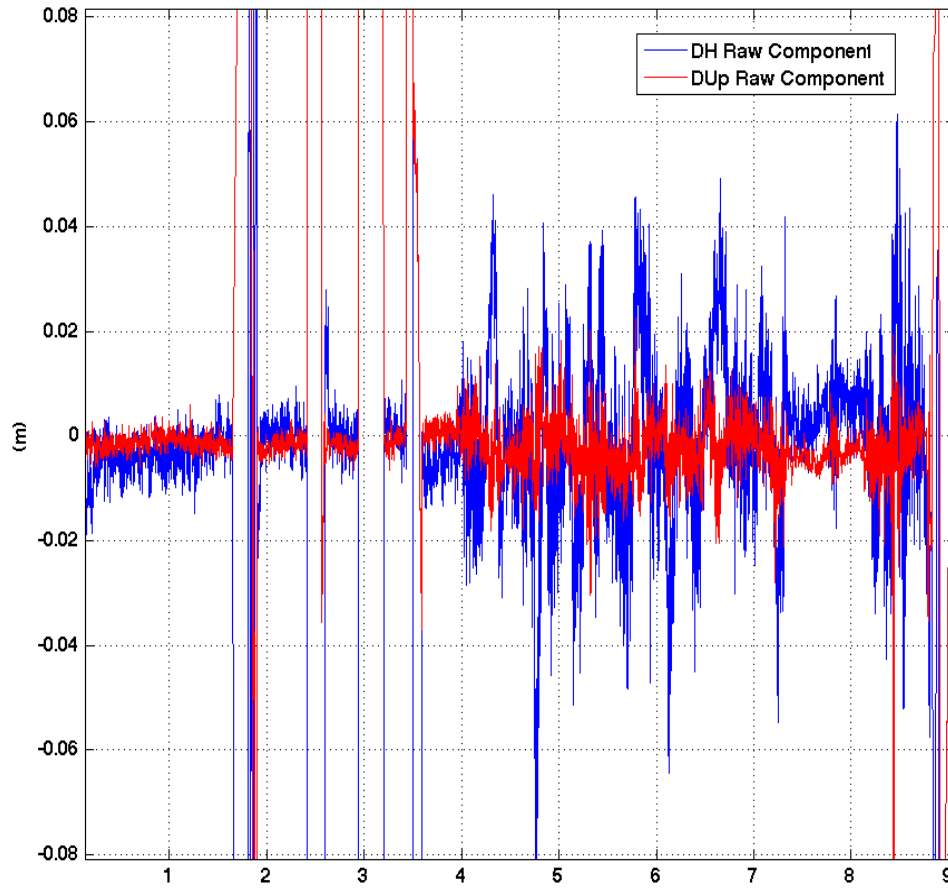


Figure 6.22: Multipath errors affecting the horizontal versus the vertical solution component

In following table one can see the statistical results from these field tests done in a moderate (when the car was away from the building façade) to severe multipath environment, i.e., when the car was very close to the building to the point where only half of the GPS satellite constellation, at the time, was visible.

| Component | RMS Before | RMS After | Improvement |
|------------------|-------------------|------------------|--------------------|
| East | 1.9 cm | 1.6 cm | 15 % |
| North | 1.7 cm | 1.5 cm | 12 % |
| Up | 2.5 cm | 1.8 cm | 28 % |

Table 6.1: Real-live signal tests statistics

The results show a reduction in multipath errors up to 28% in the up component, the most important one whereby errors are strongly mapped, especially deterministic errors such as multipath. The improvements in the horizontal components are not so profound for two reasons: first these two components are not as much affected by deterministic errors as the up component (as mentioned before), at least not in the local-level frame where these results are depicted, therefore there is not much space for improvement.

Secondly, the antennas disposition, that is, arranged in the longitudinal direction and aligned with the vehicle true heading, make the multipath phase-delay arising from the strong specular reflector to be more correlated between the dual-antenna, hence mostly being removed when performing single-differences in the scope of MIMICS algorithm.

A very interesting, and desirable, characteristic of this technique is that it is more effective when the dual-antenna experiences higher multipath periods in a quite obvious difficult and fast-changing environment such as the one in the parking lot. This is in stark

contrast to other multipath-mitigation techniques which are only effective when in controlled environments or in special conditions.

7 Conclusions and Recommendations

7.1 Introduction

Clearly carrier-phase multipath is one of the most limiting factors in accuracy and reliability regarding GNSS/RTK applications for precise positioning, and multi-antenna heading and attitude systems, as even a small separation between the antennas causes different and highly decorrelated phase-multipath errors.

At present, there are in the market low-cost single-frequency (or dual-frequency) receivers that are relatively cheap and weigh less than a kilogram (including the antenna, engine, interface board, power supply, cables) and therefore do not represent a problem for any kinematic platform to carry just two receivers. With two antennas it is possible to determine yaw and pitch angles, which for some applications is sufficient (such as for precision agriculture), and depending on their placement in the platform body, make the determination of these two angles quite robust.

At UNB we have been developing carrier-phase multipath-mitigation procedures for kinematic applications, using single-difference multipath observables with a dual-antenna system. These observables are obtained from the higher-order range-dynamic observations coming from the two antenna pseudo-random motions in kinematic applications, and thus originate a system independent of the platform/antenna chosen. In

this dissertation, we describe how the higher-order range-dynamics observations, such as range-rates and range-accelerations, can be devised to be immune to multipath, and therefore how they can be optimally used to clean the carrier-phase observable used to estimate two of the attitude angles.

In this dissertation, we describe how a typical GNSS-based dual antenna system is used to calibrate, in a first stage, and remove carrier phase multipath afterwards. The intricate relationship between the platform's 2 rover antennas dynamics and the changing multipath from nearby reflectors is explored and modeled through several stochastic and dynamical models, and their implementation in an extended Kalman filter (EKF). The tests were done under controlled environment, using either simulated data (software and hardware), or using a vehicle instrumented.

The long and thorough work of understanding and implementing the underlying functional models (especially regarding the *Jacobian* matrices), which physically represent the derived single-difference multipath observable, were absolutely crucial in this dissertation as our method of using commercial GNSS dual-antenna systems to understand phase-multipath in kinematic scenarios only now is starting to evolve.

One of these examples is the field of GNSS reflectometry (GNSS-R), whereby the dual-antenna system is used as a bi-static specular *scatterer* instrument, hence the retrieved multipath is not removed as a nuisance parameter but in fact exploited to retrieve important signal information.

7.2 Conclusions

Tests were performed using real live satellite signals, and from the results we can say that it is possible to estimate in real-time, after an initial calibration phase, the relative position of short distance strong multipath reflectors in the vicinity of the platform. Based on that, a multipath profile is created and used to correct the multipath-affected signals.

Our novel strategy seems to work well in adaptively detecting and estimating multipath profiles in real-time (or near real-time as there is a small latency to obtain multipath corrections from the MIMICS algorithm). The approach is designed to be applied in specular-rich and varying multipath environments, quite common at construction sites, harbors, airports, etc., where GNSS-based heading systems are becoming a standard.

However there are some limitations. From the most important plots, that is, the results from real-live signals, it is clear that not all multipath patterns were removed, even though the improvements are considerable. In numbers, and only considering the results “cleaned” from outliers and differential-code solutions, the up component RMS value before was 2.5 cm, and after applying MIMICS it stood at 1.8 cm RMS. This represents an improvement of 28%.

Moreover estimating multipath adaptively in real time can be a problem from a computational point of view when using high update rates. In all our tests it was defined

that the receivers should always use at least 10Hz update-rate data. This is a good compromise between obtaining single-difference multipath observables every second, (hence obtaining multipath-free RTK solutions every second as well) and not overloading the system with too many filtering operations. This will become, in the near future, less of a problem with the constant increase of hardware embedded processing power.

Furthermore when the platform is static and no previous calibration exists, the estimation of multipath parameters is impossible as the system is not observable.

7.3 Recommendations

1. The assumption that the reflection coefficient is the same at each antenna in the dual-antenna system, and that any change in the relative position between GNSS antennas most likely will affect at a small scale the amplitude and polarization of the reflected signals sensed by the two antennas (depending on their distance) would need to be assessed more consistently. For instances in a controlled environment such as in an anechoic chamber.

However, the multipath phase-delay will definitely change significantly along the ray trajectories of the plane waves passing through each of the antennas, even for very small between-antenna distances, and obtaining a rule of thumb for the optimal between antenna distances in all environments would most likely greatly improve the effectiveness of this technique.

2. This technique has been developed having in mind its use in any GNSS system, regardless of the frequency, as the method relies on multipath spatial/temporal characteristics and the relationship between a dual-antenna and specular reflectors. Nevertheless, remains to be seen how effective this system is when using frequencies other than GPS L1/L2. In fact, the derivation of typical MIMICS single-difference observables using optimal combination of GPS/Galileo frequencies seems like the appropriate research path.

This is true for Galileo signals structure, employing some of the most cutting-edge multipath limitation techniques becoming efficient with code observables, where in some cases this error is incredibly reduced to less than 10 cm. However, the same does not apply for Galileo carrier-phase multipath signals. Therefore, one can say that carrier-phase multipath mitigation is an ongoing topic with still much to be done, even with the incoming new (improved) signals and GNSS frequency diversity.

3. The combination of other GNSS observables could potentially be employed to improve the performance of the technique as the dissertation software is already prepared for that. The Incorporation of SNR information in the estimation process is likely to increase the system reliability as this observable has been used to model multipath due to being obtained from the receiver tracking and acquisition process. However, this technique using SNR observables has to be carefully assessed, as the SNR levels in different

receiver brands are usually different and may do not represent exactly same quantities (may be masked by internal receiver brand-dependent scalar factors).

4. The single-difference multipath observable equation was formulated only for the short delay multipath, as long delay multipath errors can be mitigated using existing correlator-based techniques implemented in most current commercial GNSS receivers.

However, it needs to be assessed what exactly should be the short-delay boundary as during some of the performed stress-tests where the system experienced distances less than half-meter from a strong reflector surface (with dimensions bigger than 2 GPS L1 cycles) the system become rather ineffective as the multipath phase-delay between the antennas cannot be discriminated.

Bibliography

Axelrad, P., C.J. Comp, and P.F. Macdoran (1996). "*SNR-Based Multipath Error Correction for GPS Differential Phase*". IEEE Transactions on Aerospace and Electronic Systems, Vol. 32, pp. 650-660.

Bilich, A., K.M. Larson, and P. Axelrad (2004) "*Observations of Signal-to-Noise Ratios (SNR) at Geodetic GPS site CASA: Implications for Phase Multipath.*" Proceedings of the Centre for European Geodynamics and Seismology, pp. 77-83.

Borre, K., D.M. Akos, N. Bertelsen, P. Rinder, and S.H. Jensen (2007). A Software-Defined GPS and Galileo Receiver – A single-Frequency Approach. Birkhauser, Boston, MA, 176 pp.

Brown, A., and R. Silva (2000). "*A GPS Digital Phased Array Antenna and Receiver*". Proceedings of IEEE Phased Array Symposium, Dana Point, CA, May 21-25, pp. 153-156.

Bruton, A.M., C.L. Glennie, and K.P. Schwarz (1999). "*Differentiation for High-Precision GPS Velocity and Acceleration Determination*". GPS Solutions, Vol. 2, No. 4, pp. 4-21.

Crassidis, J.L. (2006). "*Sigma-point Kalman filtering for integrated GPS and inertial navigation*". IEEE Transactions on Aerospace and Electronic Systems, Vol. 42, Issue 2, pp. 750-756.

Collins, J.P., and R.B. Langley (1997). "*Estimating the Residual Tropospheric Delay for Airborne Differential GPS Positioning*". Proceedings of ION GPS-97, the 10th International Technical Meeting of the Satellite Division of The Institute of Navigation, Kansas City, MO, September 16-19, pp. 1197-1206.

Eldar, Y.C., and A.V. Oppenheim (2002). "*MMSE whitening and subspace whitening*". IEEE Transactions on Information Theory, Vol. 49, Issue 7, pp. 1846-1851.

El-Mowafy, A. (2005). "Analysis of the Design Parameters of Multi-Reference Station RTK v GPS Networks". Journal of Satellite and Land Information Science (SaLIS), Vol. 65, No. 1, pp. 17-26.

Fenton, P. C., and J. Jones (2005). "*The Theory and Performance of NovAtel Inc.'s Vision Correlation*". Proceedings of ION GNSS 2005, Long Beach, CA, September 13-16, pp. 2178-2186.

Gelb, A., editor (1974). *Applied Optimal Estimation*. MIT Press, Cambridge, MA. 382 pp.

Georgiadou, Y. and A. Kleusberg (1988). “*On Carrier Signal Multipath Effects in Relative GPS Positioning*”. *manuscripta geodatica*, Springer-Verlag, **13**, 3, pp. 172-179.

Barrows, A.K., D. Gebre-Egziabher, R. Hayward, and X. Renxin (1996) “GPS-Based Attitude and Guidance Displays for General Aviation”, *Proceedings of Emerging Technologies and Factory Automation, EFTA 1996, IEEE, Vol. 2, Kauai, Hawaii, November 18-21*, pp. 423-428.

Grewal, M., L. Weill, and A. P. Andrews (2007). *Global Positioning Systems, Inertial Navigation, and Integration with MATLAB CD*. Wiley & Sons, Hoboken, New Jersey. 517 pp.

Hannah, B.M. (2001) *Modeling and simulation of GPS multipath propagation*. PhD thesis, Queensland University of Technology, Australia, 375 pp.

Hansen, A. (2000) *Ionospheric Model*, Retrieved 31st of May 2013, from:
<http://waas.stanford.edu/~wwu/ahansen/papers/ionntm00/node3.html>

Hein, G.W., M. Irsigler, and J.A. Avila-Rodriguez (2004). “*Performance of Galileo L₁ Signal Candidates*”. *Proceedings of the European Navigation Conference GNSS 2004, 16-19 May 2004, Rotterdam, The Netherlands*.

Hofmann-Wellenhof, B., H. Lichtenegger, and J. Collins (2001). *Global Positioning System: Theory and Practice*. Springer Wien New York, 2001. 5th revised edition, 389 pp.

ICD-GPS-200C (1999). *Navstar GPS Space Segment/Navigation User Interface Control Document*, GPS Navstar JPO, 138 pp.

Ifeachor, E.C., and B.W. Jervis (1993). *Digital Signal Processing: A Practical Approach*. Addison-Wesley Publishing Co., Workingham, England. 933 pp.

Itani, K., T. Hayashi and M. Ueno (2000). “*Low-Cost Wave Sensor Using Time Differential Carrier Phase Observations*”. *Proceedings of ION GPS 2000, Salt Lake City, Utah, September 19-22*, pp. 1467-1475.

Kavak, A., G. Xu, and W. J. Vogel (1996). “*GPS Multipath Fade Measurements to Determine L-Band Ground Reflectivity Properties*”. *Proceedings of the 20th NASA propagation experimenters meeting, Jet Propulsion Laboratory, Fairbanks, AK*, pp. 257-263.

- Khan, I.R., and R. Ohba (1999). “*Digital Differentiators Based on Taylor Series*”. IEICE Trans Fundamentals, Vol. E82-A, No. 12, December 1999, pp. 2822-2824.
- Klobuchar, J. (1987). “*Ionospheric Time-Delay Algorithms for Single-Frequency GPS Users*”. IEEE Transactions on Aerospace and Electronic Systems, Vol. AES-23, Issue 3, pp. 325-331.
- Kennedy, S. (2002). “*Precise Acceleration Determination from Carrier Phase Measurements*”. Proceedings of ION GPS 2002, Portland, Oregon, September 24-27, pp. 962-972.
- Keong, J.H., and G. Lachapelle (2000). “*Heading and Pitch Determination Using GPS/GLONASS*”. GPS Solutions, Vol. 3, Issue 3, pp. 26-36.
- Kim, D., and R.B. Langley (2003). “*On Ultrahigh-Precision Positioning and Navigation*”. Navigation: Journal of The Institute of Navigation, Vol. 50, No. 2, Summer, pp. 103-116.
- Kunysz, W. (2000). “*High Performance GPS Pinwheel Antenna*”. 6 pp., NovAtel Article, Retrieved 10th of October 2013, from:
http://gpsplusins.com/assets/Documents/Papers/gps_pinwheel_ant.pdf
- McNamara, D.A., C.W.I. Pistorius, and J.A.G. Malherbe (1990). Introduction to the Uniform Geometrical Theory of Diffraction. Artech House, Norwood, MA, 471 pp.
- Mendes, V.B., J.P. Collins, and R.B. Langley (1995). “*The Effect of Tropospheric Propagation Delay Errors in Airborne GPS Precision Positioning*”. Proceedings of ION GPS-95, the 8th International Technical Meeting of the Satellite Division of The Institute of Navigation, Palm Springs, CA, September 12-15, pp. 1681-1689.
- Niell, A.E. (1996). “*Global mapping functions for the atmosphere delay at radio wavelengths*”. Journal of Geophysical Research, Vol. 101, No. B2, pp. 3227-3246.
- Novoselov, R.Y., S.M. Herman, S.M. Gadaleta, and A.B. Poore (2005). “*Mitigating the Effects of Residual Biases with Schmidt-Kalman Filtering*”. Proceedings of the 8th International Conference on Information Fusion, Philadelphia, PA, July 25-28, Vol. 2.
- Pany, T., M. Irsigler, B. Eissfeller, and J. Winkel (2002). “*Code and Carrier Phase Tracking Performance of a Future Galileo RTK Receiver*”. Proceedings of the European Navigation Conference ENC-GNSS, Copenhagen, Denmark, May 27-30.
- Park, M. (2004). Error Analysis and Stochastic Modeling of MEMS based Inertial Sensors for Land Vehicle Navigation Applications. M.Sc. thesis, April 2004, UCGE Report 20194, University of Calgary, Canada, 135 pp.

Popović, Z., and B. Popović (2000). *Introductory Electromagnetics*. Prentice Hall, Englewood Cliffs, NJ, 556 pp.

Ray, J.K., M.E. Cannon, and P. Fenton (1998). “*Mitigation of Static Carrier Phase Multipath Effects Using Multiple Closely Spaced Antennas*”. Proceedings of ION GPS 1998, Nashville, Tennessee, September 15-18, pp. 1025-1034.

Ray, J.K. (1999). “*Use of Multiple Antennas to Mitigate Carrier Phase Multipath in Reference Stations*”. Proceedings of ION GPS 1999, Nashville, TN, September 14-17, pp. 269-279.

Revnivykh, S. (2012). “*GLONASS Status and Modernization*”. Proceedings of International GNSS Committee IGC-7, Beijing, China, November 4-9, 2012.

Ryan, S., G. Lachapelle, and M. E. Cannon (1997). “*DGPS Kinematic Carrier Phase Signal Simulation Analysis in the Velocity Domain*”. Proceedings of ION GPS 97, Kansas City, Missouri, September 16-19, pp. 1035-1045.

Saastamoinen, J. (1973). “*Contributions to the theory of atmospheric refraction*”. In three parts. Bulletin Géodésique , No. 105, pp. 279-298; No. 106, pp. 383-397; No. 107, pp. 13-34.

Sahmoudi, M., R. Landry (2008). “*Multipath Mitigation Techniques Using Maximum-Likelihood Principle*”. Inside GNSS Magazine, November/December 2008 Issue, Volume 3, Number 8, pp. 24-29.

Serrano, L., D. Kim, and R.B. Langley (2004). “*A Single GPS Receiver as a Real-Time, Accurate Velocity and Acceleration Sensor*”. Proceedings of ION GNSS 2004, 17th International Technical Meeting, Long Beach, CA, September 21-24, pp. 2021-2034.

Serrano, L., D. Kim, and R.B. Langley (2006). “*Near Real-Time Carrier-Phase Multipath Mitigation in Kinematic Applications, Using a Dual-Antenna System and Effective Close Range Reflectors*”. Proceedings of ION GNSS 2006, the 19th International Technical Meeting, Fort Worth, TX, September 26-29, pp. 863-872.

Subirana, J., J.M. Zornoza, and M. Hernandez-Pajares (2011) “GNSS Signal, Fundamentals, ESA Navipedia, Retrieved 31st of May 2013, from: http://www.navipedia.net/index.php/GNSS_signal

Szarmes, M., S. Ryan, G. Lachapelle, and P. Fenton (1997). “*DGPS High Accuracy Velocity Determination Using Doppler Measurements*”, Proceedings of KIS 97, Department of Geomatics Engineering, The University of Calgary, Banff, June 3-6, pp. 167-174.

van Dierendonck, A.J., P. Fenton, and T. Ford (1992), “*Theory and Performance of Narrow Correlator Technology in GPS Receiver*”, *NAVIGATION: Journal of The Institute of Navigation*, 39, 3, pp. 265-283.

Van Graas, F., and A. Soloviev (2003). “*Precise Velocity Estimation Using a Stand Alone GPS Receiver*”. Proceedings of ION NTM 2003, Anaheim, California, January 22-24, pp. 262-271.

Teunissen, P. [1996]. “GPS Carrier phase ambiguity Fixing concepts”, in *GPS for Geodesy. Lecture Notes in Earth Sciences*, Springer, pp. 263-335.

“The System: Radical Change in the Air For GLONASS” (2007). *GPS World*, Vol. 18, N. 2, February 2007, pp. 14-15.

Townsend, B., P. Fenton, K. van Dierendonck, and R.D.J. van Nee (1995). “*L1 Carrier Phase Multipath Error Reduction Using MEDLL Technology*”, Proceedings of ION GPS-95, Palm Spring, September 12-15, pp. 1539-1544.

Tregoning, P., and T.A. Herring (2006). “*Impact of a Priori Zenith Hydrostatic Delay Errors on GPS Estimates of Station Heights and Zenith Total Delays*”. *Geophysical Research Letters*, Vol. 33, Issue 23, December 2006, 5 pp.

Trimble GCS900 on a Dozer with Dual GPS, Retrieved 31st of May 2013, from:
<http://www.trimble.com/gcs900dg-dzr.shtml>

Trimble GCS900 on a Motor Grader With Dual GPS, Retrieved 31st of May 2013, from:
<http://www.trimble.com/gcs900dg-mg.shtml>

Weill, L., and B. Fisher (2000) “*Method for mitigating multipath effects in radio ranging*”. U.S. patent 6, 031, 881, Feb. 29, 2000.

Curriculum Vitae

Candidate's full name: Luis Miguel Pina Amaral Serrano

Current Position/Employer GNSS R&D Engineer, Trimble Navigation

Universities attended: Dept. of Mathematics, Faculty of Sciences of the
University of Lisbon
Campo Grande, 1749-016, Lisbon, Portugal
Dipl. Engineer, 1995-2002, Surveying Engineering

Dept. of Geodesy and Geomatics Engineering, University
of New Brunswick
P.O. Box 4400
Fredericton, New Brunswick, E3B 5A3
Ph.D. Candidate in GNSS/Geodesy and Geomatics
Engineering

Publications:

Serrano, L., D. Kim, R. B. Langley, K. Itani and M. Ueno (2004). "A GPS Velocity Sensor: How Accurate Can It Be? – A First Look." Proceedings of NTM 2004, the 2004 National Technical Meeting of The Institute of Navigation, San Diego, CA, 26-28 January 2004; pp. 875-885.

Serrano, L., D. Kim, and R. B. Langley (2004). "A Single GPS Receiver as a Real-Time, Accurate Velocity and Acceleration Sensor." Proceedings of GNSS 2004, the 2004 GNSS of The Institute of Navigation, Long Beach, CA, 21-24 September 2004; pp. 2021-2033.

Serrano, L., D. Kim, and R. B. Langley (2005). "A New Carrier-Phase Multipath Observable for GPS Real-Time Kinematics Based on Between Receiver Dynamics." Proceedings of The 61st Annual Meeting of The Institute of Navigation, Cambridge, MA, 27-29 June 2005.

Serrano, L., D. Kim, and R. B. Langley (2005). "A New Approach for Mitigating Low-

- Frequency Carrier-Phase Multipath in GPS-RTK, Based on Between-Receiver Dynamics and an Effective Reflector". Proceedings of The ION GNSS Meeting of The Institute of Navigation, Long Beach, CA, September 13-16, 2005.
- Kim D., L. Serrano and R. B. Langley (2005). "Compensating Phase Wind-up Effects for Improving the Performance of a GPS RTK-Based Vehicle Navigation System". Proceedings of The ION GNSS Meeting of The Institute of Navigation, Long Beach, CA, September 13-16, 2005.
- Beran T., R. B. Langley, S. B. Bisnath and L. Serrano (2005). "High-Accuracy Point Positioning with Low-Cost GPS Receivers: How Good Can It Get?" Proceedings of The ION GNSS Meeting of The Institute of Navigation, Long Beach, CA, September 13-16, 2005 (**Best Paper Award**).
- Serrano, L., D. Kim and R. B. Langley (2006). "Performance Analysis of the NovAtel OEM4-G2L Receiver for Low Earth Orbit Satellite Tracking". Report for the Canadian Space Agency (CASSIOPE Project), May 2006, 18 pp
- Kim D., L. Serrano and R. B. Langley (2006). "Phase Wind-Up Analysis: Assessing Real-Time Kinematic Performance". Innovation Column, GPS World, September 2006, pp. 58-64.
- Serrano, L., D. Kim, and R. B. Langley (2006). "Near Real-Time Carrier-Phase Multipath Mitigation in Kinematic Applications, Using a Dual-Antenna System and Effective Close Range Reflectors". Proceedings of The ION GNSS Meeting of The Institute of Navigation, Fort-Worth, TX, September 26-29, 2006.
- Beran T., R. B. Langley, S. B. Bisnath and L. Serrano (2006). "High-Accuracy Point Positioning with Low-Cost GPS Receivers: How Good Can It Get?" Accepted for publication at "Navigation", Journal of The Institute Of Navigation
- Serrano, L., D. Kim, and R. B. Langley (2007). "Real-time Multipath Calibration of a GPS-Based Heading Reference system". Proceedings of TimeNav'07, European Navigation Conference GNSS 07, Geneva, Switzerland.
- Serrano, L. (2007). "Leica Geosystems New Technologies". Presented at European CGSIC/ISC Meeting, TimeNav'07, European Navigation Conference GNSS 07, Geneva, Switzerland
- Serrano, L., D. Kim, and R. B. Langley (2008). "Carrier-Phase Multipath Calibration in GPS-RTK Machine-Guidance Applications". Proceedings of The ION / IEEE PLANS Conference, Monterey, CA, May 3-5 (**Best Paper Award**).
- Serrano, L., C. S. Dixon, and R. Haas (2009). "Pseudolite Augmentation for GNSS-based Monitoring Systems". Proceedings of ENGA 09 (Encontro Nacional de Geodesia

Aplicada), 12-13 October, LNEC, Lisbon, Portugal.

Serrano, L. (2010). "Multipath Adaptive Filtering in GNSS/RTK-Based Machine automation Applications". Proceedings of the ION/IEEE PLANS Conference, 3-6 May 2010, Indian Wells/Palm Springs, CA.